

Preparatory Study for in-situ Neutron Diffraction Experiments of creep-exposed 9%Cr Crosswelds at VULCAN

Diploma Thesis of
Ozan Caliskanoglu

Institute for Materials Science and Welding



Chair: Univ.-Prof. Dipl.-Ing. Dr. techn. Christof Sommitsch

Supervisors: Univ.-Prof. Dipl.-Ing. Dr. techn. Peter Mayr

Dipl.-Ing. Christian Schlacher

Faculty of Mechanical Engineering and Economic Sciences

Graz University of Technology



Graz, 2011

STATUTORY DECLARATION

I declare that I have authored this thesis independently, that I have not used other than the declared sources / resources, and that I have explicitly marked all material which has been quoted either literally or by content from the used sources.

date

(signature)

EIDESSTATTLICHE ERKLÄRUNG

Ich erkläre an Eides statt, dass ich die vorliegende Arbeit selbstständig verfasst, andere als die angegebenen Quellen/Hilfsmittel nicht benutzt, und die den benutzten Quellen wörtlich und inhaltlich entnommene Stellen als solche kenntlich gemacht habe.

Datum

(Unterschrift)

Acknowledgements

First of all, I would like to thank my supervisor Prof. Peter Mayr from the Chemnitz University of Technology for enabling this diploma thesis and for supporting me with encouraging words and deeds.

I owe particular thanks to Prof. Christof Sommitsch for giving me the opportunity to join the team at the Institute for Materials Science and Welding.

Special thanks go to my second advisor Dipl.-Ing. Christian Schlacher for his kind assistance and help during this work.

Furthermore, I thank Dr. Francisca Méndez Martín who was very helpful in providing useful information.

I am grateful to my family and all the people who supported me in completing this thesis.

Abstract

High-temperature applications such as thermal power plants require suitable as well as reliable heat- and creep-resistant materials. The use of welded components in such facilities is essential and will also remain in the future. On the basis of the high performance, martensitic boron alloyed 9%Cr steels will be investigated for this study. Welds represent a significant problem in terms of creep failures which may occur during service in the heat-affected zone (HAZ). Premature creep failures limit the lifetime of the components and can cause unexpected breakdowns.

Non-destructive materials testing techniques are becoming more and more important to examine the properties and behavior of materials under extreme conditions. Strain and stress measurements by diffraction using neutrons are of great importance and enable a very accurate materials research at the atomic level. The powerful engineering materials diffractometer VULCAN at the Spallation Neutron Source at Oak Ridge National Laboratory in Tennessee, which was recently put into operation, is one of the world's most sophisticated neutron diffraction instruments and may capacitate the study of the complex creep mechanisms in 9%Cr steel welds in a way that has never before been possible. VULCAN facilitates e.g. a three-dimensional strain mapping and in-situ studies of welded joints at simulated service conditions during creep exposure.

The content of this work includes a detailed description of theoretical foundations and the state-of-the-art neutron diffraction theory in materials testing in conjunction with the characteristic capabilities of VULCAN.

The objective is to point out the technical possibilities of diffraction using neutrons and to provide new insights into the different mechanisms occurring in the HAZ in creep exposed crosswelds in order to achieve a better understanding of the relationship between strain and creep rupture behavior.

Kurzfassung

Hochtemperaturanwendungen wie kalorische Kraftwerke erfordern entsprechend betriebssichere hitze- und kriechbeständige Materialien. Die Verwendung von geschweißten Bauteilen ist in heutiger Zeit nicht wegzudenken und wird auch in Zukunft bestehen bleiben. Basierend auf diesen hohen Leistungsanforderungen werden borlegierte martensitische 9% Chromstähle im Rahmen dieser Arbeit untersucht. Allerdings stellen die Zeitstandfestigkeiten der Schweißnähte ein wesentliches Problem dar, die sich während dem Betrieb in der Wärmeeinflusszone (WEZ) verschlechtern können. Vorzeitige Kriechschäden können die Lebensdauer der Komponenten erheblich herabsetzen und zu plötzlichem Versagen führen.

Zerstörungsfreie Werkstoffprüfverfahren ermöglichen die Untersuchung von Materialeigenschaften und -verhalten unter extremen Bedingungen und gewinnen zunehmend an Bedeutung. Dehnungs- und Spannungsmessungen mittels Neutronenstreuung sind von hoher Wichtigkeit und eignen sich hervorragend zur Materialforschung auf atomarer Ebene. Das kurz zuvor in Betrieb genommene hochmoderne Neutronendiffraktometer VULCAN bei der Spallationsneutronenquelle in Tennessee ist eines der weltweit technisch ausgereiftesten Systeme seiner Klasse und könnte erstmals eine zuvor noch nie durchgeführte komplexe Kriechanalyse an geschweißten 9% Chromstählen realisieren. VULCAN ermöglicht u.a. eine dreidimensionale Dehnungsmessung und in-situ Studien unter simulierten Betriebsbedingungen an Schweißnähten während des Kriechens.

Der Inhalt der Studie befasst sich mit den theoretischen Grundlagen der Materialprüfung mittels der Neutronenstreuung im Zusammenhang mit den charakteristischen Fähigkeiten und Besonderheiten von VULCAN.

Das Ziel dabei ist, die technischen Möglichkeiten der Neutronendiffraktometrie zu analysieren, um diese auf kriechbelastete Schweißnähte zu überführen, sich neue Einblicke in die unterschiedlichen Mechanismen in der WEZ zu verschaffen und ein besseres Verständnis der Zusammenhänge zwischen Beanspruchung und Kriechbruchverhalten zu bekommen.

Table of Contents

1. Introduction	1
2. Objectives.....	4
3. Creep-Resistant 9%Cr Steels for USC Components.....	5
3.1 Preface	5
3.2 Definition of Creep.....	7
3.2.1 Creep Curves	7
3.3 Development of 9-12% Cr-Steels for Critical Components.....	8
3.4 Welded Joints in Martensitic 9%Cr Steels.....	13
3.4.1 The Heat Affected Zone.....	14
3.4.2 Cracks in 9%Cr Steel Welds	16
3.4.2.1 Type IV Cracking.....	16
4. Neutron Diffraction to Engineering Problems.....	18
4.1 Properties of Neutrons	18
4.1.1 Why use Neutrons?.....	19
4.2 Neutron-Producing Reactions.....	20
4.2.1 Nuclear Fission	20
4.2.2 Spallation.....	21
4.2.3 Pulsed vs. Steady-State Neutron Sources.....	23
4.2.4 Pulsed Spallation Neutron Sources.....	24
4.3 Principles of Neutron Scattering.....	24
4.3.1 Neutron Scattering Cross Sections	24
4.3.2 Scattering by a single fixed Nucleus.....	26
4.3.3 Scattering by many Nuclei.....	27
4.3.4 Coherent and Incoherent Neutron Scattering.....	28
4.3.5 Elastic Neutron Scattering.....	29
4.3.6 Inelastic Neutron Scattering.....	30
4.4 Neutron Diffraction.....	31
4.4.1 Time-of-Flight Technique	32
4.4.2 Observation of Diffraction Profiles and Refinement	33
4.4.2.1 Information from Diffraction Spectra.....	33
4.4.2.2 General Structure Analysis System.....	34

4.5	Small Angle Neutron Scattering.....	36
4.5.1	Principle.....	37
4.5.2	SANS Formalism.....	38
4.5.2.1	Guinier and Porod Regime.....	40
4.5.3	Practical Application.....	40
4.6	Strain and Stress Analysis.....	42
4.6.1	Definition of Strain and Stress.....	42
4.6.2	Polycrystalline Materials.....	44
4.6.3	Classification of Residual Stresses.....	45
4.6.4	Determination of the Reference Lattice Spacing d_{hkl}^0	46
4.6.5	Volumetric Strain Mapping.....	46
4.6.6	Residual Stress Measurement by Neutron Diffraction in Welds.....	48
4.6.6.1	Origin of Residual Stresses in Welds.....	48
4.6.6.2	Practical Example – Bead-on-Plate Weld Specimen.....	49
4.7	Texture Analysis.....	51
4.7.1	Basics.....	51
4.7.2	Presentation of Orientations.....	52
4.7.3	Euler Angles.....	52
4.7.4	Pole Figures.....	53
4.7.5	Inverse Pole Figures.....	54
4.7.6	Orientation Distribution Function.....	55
4.7.7	Texture Analysis with TOF Neutron Diffractometers.....	56
4.8	Deformation Analysis.....	60
4.8.1	Elastic and Plastic Deformation.....	60
4.8.2	In-situ Deformation Studies.....	62
4.9	Phase Transformation Analysis.....	65
4.9.1	Basics.....	66
4.9.2	In-situ Study during Phase Transformations.....	66
5.	The Spallation Neutron Source at Oak Ridge.....	69
5.1	Functionality.....	70
5.1.1	Front-End System.....	71
5.1.2	Linac.....	71
5.1.3	Accumulator Ring.....	71
5.1.4	Target.....	72
5.1.5	Neutron Detector Instruments.....	72

5.2	The Engineering Materials Diffractometer VULCAN	73
5.2.1	Sample Environment.....	75
5.2.1.1	VULCAN load-frame.....	76
5.2.1.2	ILL 1800°C Furnace	77
5.2.1.3	Heavy Duty Sample Table.....	78
6.	Possible Experimental Procedures at VULCAN	79
6.1	Testing Materials	79
6.2	Sample Preparation.....	81
6.3	Data Analysis.....	82
7.	Summary and Outlook	84
	List of Literature.....	86
	Appendix.....	92
	Appendix A: Pulsed Spallation Neutron Sources and Main Parameters.....	93
	Appendix B: Neutron Scattering Lengths and Cross Sections of Selected Elements and Isotopes.....	95
	Appendix C: Radii of Gyration of some Selected Homogeneous Particles	100
	Appendix D: Technical Parameters of the SNS	101
	Appendix E: SNS Instrumentation	102

List of Symbols and Abbreviations

General

A_{C1}	temperature at which austenite transformation starts on heating
A_{C3}	temperature at which austenite transformation is complete on heating
ACCEPT	alloy development for critical components of environmental friendly power plants
BN	boron nitride
CGHAZ	coarse-grained heat-affected zone
COST	Cooperation in Science and Technology
DOE	U.S. Department of Energy
e	electron
e^+	positron
EPRI	Electric Power Research Institute
FEM	finite-element modeling
FGHAZ	fine-grained heat-affected zone
FIM	field ion microscopy
HAZ (WEZ)	heat-affected zone
ICHAZ	intercritical heat-affected zone
ILL	Institut Laue-Langevin
IWS	Institute for Materials Science and Welding
linac	linear accelerator
n	neutron
NIMS	National Institute for Materials Science
NSF	National Science Foundation
NSS	neutron spallation source
ORNL	Oak Ridge National Laboratory
p	proton
PAGB	prior austenite grain boundaries
PWHT	post-weld heat treatment

R&D	research and development
SANS	small angle neutron scattering
SAXS	small angle x-ray scattering
SC	supercritical
SEM	scanning electron microscopy
SNS	Spallation Neutron Source
t	time
t_r	time to rupture
t_0	instantaneous time
T_m	absolute melting temperature
$T_{\gamma\delta}$	temperature at which delta-ferrite transformation is complete on heating
TEM	transmission electron microscopy
TIG	tungsten inert gas welding
TMCP	thermo-mechanical controlled process
UNFCCC	United Nations Framework Convention on Climate Change
USC	ultra-supercritical
XRD	x-ray diffraction
ZGS	zero gradient synchrotron
ZING-P	zero gradient synchrotron intense neutron generator-prototype
α	ferrite
γ	austenite
Γ	gamma radiation
ε	strain
ε_0	strain at time t_0
$\dot{\varepsilon}$	creep-rate
Π	pion
σ	stress

Neutron Diffraction

A_h	absorption correction factor
b	neutron scattering length
d	(interplanar) lattice spacing
d_{hkl}	(interplanar) lattice spacing between planes of the Miller indices
d_{hkl}^0	(interplanar) reference lattice spacing between planes of the Miller indices of the stress-free material
$d\Omega$	differential solid angle
$d\sigma/d\Omega$	differential neutron scattering cross section
$d^2\sigma/d\Omega dE$	partial differential neutron scattering cross section
E	energy of the neutron
E_i	energy of the incident neutron
E_{ph}	extinction correction factor
E_s	energy of the scattered neutron
F_{ph}	structure factor
FWHM	full width at half-maximum
GSAS	General Structure Analysis System
h	Planck's constant
\hbar	reduced Planck's constant
$H\Delta T$	profile shape function
I_b	background scattering intensity
I_C	calculated intensity
I_{ph}	Bragg-intensity
k	wavevector
k_i	incident wavevector
k_s	scattered wavevector
L	total path length of the neutron (source-to-detector path length)
L_P	Lorentz-polarization correction factor
L_1	source-to-sample path length of the neutron
L_2	sample-to-detector path length of the neutron
m_n	neutron mass

M_p	reflection multiplicity
O_{ph}	preferred orientation correction factor
p	momentum
Q	scattering vector / wavevector transfer
Q_L	scattering vector / wavevector transfer left detector
Q_R	scattering vector / wavevector transfer right detector
r_0	neutron radius
$R_{i/j}$	scattered spherical wave distance to the scattering center
S_h	histogram scale factor
S_{ph}	phase scale factor
TOF	time-of-flight
v	neutron velocity
v_i	incident neutron velocity
v_s	velocity of the scattered neutron
V_p	unit cell volume for a phase
θ	scattering (diffraction) angle
λ	wavelength
μ	magnetic dipole moment
μ_N	nuclear magneton
σ	neutron scattering cross section
σ_{coh}	coherent neutron scattering cross section
σ_{inc}	incoherent neutron scattering cross section
σ_{tot}	total neutron scattering cross section
Φ	neutron beam flux
ψ_i	incident plane wavefunction
ψ_s	scattered spherical wavefunction

SANS

$d\Sigma/d\Omega$	macroscopic differential neutron scattering cross section
f	volume fraction
I_0	incident intensity
N	number density

N_P	number of particles
P	form factor
R_g	radius of gyration
S	structure factor
V_P	particle volume
ρ	neutron scattering length density
Φ	azimuthal angle

Strain and Stress Analysis

A	cross-sectional plane
C_{ijkl}	stiffness tensor
E	modulus of elasticity / Young's modulus
E_{hkl}	plane-specific modulus of elasticity / Young's modulus
F	applied force
l	length after subjected to force
l_0	original length
LD	longitudinal direction
ND	normal direction
S_{ijkl}	compliance tensor
TD	transverse direction
ν	Poisson's ratio
ν_{hkl}	plane-specific Poisson's ratio
V	gauge volume
δ	Kronecker delta function
ε	engineering strain
ε_{ij}	strain tensor
σ	engineering stress
σ_{ij}	stress tensor
σ_R^I	type I residual (macro)-stress
σ_R^{II}	type II residual (micro)-stress
σ_R^{III}	type III residual (micro)-stress

Texture Analysis

CCS	crystal coordinate system
E-WIMV	extended Williams-Imhof-Matthies-Vinel
L	logarithmic scale
m.r.d.	multiples of random distribution
MAUD	material analysis using diffraction
ODF	orientation distribution function
p	projection plane
SCS	sample coordinate system
WIMV	Williams-Imhof-Matthies-Vinel
α, β, γ	Euler angles
φ_1	rotation around z-axis
φ_2	rotation around z'-axis
Φ	rotation around x'-axis

Deformation Analysis

A	slip plane
A_0	plane perpendicular to uniaxial applied force
C	cooling
DSA	dynamic strain aging
F	uniaxial applied force
H	heating
τ	shear stress
τ_{crit}	critical shear stress

1. Introduction

Power station industries with substantial gains in efficiency have lower fuel consumption and therefore lower CO₂ emissions [1]. High thermal efficiencies can be achieved by increasing the steam pressure and temperature in the range of 650°C as seen in supercritical (SC) and ultra-supercritical (USC) power plants [2]. These facilities necessitate the need for safe and reliable heat- and creep-resistant power generation parts like boiler components, steam turbines, valves, tubings and pipings (Figure 1).



Figure 1: Welded power generation components. “Boiler Engineering Company Rafako S.A”

Due to these high-temperature requirements the use of advanced boron alloyed 9% chromium steels with a martensitic microstructure is well-established for such high-temperature applications [3]. 9%Cr steels are also remarkable for their excellent formability and weldability. Weldments in the construction as well as in maintenance and repair works are indispensable and will be by far the most common joining technology for thermal power plants in the future [4].

The fine-grained or the intercritical region of the heat-affected zone (HAZ) which is formed through the welding process seems to be the weakest link in

welded joints. Premature creep failures are the most critical failure mechanisms and decrease the creep-rupture strength down to half of the base metal strength. These failures can cause cracks and limit the lifetime of the welded components. Long-term creep rupture tests at elevated temperatures have shown that the specimens mostly collapse due to the so-called type IV cracking in the fine-grained HAZ [4]. Materials properties like creep strength and ductility deteriorate with increasing operating hours and can lead to unexpected disaster (Figure 2).

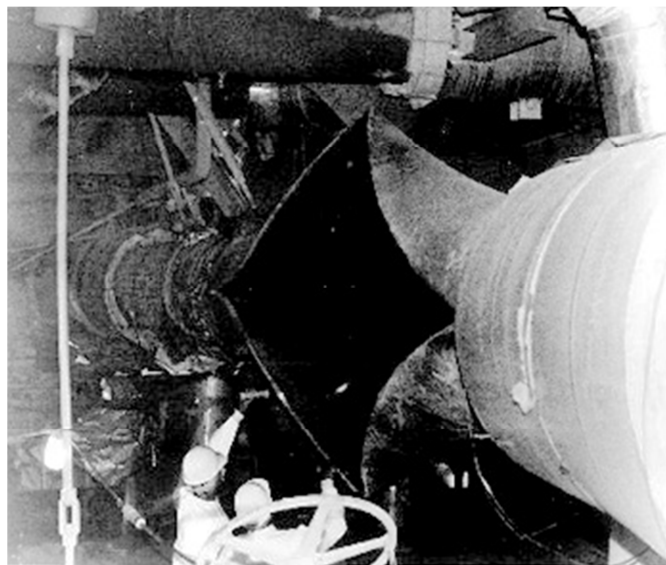


Figure 2: Seam failure causes 6 deaths in the USA [4]

Insufficient material resistance under extreme conditions forces engineers and constructors correspondingly to cause studies on the fractured components. Usual material testing techniques are for example non-destructive methods such as electron microscopy or X-ray diffraction and simulation-based methods like finite-element modeling (FEM). Recent advances in the area of materials research have shown that sophisticated neutron diffraction investigations enable very reliable in-situ determinations of the properties and behavior of materials during service. Neutron sources provide very intense neutron beams which can be used e.g. to investigate the strain by diffraction at the microstructural level. The method is based on the same principle as in X-ray diffraction but enables a more accurate measurement of bulk samples.

The Spallation Neutron Source (SNS) at Oak Ridge National Laboratory (ORNL) in Tennessee provides the most intense pulsed neutron beams in the world and opens up new scientific possibilities for researchers in materials science and engineering. The engineering diffractometer VULCAN at the SNS recently realizes a three-dimensional strain mapping with very high spatial resolution in parts such as welds and enables in-situ experiments of materials creep behavior at simulated operating conditions [5]. This ability is of great interest and allows engineers to understand the mentioned critical premature creep failure in the HAZ of welded 9%Cr steels.

Peter Mayr and his team received a 4-day beam time at the SNS in December 2011 in order to conduct some in-situ experiments at VULCAN. The aim of the study is the observation of stress/strain distribution in 9%Cr crosswelds at elevated temperature and small external loading similar to creep conditions.

2. Objectives

This thesis has the main objective to show a possible preparatory study for in-situ neutron diffraction experiments of creep-exposed welded 9%Cr steels at VULCAN with the aim to analyze different mechanisms such as strain and stress evolution in the different regions of the HAZ during creep exposure. Type IV cracking is the most noted failure cause of welds exposed to long-term creep testings. The damage assessment can be either done with metallographic examinations or with the help of numerical and computational methods. Of course there were various experiments already carried out to provide improvement potentials in order to extend the service life of the welded joints, but they were primarily characterized by in-situ without other ancillary equipment (e.g. only in-situ tensile tests), ex-situ and simulation-based measurements like FEM. The most challenging problem nevertheless is the fundamental understanding of the creep mechanics in the weld dependent on the temperature and applied stress.

This work provides a literature study to carry out, among other things, future in-situ analysis of creep specimens with neutron diffraction and to understand the mechanism of the premature creep failure which leads to high creep rupture strength losses down to 50%. The diffractometer VULCAN with appropriate coupled ancillary equipment enables high-temperature creep tests by simulating service conditions around 1000°C and stress loads of a few hundred MPa. This instrument allows a 3D-mapping of the strain e.g. around crucial regions of the HAZ and may collect important know-how for the purpose of future projects.

The knowledge gained from such in-situ diffraction studies may be decisive for further research projects and should supply R&D scientists with unprecedented insights into high-temperature properties of creep-exposed 9%Cr crosswelds. The main goal is to explore the correlation between the strain and the creep rupture behavior in service. This might close an important gap in scientific knowledge which can contribute considerably to the avoidance of type IV cracking.

3. Creep-Resistant 9%Cr Steels for USC Components

3.1 Preface

Global warming is currently one of the most challenging topics of climate protection. The change of the global radiation equilibrium in the stratosphere can be described by the so-called radiative forcing, the difference of incoming short and emitted long wave radiation. Carbon dioxide (CO₂), methane (CH₄), nitrous oxide (NO₂) and other greenhouse gases have the ability to absorb these long wave radiations and lead to a positive radiative forcing which results in higher temperatures on the earth. This process is also known as the greenhouse effect. CO₂ concentrations have the biggest share (~70%) of the greenhouse gases and are mainly generated by combustion processes like burning fossil fuels. An accelerated greenhouse effect and an increase of the global temperature will have drastic impacts on nature like rising sea levels, melting glaciers and extinction of species. Table 1 shows the world-wide CO₂ emission caused by human activities, especially through burning fossil fuels in power plants [1].

Table 1: Profile by process or industrial activity of worldwide large stationary CO₂ sources with emissions of more than 0.1 million tons of CO₂ per year [1]

Process	Number of Sources	Emissions (MtCO ₂ /year)
Fossil Fuels		
Power	4.942	10.539
Cement Production	1.175	932
Refineries	638	798
Iron and Steel Industry	269	646
Petrochemical Industry	470	379
Oil and Gas Processing	not available	50
Other Sources	90	33
Biomass		
Bioethanol and Bioenergy	303	91
Total	7.887	13.466

The United Nations Framework Convention on Climate Change (UNFCCC) adopted the Kyoto Protocol at the conference in 1997. This international environmental agreement was one of the most important milestones in climate protection and includes the first fixed emission reduction goals (particularly CO₂) for industrialized countries. Increasing the share of renewable energy sources on the one hand and the improvement of the energy efficiency on the other hand can contribute substantially to climate protection [1].

The use of fossil fuels in ultra-supercritical (USC) power generating industries will be indispensable; the main focus will be therefore on increasing net plant efficiencies in order to decrease the CO₂ emission. Figure 3 shows the correlation between net plant efficiency, CO₂ reduction and CO₂ emission [2].

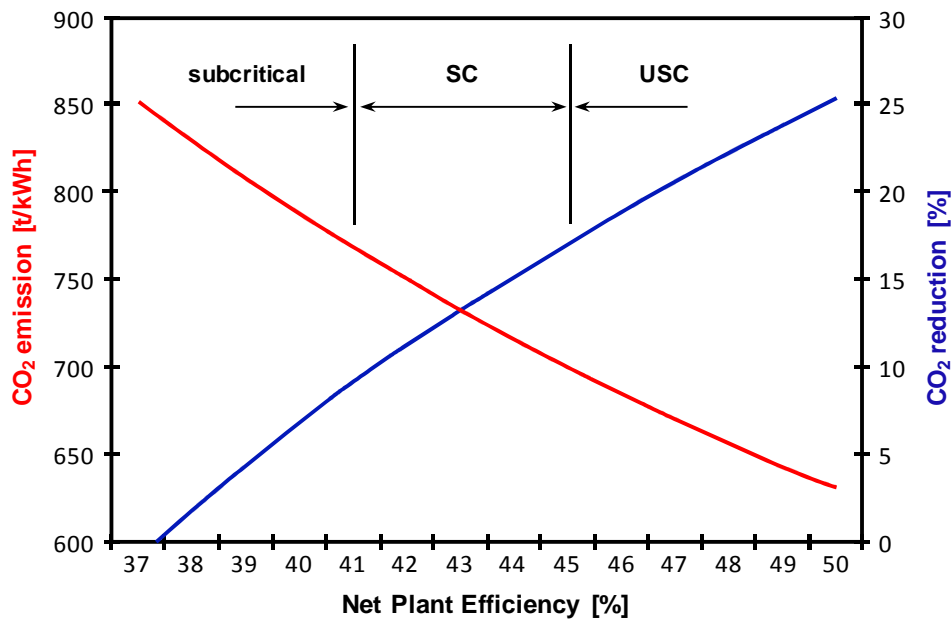


Figure 3: CO₂ emission reduction by increasing efficiency in pulverized coal plants. Compiled by the author and based on G. Booras, EPRI^a [2].

Note: 2% net plant efficiency gain = 5% CO₂ emission reduction

High thermal efficiencies signify an increase of the steam pressures and steam temperatures up to 650°C. This fact forces the industry to the development of new innovative concepts in terms of reliable creep-resistant critical components

^a Electric Power Research Institute, California - USA

such as blades, bolts, steam turbines, valves, tubings and pipings used in USC power stations.

3.2 Definition of Creep

The term “creep” generally denotes a time-dependent plastic deformation of materials at elevated temperatures often greater than $0.4T_m$ under certain loads. This can be either described by creep tests at constant stresses, or with rarely conducted relaxation tests at constant strain-rates.

3.2.1 Creep Curves

Creep curves obtained from the creep tests at constant stresses are plotted as creep-strain vs. time as shown in Figure 4 for an engineering steel [6, 7].

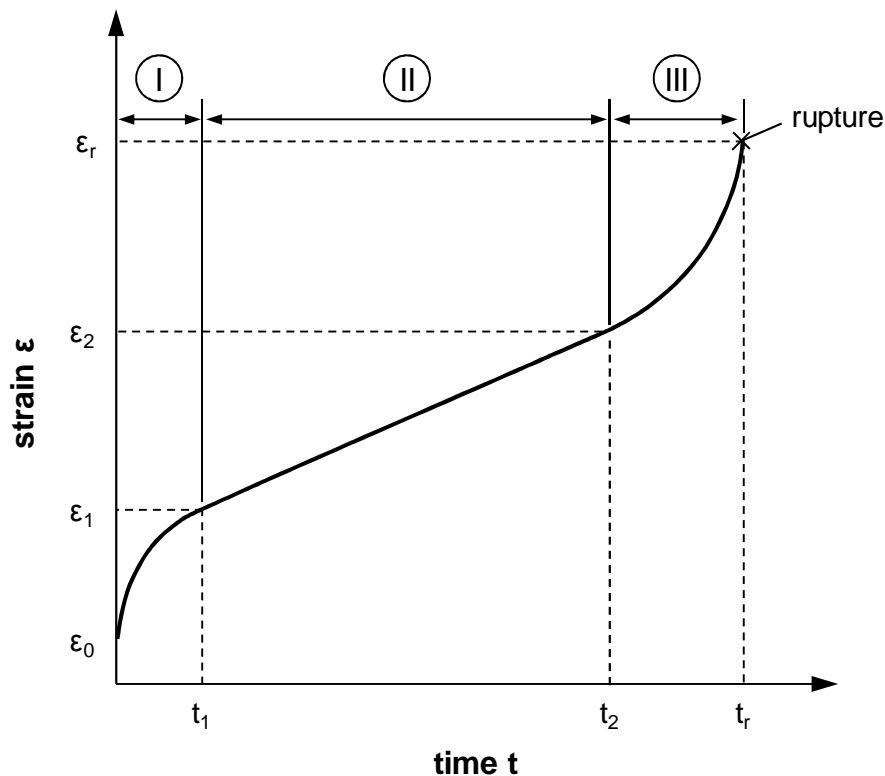


Figure 4: Typical creep curve of an engineering steel at constant load and temperature. Compiled by the author and based on [7]

The creep curve can be divided into three distinct sections Stage I, II and III: Stage I (primary or transient creep) between ϵ_0 and ϵ_1 is characterized by a

decline of the creep-rate $\dot{\epsilon} = d\epsilon/dt$ with time, attributable to strain hardening or to a decrease of the number of dislocations. Within the regime of Stage II (secondary or steady-state creep) the creep-rate stays nearly constant where a dynamic balance between hardening and recovery is approached. The profile at Stage III (tertiary or acceleration creep) shows again an increase of the creep-rate $\dot{\epsilon}$ up to a time t_r where the specimen ruptures. Here, an increase of the stress can be observed as a result of the reduced load-bearing cross-section. This effect is induced by the necking phenomena during creep. These include dynamic recovery or recrystallization as well as coarsening of precipitates which lead to the formation of creep voids ultimately causing cracks and fractures. In some cases the primary creep stage may directly go over to Stage III (two-stage creep-curves). Furthermore, it should be noted that the strain increases and the time to rupture decreases as the testing stress and temperature is increased [6, 7].

A detailed description of creep mechanisms and effects give references [6, 8].

3.3 Development of 9-12% Cr-Steels for Critical Components

New R&D activities on materials research such as the European COST (Cooperation in Science and Technology) have been initiated to develop materials for steam power plants. Thus, the ORNL in the U.S., for instance, developed the modified 9CrMo steel grade “P91” (X10CrMoVNb9-1) characterized by a lower carbon content and additions of niobium (Nb) and nitrogen (N). This material was about to replace the broadly used martensitic “X20”-steel (X20CrMoV12-1) which has been utilized for over 30 years. P91 showed superior creep properties after long-term creep tests at higher temperatures than X20. This technical progress formed the basis for further developments and showed high improvement potentials in materials properties at even higher temperatures and efficiencies. Nippon Steel in Japan developed the steel “NF616”, also known as “P92” with an addition of 1.8% tungsten (W) and a reduced molybdenum (Mo) - content to 0.5% which resulted in a significant creep rupture strength. Also the first COST 501-program (1983-1997) enabled the development of the modified 1% W-containing 9-12%Cr steel

“E911” with improved properties. The creep strengths at 600°C of forging and casting alloys and pipe steels were about 20% higher than the values of P91. Due to these very good high-temperature properties these steels are well-established and are still successfully used in power generation plants [12-16]. An overview of the chemical composition of these discussed martensitic 9-12% Cr-steels gives Table 2.

Table 2: Chemical Composition of X20 [3], P91 [9], P92 [10] and E911 [11]

		Analysis (wt. %)													
		C	Si	Mn	P	S	Cr	Mo	Ni	V	W	Nb	N	Al	B
X20	min	0.17	-	1.00	-	-	10.00	0.80	0.30	0.25					
	max	0.23	0.50		0.03	0.03	12.50	1.20	0.80	0.35					
P91	min	0.08	0.20	0.30	-	-	8.00	0.85	-	0.18		0.06	0.03	-	
	max	0.12	0.50	0.60	0.02	0.01	9.50	1.05	0.4	0.25		0.10	0.07	0.04	
P92	min	0.07	-	0.30	-	-	8.50	0.03	-	0.15	1.50	0.04	0.03	-	0.001
	max	0.13	0.05	0.60	0.02	0.01	9.50	0.60	0.4	0.25	2.00	0.09	0.07	0.04	0.006
E911	min	0.09	0.10	0.30	-	-	8.50	0.90	0.10	0.18	0.90	0.06	0.05	-	0.0005
	max	0.13	0.50	0.60	0.02	0.01	9.50	1.10	0.40	0.25	1.10	0.10	0.09	0.04	0.0050

Following the COST action 522 “Materials for Advanced Power Engineering” (1998-2003) was the subsequent step for the development of new steels with boron (B) for power plants at steam and reheat temperatures of 610°C and 630°C [12]. The Cr content had to be increased to 11% to ensure sufficient oxidation resistance at elevated steam conditions. High Cr containing steels tend to form delta-ferrite at high temperatures which has a negative impact on the mechanical properties. It has been demonstrated that the presence of delta-ferrite decreases the creep rupture strength significantly [13]. Austenite stabilizing elements such as copper (Co) is added to reduce the delta-ferrite formation in the martensitic structure [13, 14, 15]. Therefore it was possible to achieve similar creep strengths of 9%Cr steels.

Within the European Initiative COST 536 (2004-2009) the project with the title “Alloy development for Critical Components of Environmental friendly Power plantTs” (ACCEPT) was introduced with the aim of achieving even greater plant efficiencies and lower emissions. This project had the objective to determine the relation between the microstructure and creep properties at

temperatures up to 650°C [16]. The corresponding creep curves are shown below in Figure 5.

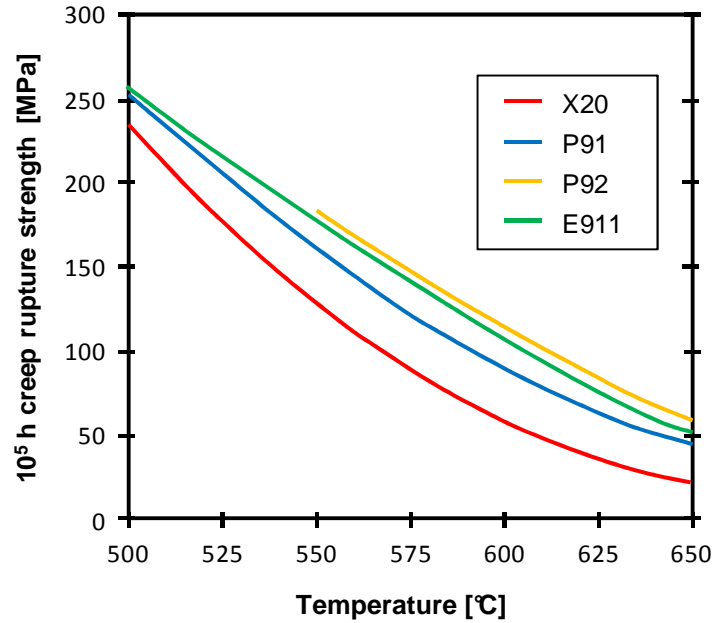


Figure 5: Creep rupture strength of conventional power plant steels. Based on reference [14]

Especially worth mentioning is the tempered martensitic steel grade 9Cr3W3CoVNbBN (NPM1) which was developed by the Institute for Materials Science and Welding (IWS) at Graz University of Technology in collaboration with the National Institute for Materials Science (NIMS) in Japan supported by COST 536 [17]. This steel was specifically developed to overcome the deterioration of the creep rupture strength in the HAZ of welded components. The chemical composition is given in the following table. The chemical composition of NPM1 is given in the following table.

Table 3: Chemical Composition of NPM1 [13]

	Analysis (wt. %)							
	C	Si	Mn	P	S	Cr	Ni	V
NPM1	0.074	0.29	0.44	0.009	0.004	9.26	0.06	0.21
	W	Nb	N	Al	B	Co	Ti	
	2.84	0.056	0.013	<0.005	0.012	2.95	<0.005	

A modified variant NPM4 (see experimental setup, chapter 6.1) was also developed to improve the high-temperature properties and would be the first choice for future in-situ studies. The creep-tests are still running and show very promising performances.

Balanced additions of boron and nitrogen showed auspicious properties in terms of an improved creep behavior and high oxidation resistance despite the relative low chromium content of max 9% [17]. A controlled addition of N and B stabilizes the martensitic microstructure of the material significantly which results in a better creep rupture strength. The coarsening of certain precipitates during service such as $M_{23}C_6$ around the prior austenite grain boundaries (PAGB) at elevated temperatures supports the evolution of inhomogeneous distributions of precipitates within the microstructure and basically has a negative impact on the materials. Boron suppresses these coarsening effects and decelerates the creep rate. Surplus added amount of boron combined with nitrogen, on the other hand, tend to form boron nitride (BN) precipitates, which may reverse this positive effect [13, 18].

However, special attention has to be paid mainly to creep-strengthening mechanisms such as solid solution, dislocation, sub-boundary, precipitation or dispersion hardening in martensitic 9-12%Cr steels. This can be achieved e.g. by finely dispersed and stable precipitates (for example MX carbonitrides) within the base material, at grain boundaries, as well as in the HAZ, which impede the movement of dislocations and thus increase the long-term creep strength [13, 18]. The most frequent and typical precipitates in 9-12%Cr steels, their compositions and crystal structures are given in Table 4. The chemical compounds are generally given as M_iX_j (M = metallic element, X = carbon/nitrogen) [18].

Table 4: Precipitates in 9-12% Cr steels [19]. fcc = face-centered cubic

Precipitation	Composition	Crystal structure
	VN: (V,Nb)(N,C)	fcc
MX	VC: (V,Nb)(N,C)	fcc
	NbC: (Nb,V)(C,N)	fcc
M ₂₃ C ₆	(Cr,Fe,Mo,W) ₂₃ C ₆	fcc
M ₇ C ₃	(Fe,Cr,Mo) ₇ C ₃	orthorhombic
M ₂ X	Cr ₂ N	hexagonal
M ₃ C	(Fe,Cr) ₃ C	orthorhombic
M ₆ X	(Fe,Cr,Mo) ₆ (C,N)	fcc
M ₃ B ₂	(Mo,Nb,Fe,Cr) ₃ B ₂	tetragonal
BN	BN	triclinic/hexagonal/ cubic/orthorhombic
AlN	AlN	hexagonal
Laves-phase	(Fe,Cr,Si) ₂ (Mo,W)	hexagonal
Z-phase	CrNbN	tetragonal
mod. Z-phase	Cr(Nb,V)N	tetragonal

Particularly noteworthy is the formation of the Z-phase which causes the dissolution of fine MX particles during long-term creep exposure. This phase is predominantly responsible for the tremendous loss in materials creep strength after long periods in service. The intermetallic Laves-phase on the other hand, which is promoted by the presence of Mo and W, arises during service (< 3000h) as well and tends to reduce the creep strength too. This can be explained by the fact that the removal of Mo and W has a negative impact on the mechanism of solid solution strengthening. A further interesting aspect is the effect of delta-ferrite in tempered martensitic 9-12% chrome-steels. The presence of delta-ferrite diminishes the overall dislocation density of the materials and therefore contributes to a decrease of the creep strength. Nevertheless, the challenging factors in the development and improvement of

novel creep- and heat-resistant steels will be mainly in the avoidance and prevention of certain unwanted populations of precipitates and the coarsening effects of the existing fine dispersed particles [14, 13, 18, 19].

3.4 Welded Joints in Martensitic 9%Cr Steels

Welding processes strongly influence the metallurgical properties of the base material within the HAZ (see next paragraph) which may result in a considerable decrease of the creep rupture strength due to the inhomogeneous heat inputs. Figure 6 shows a schematic sketch of the subzones of the HAZ due to the welding procedure and the related calculated equilibrium phase diagram of the steel grade P91 [13].

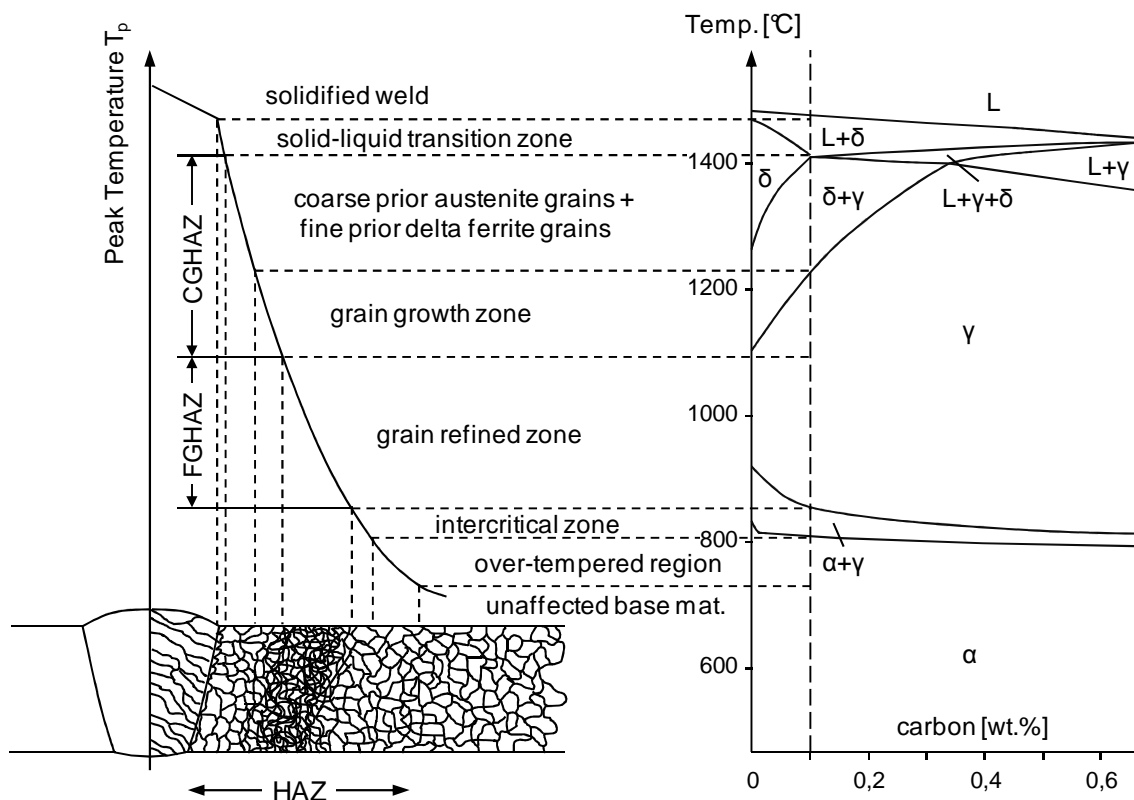


Figure 6: Schematic illustration of the HAZ and the corresponding phase diagram of P91. CGHAZ = coarse-grained HAZ; FGHAZ = fine-grained HAZ. Compiled by the author and based on ref. [13]

Different appropriate process parameters such as heating and cooling rate, peak temperature, dwell time and post-weld heat treatment (PWHT) as well as the influences of multilayer weldings define the microstructural evolution and

therefore the mechanical properties of the welded components. The heating rate, for instance, influences the phase transformation and recrystallization temperatures, solution temperature of precipitates and the grain growth behavior [13].

3.4.1 The Heat Affected Zone

As demonstrated in the previous section, the HAZ can be classified into various subzones, extending from the fusion zone, the coarse- and fine-grained HAZ, intercritical zone, over-tempered region and finally to the unaffected base steel. These zones are described in the following according to [3, 14, 13].

- **Coarse-grained zone**

This zone ranges over the region just beside the molten material with temperatures below T_m and above A_{C3} , in the higher temperature fields of the austenization area. It is marked by the dissolution of the particles causing the formation of coarse prior austenite grains as well as fine prior delta-ferrite grains. Furthermore, the zone is characterized by its high hardness and low toughness properties.

- **Fine-grained zone**

At temperatures below $T_{\gamma\delta}$ (temperature at which delta-ferrite transformation is complete on heating) and just above A_{C3} , usually around 1100°C, the material shows a fine-grained microstructure, in which some of the precipitates are not fully dissolved and hinder the grain growth. Obviously, this region seems to be the weakest link of welded structures, where the components break down due to Type IV cracking (see later).

- **Intercritical zone**

The region indicates incomplete α to γ transformations at ordinary temperatures between A_{C1} and A_{C3} (“partially transformed zone”) featuring an untempered and overtempered fine-grained microstructure. Here, partially dissolved particles and a coarsening of the remaining precipitates

are observable during the heat input. It cannot be ruled out that the components may experience type IV failures in this zone.

- **Over-tempered region**

No further phase transformations, but a local tempering during the welding process can be perceived at temperatures below A_{C1} and above the original tempering temperature of the base metal.

- **Zone of unaffected base material**

Within the region of the unaffected base steel the microstructure is similar to that of the respective parent material.

Distinctive difficulties in welding seams or rather a noticeable decline of the creep rupture strength compared to the base material have been clearly observed during long-term creep tests, especially at elevated temperatures and lower stress levels. Figure 7 points out the decreased creep strengths of crosswelds at different temperatures in an E911-steel compared to those of the unwelded material [13].

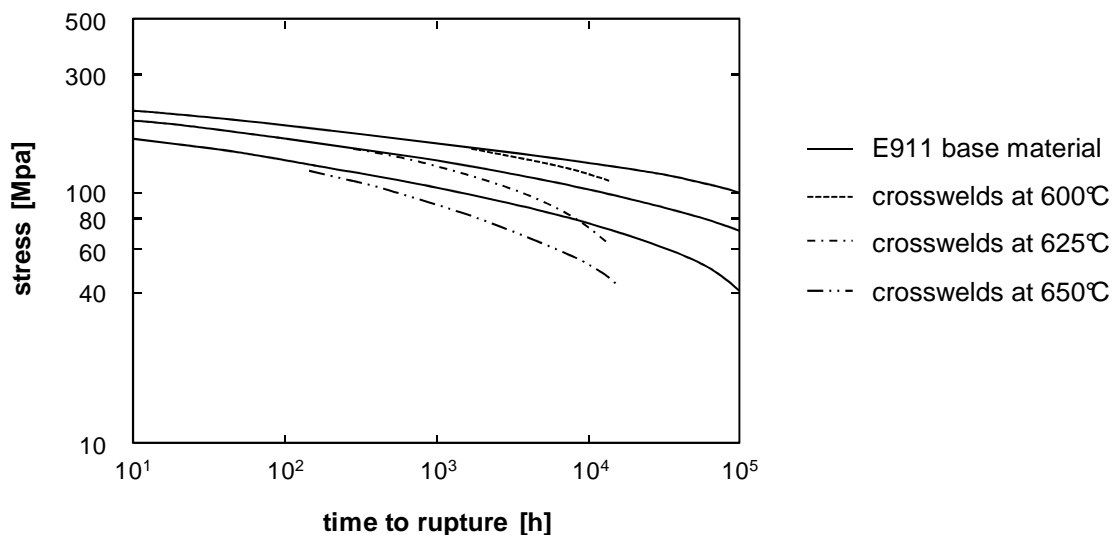


Figure 7: Creep rupture strength of crosswelds at different temperatures compared with the base material of E911. Based on [4]

This may induce premature creep failures such as cracks as will be briefly described in the following.

3.4.2 Cracks in 9%Cr Steel Welds

As a consequence of the reduced creep resistance, diverse in-service crack failures may appear in the welded elements. These cracks can be categorized into four types as demonstrated below.

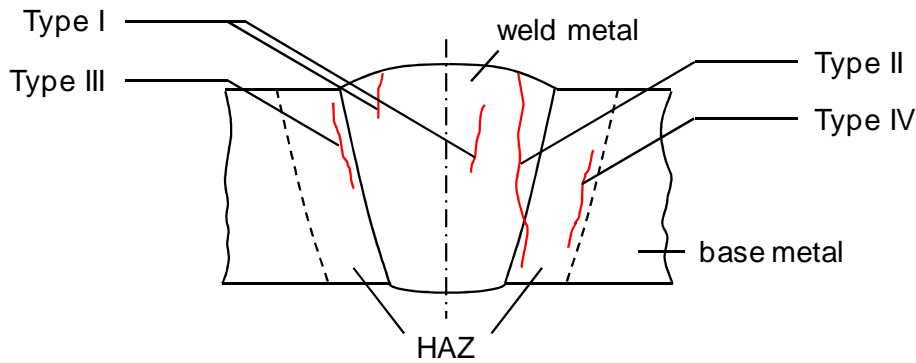


Figure 8: Types of cracks in welded joints. Compiled by the author and based on [13]

Type I and type II crackings, extending both in transversal and longitudinal direction, can be exclusively identified in the weld metal itself, whereas the type II cracks may also spread into the HAZ of the joint. While type III or reheat crackings develop in the CGHAZ, the type IV failure mode is formed in the FGHAZ or intercritical HAZ of the welded steel. A precise description of type I, type II and type III gives reference [13]. In the following, the issue of the type IV mechanism is discussed in more detail.

3.4.2.1 Type IV Cracking

Type IV failures are regarded as the main cause of breakdowns of cross-welded 9%Cr power plant materials during creep tests, particularly at relatively low stresses ($< 100\text{MPa}$), comparable to real service conditions (Figure 9). The complicated phenomenon of the type IV creep fracture predominantly occurs in the fine-grained region or in the intercritical zone of the HAZ, close to the area of the unaffected base metal. Above about 100MPa , the creep strengths of the weldments are quite similar to that of the base material. The microstructural

evolution with increasing service time and temperature is associated with further precipitation and coarsening processes which contribute to the nucleation of creep voids. These are originated e.g. due to the coarsening of retained carbides during the PWHT, which were not fully dissolved by the preceding weld thermal cycle. Furthermore, local suggested multi-axial stresses in the IC/FGHAZ may accelerate the development of these voids [13, 20].

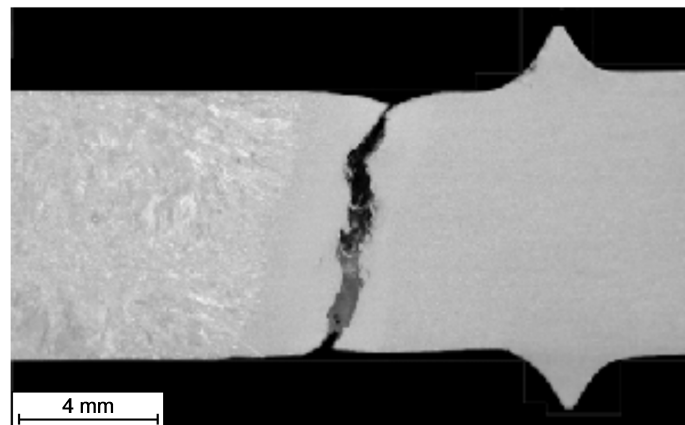


Figure 9: Type IV cracking in a creep-exposed cross-welded E911-sample welded with matching filler, tested at 600°C and 110MPa for 18.000 h [4]

Another very interesting aspect is the role of constraint of creep deformation in the weak type IV region. Various modeling methods gave rise to the suspicion that the constraint is relaxed by the grain boundary sliding. This means the more grain boundary sliding occurs, the greater will be the number of cavities within this area, resulting in poor creep performance of the welded parts [20].

The mechanisms of type IV crackings in martensitic 9%Cr steel welds have not yet been completely clarified. Therefore, many efforts, such as the use of the promising neutron diffraction technique as will be extensively presented in chapter 4, are being made to understand the deterioration of the creep strength behavior of the weldments.

4. Neutron Diffraction to Engineering Problems


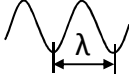
The historical background of neutrons goes back to 1932 when James Chadwick proved the existence of neutrons and received the Nobel Prize “*for the discovery of the neutron*” in 1935 [21]. D.P. Mitchell and P.N. Powers firstly demonstrated the Bragg scattering by crystals in 1936 [22]. Clifford G. Shull and Ernie Wollan also went down in history for the development of the theory of neutron reflection, scattering and diffraction in the mid and late 1940’s. Further important steps in neutron science were taken in 1994 for scattering improvements in the study of condensed matter. “*Neutrons show where the atoms are and what the atoms do*”: C. Shull and Bertram N. Brockhouse won the Nobel Prize in Physics “*for pioneering contributions to the development of neutron scattering techniques for studies of condensed matter*” [21]. They explained the fundamentals of elastic and inelastic scattering of neutrons when colliding with atoms in the sample material [23].

The following subchapters deal with the neutron theory in detail and give an overview of the properties of neutrons, how they can be produced, which measurement techniques already exist and how neutron diffraction can be applied to engineering problems.

4.1 Properties of Neutrons

Neutrons are uncharged (neutral) particles with a mass of $m_n = 1.67 \times 10^{-27}\text{kg}$ and a radius of $r_0 = 6 \times 10^{-16}\text{m}$. The spin is equal $\frac{1}{2}$ and the magnetic dipole moment can be described with $\mu = 1.9 \times \mu_N$, whereas μ_N is the nuclear magneton. The neutron has particle-like as shown above and at the same time wave-like properties. This uniqueness is represented by following formulas [24]:

Table 5: Particle and wave properties of neutrons

	
momentum $\vec{p} = m_n \cdot \vec{v}$ (1. 1)	wavelength $\lambda = \frac{h}{m_n \cdot v}$ (de Broglie) (1. 2)
\vec{v} ... velocity	h ... Planck's constant
energy $E = \frac{m_n \cdot v^2}{2}$ (1. 3)	wavevector $k = \frac{2\pi}{\lambda}$ (1. 4)
	momentum $\vec{p} = \frac{h \cdot \vec{k}}{2\pi} = \hbar \cdot \vec{k}$ (1. 5)
	reduced Planck's constant $\hbar = \frac{h}{2\pi}$ (1. 6)
	energy $E = \frac{h^2}{2m_n \cdot \lambda^2} = \frac{\hbar^2 \cdot k^2}{2m_n}$ (1. 7)

4.1.1 Why use Neutrons?

The zero charged neutrons can be used as non-destructive particles in materials testing methods and allow the study of samples in high temperature or pressure environments. An important characteristic of neutrons is the high penetration capacity which facilitates the analysis of big and complex parts in various research projects.

Another specialty is the wavelength similarity of neutrons to interatomic spacings. Thus, crystal structures, structural sensitivities and atomic spacings of the sample can be determined. Neutrons interact with the atomic nucleus (neutrons and protons) and have a sensitivity to light atoms. This unique property enables neutrons to detect positions of hydrogen and deuterium atoms/bonds which are practically invisible for x-rays. A further advantage of neutrons can be seen in the ability of the use of contrast variations to differentiate complex molecule structures in biological systems. The energies of

these neutral particles amount a few meV and are similar to those of elementary excitations in matter (phonons and magnons). Both represent analogical molecular dynamics and lattice vibrations. Neutrons have a magnetic moment and are highly sensitive to magnetic fields. Therefore, they are scattered on magnetic lattices and can hence be utilized as an important tool to study microscopic magnetic structures and fluctuations. Apart from the properties as previously stated, neutrons possess a spin to form polarized neutron beams and to investigate magnetic structures and motions as well [24].

All these facts make diffraction using neutrons very promising as a complementary and attractive tool compared to other materials testing techniques.

4.2 Neutron-Producing Reactions

Basically there are two ways to create neutron beams for experimental scattering: On the one hand by means of nuclear fission (steady-state) reactors and on the other hand by spallation sources. Moreover, both processes are cost-intensive and difficult to execute as e.g. X-ray sources.

4.2.1 Nuclear Fission

A controlled nuclear fission process is performed when a slow thermal neutron hits an isotope, primary uranium (^{235}U), and cleaves it into two almost equally sized nuclei. ^{235}U is the only naturally occurring substance which can be split by slow neutrons, other isotopes have to be produced artificially and cost-intensive (e.g. plutonium ^{239}Pu – note: “the most toxic substance on earth” [25]). Each reaction generates a total energy about 200MeV and an average of 2.5 neutrons: 1 neutron initiates further fission processes and triggers the chain reaction (has to be moderated to a thermal neutron), 0.5 is lost by absorption and eventually 1 neutron per nuclear fission is useful for scientific purposes [24, 26]. Figure 10 illustrates this event, its fission products and the generated heat energy.

Equation for nuclear fission: ${}_0^1\text{n} + {}_{92}^{235}\text{U} \rightarrow {}_{56}^{144}\text{Ba} + {}_{36}^{89}\text{Kr} + 2(3){}_0^1\text{n} + 177\text{MeV}$ [24]

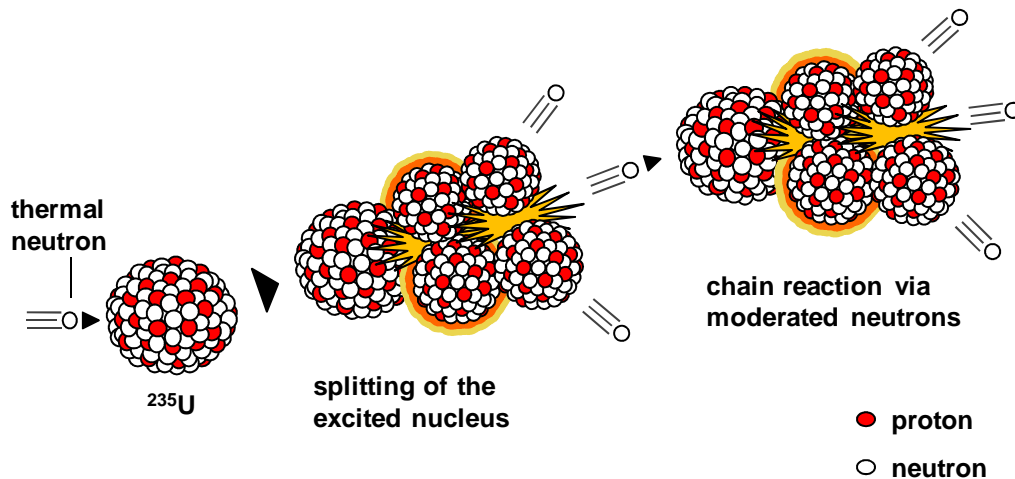


Figure 10: Fission. Compiled by the author and based on [24]

4.2.2 Spallation

The second method for neutron production is the so-called spallation: High-energy protons with about 1GeV impinge on a heavy metal target with great mass numbers (Pb, W, Hg or U) and induce a highly excited nucleus. By-products such as protons, neutrons as well as pions (π) also emerge due to this collision process and cause additional excitations of the nuclei. Furthermore, the highly excited nucleus releases the energy to reach an equilibrium by evaporating neutrons, positrons (e^+) and gamma radiation (Γ). Dependent on the used targets, the average number of released neutrons amounts around 20 for each reaction [26]. The event is shown in the figure below.

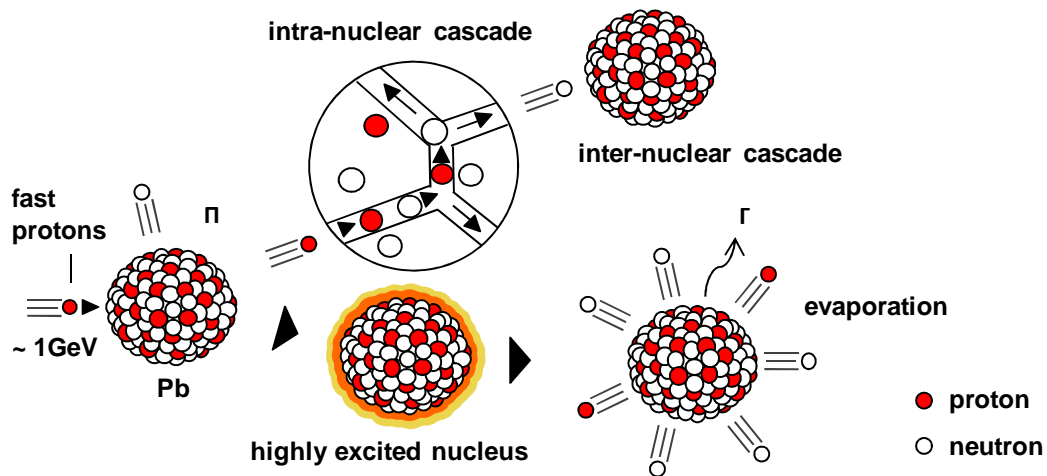


Figure 11: Spallation. Compiled by the author and based on [24]

Fast (hot) neutrons, both in spallation or nuclear fission, have energies of a few MeV and need to be decelerated in moderators. Cold, thermal and hot neutrons have their own characteristics in terms of wavelength and beam flux distribution [26]. The greater the energy of the neutrons, the hotter and faster they get and the shorter their wavelength. Useful research experiments require specific wavelength distribution spectra of the neutron flux. This can be achieved by cooler neutrons around room temperature. The moderation can be either done with water ($\text{H}_2\text{O}/\text{D}_2\text{O}$) or beryllium (Be) for thermal neutrons, liquid or heavy hydrogen (H_2 or D_2) for cold neutrons or with graphite in the case of hot neutrons [26].

The following table points out the relation of the energies, temperatures, velocities and wavelengths of each modification [23]. Note: 0.1nm (1\AA) roughly corresponds to the atomic distance in molecules and solids.

Table 6: Relation of energy, temperature and wavelength of hot, thermal and cold neutrons

neutrons	energy [meV]	temperature [K]	velocity [m/s]	wavelength [\AA]
hot	100 - 500	1000 - 6000	~ 5000	0.4 - 1
thermal	5 - 100	60 - 1000	~ 2200	1 - 4
cold	0.1 - 10	1 - 120	~ 700	4 - 30

Heat generation and heat removal limit the performance of fission reactors compared to spallation sources. Nevertheless, the challenging factors in neutron generators are shielding and irradiation issues in the target window to meet the highest standards of safety and environmental protection set by the government and national policies.

4.2.3 Pulsed vs. Steady-State Neutron Sources

Steady-state reactors generate continuous neutron beam fluxes showing a Maxwell-Boltzmann distribution spectrum which can be characterized by time-average integration. Pulsed sources like the SNS are characterized by the high peak neutron flux of which the energies are intended by time-of-flight detection. The technology has a beneficial time structure for many applications and is rapidly evolving. Another advantage is the licensing factor compared to reactors, which are e.g. not licensable in the western United States [22]. The rising trend towards neutron spallation sources is confirmed in Figure 12.

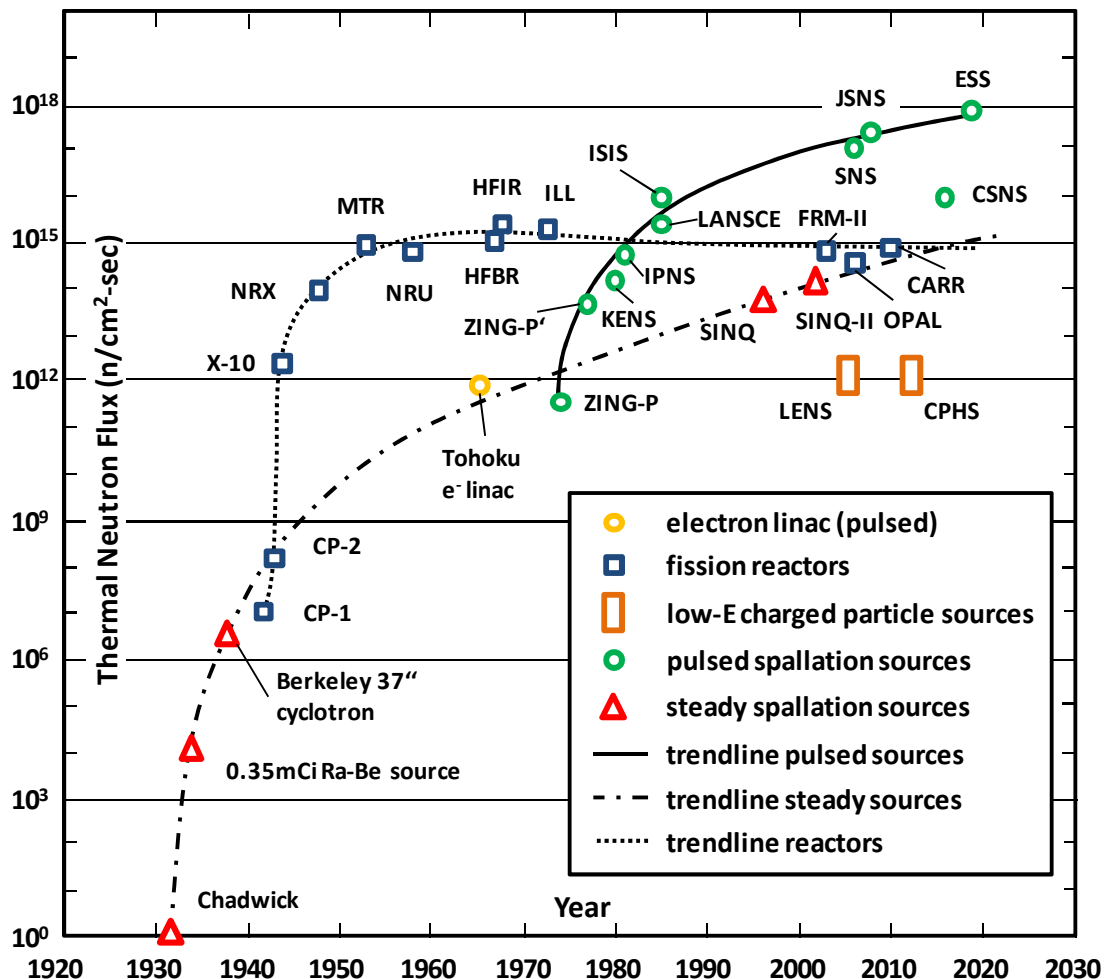


Figure 12: Development of neutron science facilities (Compiled by the author and based on “Neutron Sources for Materials Research” – J.M. Carpenter, updated version) [22]

4.2.4 Pulsed Spallation Neutron Sources

The zero gradient synchrotron (ZGS) intense neutron generator- prototype (ZING-P) with a proton energy of 200MeV was the first of its kind and was put into operation in 1974. Further developments of the existing devices and instruments of ZING-P have led to the construction of the improved ZING-P', which provided the ability to carry out first scientific experiments (originated in 1977 and shut down in 1980). An overview of the past, existing and future pulsed neutron spallation sources (green open circles), their primary parameters and characteristics in chronological order is given in Appendix A.

4.3 Principles of Neutron Scattering

This subchapter covers the fundamentals of the neutron scattering theory and gives a brief overview about the interaction of atoms and neutrons in general. The structure and dynamics of materials can be examined by either elastic or inelastic scattering which will be described in chapter 4.3.5.

4.3.1 Neutron Scattering Cross Sections

Since every neutron scattering experiment is principally based on the measurement of the cross sections, it is essential to define these quantities in a comprehensive manner. Figure 13 shows the principle of neutron scattering, where incoming neutrons are scattered by a sample into a solid angle $d\Omega$.

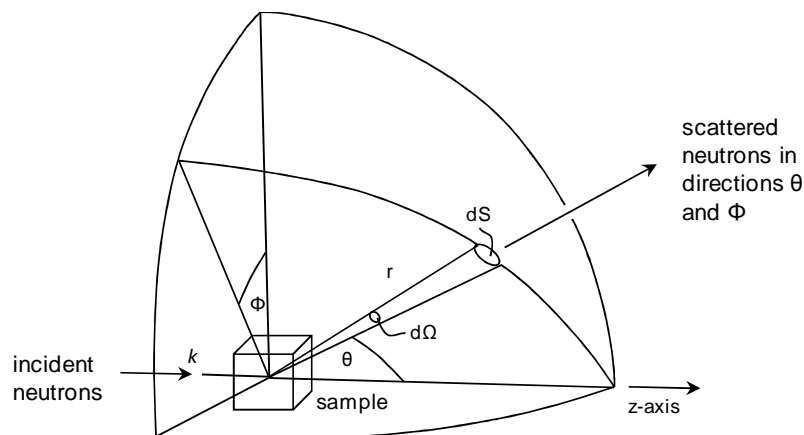


Figure 13: Geometry for a scattering experiment. Based on [27]

The cross section is the effective area of a scattering system (e.g. crystals) which absorbs or scatters a certain number of incident neutrons. The neutron beam flux Φ is defined by the number of incoming neutrons per unit area perpendicular to the incoming beam direction per second [n/cm²/sec]. Furthermore, the neutron scattering cross section σ is the capability of neutrons being scattered by a sample and is given by

$$\sigma = \frac{\text{number of neutrons scattered per second}}{\Phi}. \quad (1.8)$$

In atomic and nuclear physics, σ is commonly measured in barns (1 barn = 10⁻²⁴ cm²). Imagining that the neutrons are scattered into a small differential solid angle $d\Omega$ orientated in the directions θ , Φ and no energy to be analyzed is taken into account (= elastic scattering, see 4.3.5), the differential scattering cross section can be defined as

$$\frac{d\sigma}{d\Omega} = \frac{\text{number of neutrons scattered per second into angle } d\Omega}{d\Omega}. \quad (1.9)$$

Considering the energy transfer in the case of inelastic scattering (4.3.6), the equation is known as the partial differential scattering cross section:

$$\frac{d^2\sigma}{d\Omega dE} = \frac{\text{number of neutrons scattered per second into } d\Omega \text{ and } dE}{\Phi d\Omega dE}. \quad (1.10)$$

The total number of neutrons scattered in all directions is expressed as

$$\sigma_{\text{tot}} = \int \left(\frac{d\sigma}{d\Omega} \right) d\Omega \quad (1.11)$$

$$\text{and } \sigma_{\text{tot}} = \int_0^\pi \frac{d\sigma}{d\Omega} 2\pi \sin \theta d\theta \quad (1.12)$$

in the case of axially symmetric elastic scattering.

All these definitions and equations of scattering cross sections are valid for all types of scattering techniques [27].

4.3.2 Scattering by a single fixed Nucleus

The function of the incident plane wave along z (z -axis parallel to the incident wavevector k_i as shown in Figure 14) is expressed as

$$\psi_i = e^{ikz}. \quad (1.13)$$

If the incident wave strikes a single fixed nucleus, the outgoing scattered wave is then a spherical wave with the function

$$\psi_s = \frac{-b}{r} e^{ikr}, \quad (1.14)$$

where b denotes the neutron scattering length (the negative sign represents a positive value of b for repulsive interactions). It depends on the type of the nuclei and on the nuclear spin both of the nucleus and neutron. The nucleus has two scattering length values (coherent and incoherent parts – see later) if the spin of the nucleus is not equal to zero. If the nuclide has a spin = 0, then it will only have one value for the (coherent) scattering length.

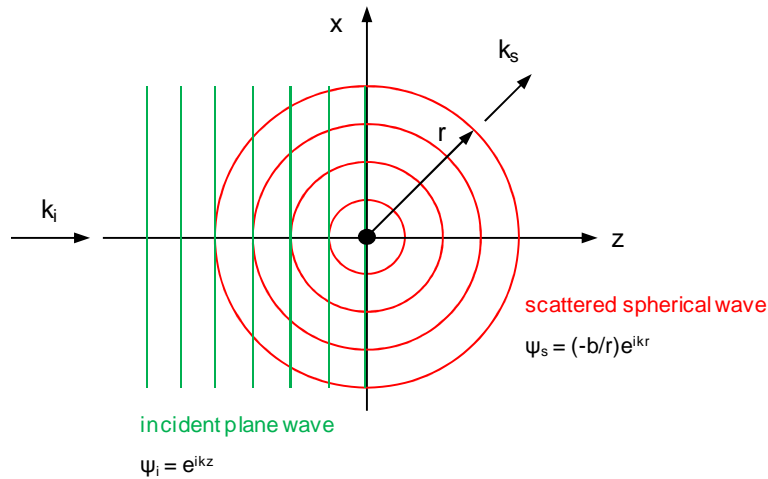


Figure 14: Scattering from a single fixed nucleus. Based on [24]

Further formulations for this simple case include the equation for number of neutrons per second through dS , which can be defined by

$$dS|\psi_s|^2 = vdS \frac{b^2}{r^2} = vb^2 d\Omega, \quad (1.15)$$

where v is the neutron velocity ($v_i = v_s$). The incident neutron flux is given as

$$\Phi = v|\psi_i|^2 = v. \quad (1. 16)$$

By inserting (1. 15) into the definition of (1. 9) the neutron differential cross section for the simple case can be written as

$$\frac{d\sigma}{d\Omega} = \frac{vb^2d\Omega}{\Phi d\Omega} = b^2, \quad (1. 17)$$

and finally for the total neutron scattering cross section

$$\sigma_{\text{tot}} = 4\pi b^2. \quad (1. 18)$$

4.3.3 Scattering by many Nuclei

This subchapter covers the fundamentals of scattering by many nuclei in order to define the wavevector transfer Q , also known as the momentum transfer, which is the basic module for diffraction experiments such as small angle neutron scattering (SANS) for characterizing nanoparticles (chapter 4.5).

The incident wave, located at R_i , is given as

$$\psi_i = e^{i\vec{k}_i\vec{R}_i}, \quad (1. 19)$$

the outgoing scattered wave at r is

$$\psi_s = \sum e^{i\vec{k}_i\vec{R}_i} \left[\frac{-b_i}{|\vec{r} - \vec{R}_i|} e^{i\vec{k}_s(\vec{r} - \vec{R}_i)} \right]. \quad (1. 20)$$

Using equations (1. 15) and (1. 17) the differential cross section is

$$\frac{d\sigma}{d\Omega} = \frac{dS}{d\Omega} \left| b_i e^{i\vec{k}_s\vec{r}} \sum \frac{1}{|\vec{r} - \vec{R}_i|} e^{i(\vec{k}_i - \vec{k}_s)\vec{R}_i} \right|^2. \quad (1. 21)$$

Further, by measuring far away so that $r \gg R_i$, the expression $d\Omega = dS/r^2$ can be used for (1. 17)

$$\frac{d\sigma}{d\Omega} = \sum_{i,j} b_i b_j e^{i(\vec{k}_i - \vec{k}_s)(\vec{R}_i - \vec{R}_j)} \quad (1. 22)$$

and finally

$$\frac{d\sigma}{d\Omega} = \sum_{ij} b_i b_j e^{i\vec{Q}(\vec{R}_i - \vec{R}_j)} \quad (1. 23)$$

by introducing the scattering vector Q as $k_i - k_s$ [24].

4.3.4 Coherent and Incoherent Neutron Scattering

Neutron scattering experiments are influenced by the variation of the spin states of the neutrons with the atomic nucleus. Thus, one has to distinguish between the coherent and incoherent scattering. The first is Q -dependent and reveals information about the interference between the scattered waves of a neutron from all the component's nuclei. The latter does not depend on the scattering vector and is uniform in all directions with no interferences. Therefore, the scattering cross section from (1. 23) can be separated into two terms:

$$\sum_{ij} b_i b_j e^{i\vec{Q}(\vec{R}_i - \vec{R}_j)} = \sum_{ij} \langle b \rangle^2 e^{i\vec{Q}(\vec{R}_i - \vec{R}_j)} + \sum_i (\langle b^2 \rangle - \langle b \rangle^2) e^{i\vec{Q}(\vec{R}_i - \vec{R}_j)}. \quad (1. 24)$$

and
$$\frac{d\sigma}{d\Omega} = \left[\frac{d\sigma}{d\Omega} \right]_{\text{coh}} + \left[\frac{d\sigma}{d\Omega} \right]_{\text{inc}}, \text{ respectively.} \quad (1. 25)$$

Using the right side of equation (1. 24) the (bound) coherent and incoherent scattering lengths can now be introduced as

$$\langle b \rangle = b_{\text{coh}} \quad (1. 26)$$

and
$$\sqrt{\langle b^2 \rangle - \langle b \rangle^2} = b_{\text{inc}}. \quad (1. 27)$$

Considering the equation for the total neutron scattering cross section (1. 18), the coherent and incoherent scattering cross sections can be defined as

$$\sigma_{\text{coh}} = 4\pi \langle |b_{\text{coh}}|^2 \rangle \quad (1. 28)$$

and
$$\sigma_{\text{inc}} = 4\pi \langle |b_{\text{coh}}|^2 \rangle [24, 28]. \quad (1. 29)$$

The coherent and incoherent scattering lengths and cross sections for elements and isotopes being used in martensitic 9-12% Cr-steels are listed in Appendix B.

4.3.5 Elastic Neutron Scattering

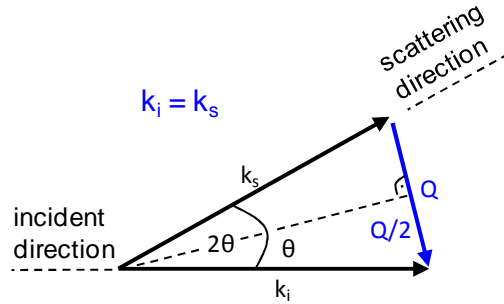


Figure 15: Elastic neutron scattering

Elastic scattering is characterized by the change in direction of the neutrons when they strike the atoms of the sample part as shown in Figure 15. They have the same energy before and after being scattered. The scattering vector Q as previously been presented is given by

$$\vec{Q} = \vec{k}_i - \vec{k}_s \quad [\text{nm}^{-1}] \quad (1.30)$$

with k_i and k_s as the incident and scattered wavevectors. Using the triangle of the figure above the scattering vector can be defined as

$$\vec{Q} = 2\vec{k} \cdot \sin \theta. \quad (1.31)$$

With (1.4) the equation for Q finally changes to

$$\vec{Q} = \frac{4\pi \cdot \sin \theta}{\lambda}. \quad (1.32)$$

Elastic neutron scattering instruments include diffractometers for the study of e.g. atomic orderings, texture and strain/stress states, and reflectometers in the case of surface investigations.

Diffractometers, both in pulsed and steady-state neutron sources, are

- powder diffractometers
- single-crystal diffractometers and
- small-angle neutron scattering (SANS) instruments.

4.3.6 Inelastic Neutron Scattering

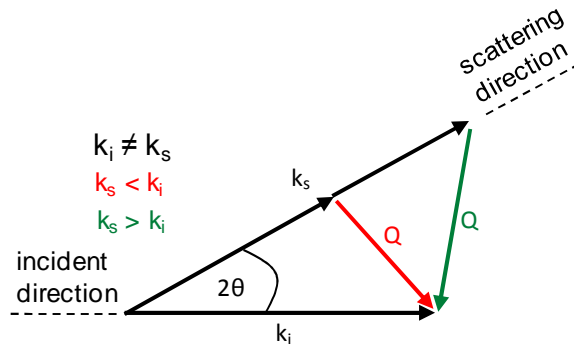


Figure 16: Inelastic neutron scattering

Inelastic neutron scattering shows an exchange of the neutron energy and momentum when colliding with the sample material (Figure 16). The neutron gains energy if $k_s > k_i$, and vice versa. The energy change is calculated with the equation

$$\Delta E = E_i - E_s = \frac{\hbar^2}{2m} (\vec{k}_i^2 - \vec{k}_s^2). \quad (1.33)$$

Frequencies of excitations, magnetic and atomic/molecular dynamics and other dynamic phenomena can be observed with spectrometers by inelastic neutron scattering.

These include

- triple-axis instruments principally at steady-state neutron sources
- chopper instruments
- diffuse scattering instruments
- spin echo instruments and
- backscattering instruments [29].

A very good description of neutron instrumentations can be found in [30]. Neutron diffraction will be addressed next.

4.4 Neutron Diffraction

Neutron diffraction is a very sophisticated elastic neutron scattering method to investigate extensive materials properties in engineering and will also be used for the purpose of this work. The technique is based upon Bragg's law which allows determining the location of individual atoms in the unit cell:

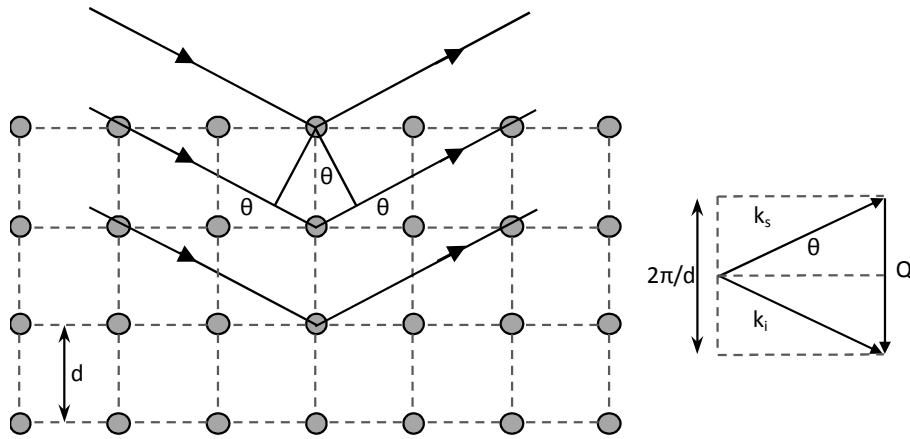


Figure 17: Bragg-diffraction on a crystal

Bragg diffraction from an ideal crystal appears when the scattering vector Q is perpendicular to the lattice planes corresponding to the reciprocal lattice vector as shown in Figure 17. Its value is

$$Q = \frac{2\pi}{d}. \quad (1.34)$$

Inserting (1.34) into (1.32) and having a constructive interference of the incident and scattered neutrons leads thus to the Bragg's equation

$$\lambda = 2d_{hkl} \sin \theta_{hkl}, \quad (1.35)$$

and accordingly
$$d_{hkl} = \frac{\lambda}{2 \sin \theta_{hkl}}, \quad (1.36)$$

where θ_{hkl} is the diffraction angle, λ the wavelength and d_{hkl} the interplanar spacing between planes of the Miller indices [29]. This fundamental formula is essential for each diffraction experiment. Neutron diffraction enables e.g. very

accurate strain and consequently stress measurements of specimens by measuring the crystal lattice spacing d_{hkl} . This can be either done with conventional angular scanning instruments for steady-state reactors or with the TOF method for pulsed spallation sources [31]. Since TOF engineering materials diffractometers like VULCAN offer better capabilities and higher efficiencies for crystallographic analysis and materials testing, the focus will accordingly be on the second principle.

4.4.1 Time-of-Flight Technique

The technique is characterized by a wide wavelength spectrum (usually 0.5-5Å) of different short pulsed neutrons which provide the capturing of multitude diffraction peaks simultaneously. The time-of-flight (t) of each neutron is calculated using de Broglie (1. 2) and $v = L/t$:

$$t = \frac{\lambda m_n L}{h} \text{ [\mu s]}, \quad (1. 37)$$

L is the total path length corresponding to the source-to-detector distance. It is the sum of source-to-sample L_1 and sample-to-detector distance L_2 as demonstrated in the schematic layout of VULCAN in chapter 5.2.

The interplanar spacing is calculated by inserting (1. 37) into (1. 36):

$$d_{hkl} = \frac{h \cdot t_{hkl}}{2m_n(L_1 + L_2)\sin\theta_{hkl}} \text{ [\AA]}. \quad (1. 38)$$

Moreover, the elastic strain (see 4.6.1) of a material is defined by

$$\varepsilon = \frac{d_{hkl} - d_{hkl}^0}{d_{hkl}^0} = \frac{t_{hkl} - t_{hkl}^0}{t_{hkl}^0} = \frac{\Delta t_{hkl}}{t_{hkl}^0}. \quad (1. 39)$$

Here, d_{hkl}^0 is the lattice spacing of the stress-free material measured at t_{hkl}^0 (see subchapter 4.6.4) and depends on the t_{hkl} -location in the diffraction spectrum. If the sample is exposed to certain stress, the diffraction peak will shift in the time-axis due to the time difference in the numerator of (1. 39) [31]. This shift is used to determine the elastic strain.

4.4.2 Observation of Diffraction Profiles and Refinement

Nondestructive investigations of polycrystalline materials (metals) such as microstructure and texture analysis and elastic strain measurements can be obtained by recording certain neutron diffraction patterns (diffractograms). The experimental results are presented in an axis-system where the intensities are plotted over different Bragg reflections 2θ or scattering vectors Q . By knowing θ , the diffraction intensity pattern can also be plotted as a function of the lattice spacing, the time-of-flight t in the case of polychromatic neutron beams, or keV. A typical TOF diffraction pattern of a stainless steel is shown below.

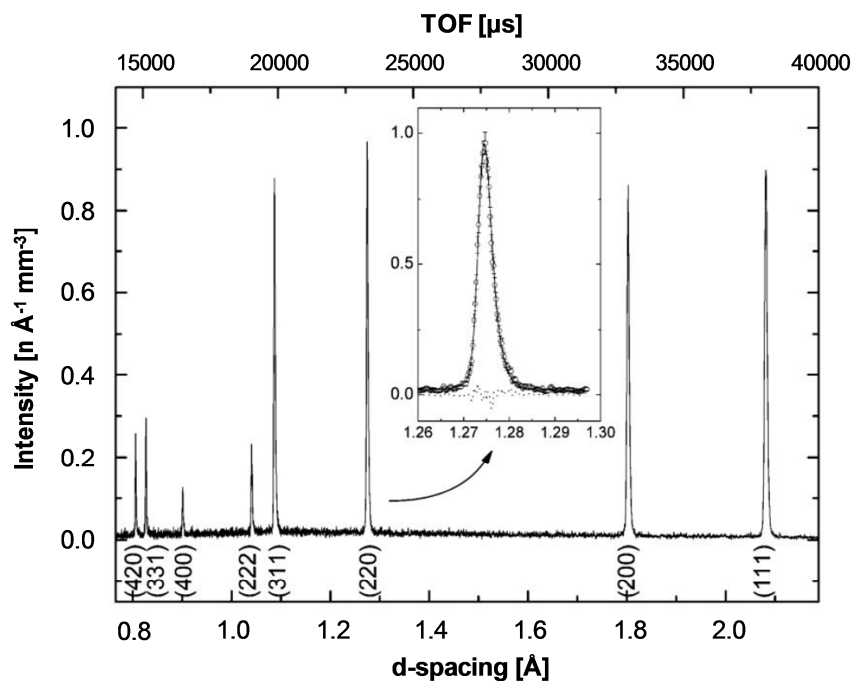


Figure 18: A typical TOF diffraction pattern of a stainless steel on the diffractometer ENGIN-X at ISIS, UK. Each peak corresponds to a lattice plane family (hkl) [32]

4.4.2.1 Information from Diffraction Spectra

Diffraction peaks within a generated pattern are characterized by the

- peak position,
- peak shape and
- peak intensity (Figure 19).

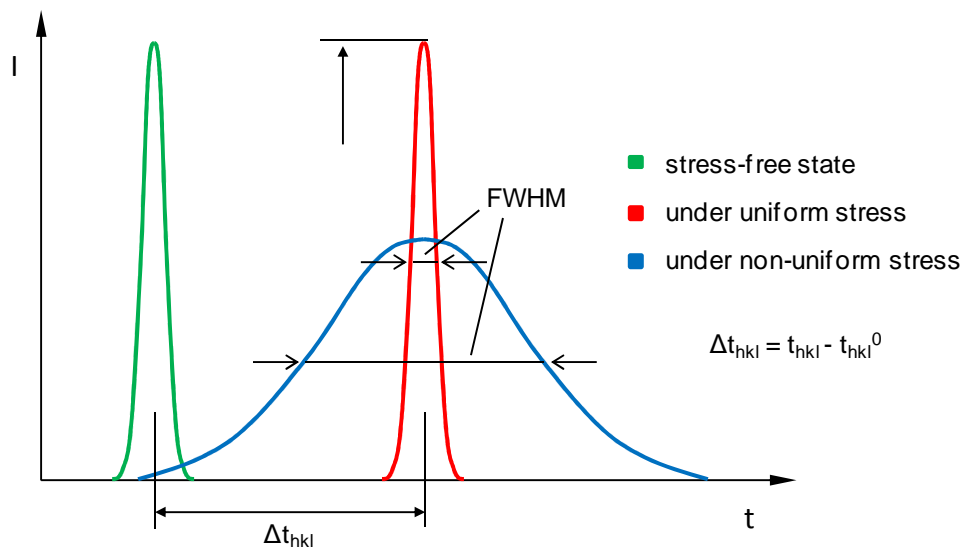


Figure 19: Characterization of a neutron diffraction peak [34]

The peak position characterizes the lattice spacing (d-spacing) of the crystal. A displacement in the peak position provides information about the stress condition and strongly depends on the elastic strain, current temperature and on the materials composition. The peak shape and the peak width reveal information about the materials microstructure such as defects, crystal size and shape, and microstrain. It depends on the convolution of the instrumental geometry, compositional heterogeneity and size of coherently diffracting domains, elastic strain heterogeneity and by local type III residual (micro)-stresses σ_R^{III} (see subchapter 4.6.3). The peak width, however, provides information of the strain fluctuation triggered by inhomogeneous stress fields (e.g. dislocations) and plastic deformations in the material. In practice it is often common to work with the full width at half-maximum (FWHM) as shown in Figure 19. Finally, the diffraction peak intensity of the observed profile characterizes the materials texture and the crystal structure [33, 34].

4.4.2.2 General Structure Analysis System

VULCAN uses the General Structure Analysis System (GSAS) – Software (Rietveld refinement) to fit the diffraction peak and to obtain the intensities. This is more like a standard program for crystallographic analysis of powder and single-crystal diffraction studies at time-of-flight instruments. GSAS

contains numerous specifications for selective fields of tasks. These include, among other things, thermal motion analysis, bond distance and angle computations, molecular geometry calculations as well as crystal structure, powder pattern and pole figure plotting.

Calculations of integrated intensities and profile functions of TOF data are based on [35] and are presented in the following section. The calculated intensity I_c at each point in the diffraction pattern is expressed by

$$I_c = I_b + S_h \sum_p S_{ph} I_{ph}. \quad (1.40)$$

I_b is the background scattering value, the other term is the sum over all phases p and histograms h where S_h is the histogram scale factor, S_{ph} is the phase scale factor within a histogram and I_{ph} complies with the contributed Bragg-intensity. The Bragg-intensity I_{ph} is proportional to the structure factor F_{ph} and is given as

$$I_{ph} = |F_{ph}|^2 H\Delta T K_{ph} \quad (1.41)$$

Here, $H\Delta T$ is the profile shape function and K_{ph} is the product of the reflection multiplicity M_p , the unit cell volume for the phase V_p and the correction factors extinction E_{ph} , absorption A_h , preferred orientation O_{ph} and the Lorentz-polarization L_p :

$$K_{ph} = \frac{E_{ph} A_h O_{ph} M_p L_p}{V_p} \quad (1.42)$$

Hence, by inserting (1.42) into (1.41) the Bragg-intensity equation finally changes to

$$I_{ph} = \frac{|F_{ph}|^2 H\Delta T E_{ph} A_h O_{ph} M_p L_p}{V_p} . \quad (1.43)$$

GSAS works with four different profile shape functions $H\Delta T$ which are basically Gaussian or Lorentzian. The functions are discussed in [35] in detail.

4.5 Small Angle Neutron Scattering

Small angle neutron scattering (SANS) is a very sophisticated and well-established diffraction technique to collect important data about the size, shape, structural arrangement and volume fraction of nanometer-sized particles and inhomogeneities (e.g. cavity/porosity) in a wide variety of materials. The SANS method has gained high interest for its application to diverse areas of technology, especially in the field of research in polymers and complex fluids, biology, chemistry and materials science. However, various testing methods such as scanning and transmission electron microscopy (SEM and TEM) or field ion microscopy (FIM) are usually confined to thin samples and are not capable to characterize precipitation kinetics in-situ. Therefore, SANS is a useful complementary approach to close certain gaps in the analysis of precipitation processes e.g. in thick samples [36].

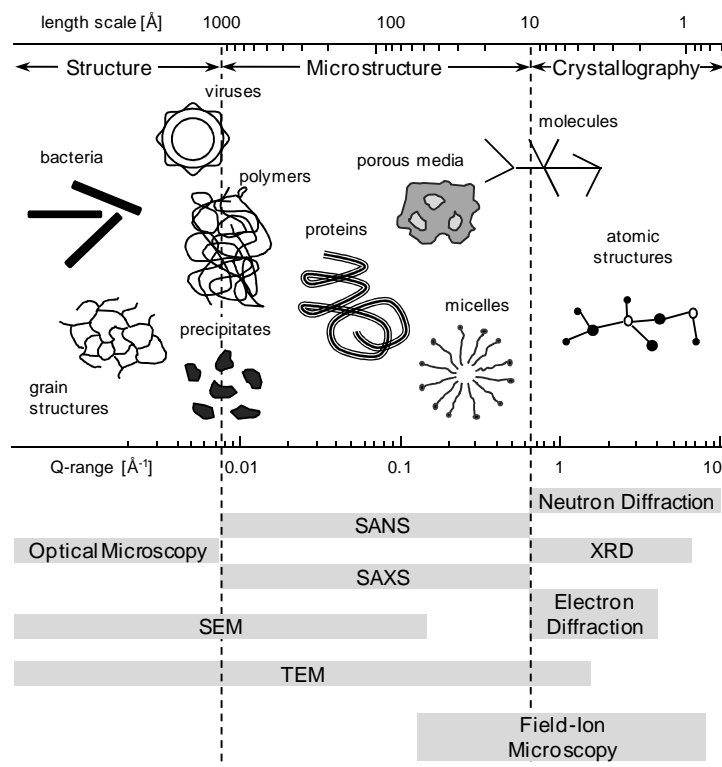


Figure 20: Comparison of different techniques to evaluate the structure of several materials. Small angle x-ray scattering (SAXS) facilitates the same capabilities like SANS, but it cannot be used to study bulk samples and hydrogen/deuterium containing materials. Sketch was compiled by the author and is based on [24, 36]

Apart from that, the method is remarkable for its better quantitative and statistical ascertainment of relevant data of nanoparticles [37, 38].

4.5.1 Principle

The technique is based upon the determination of the (macroscopic) differential scattering cross section $d\Sigma/d\Omega$ as a function of the scattering vector Q . The data is collected on a 2-dimensional neutron detector plate at very small scattering angles ($\theta < 4^\circ$). Curve shapes and progressions in the SANS pattern ($d\Sigma/d\Omega / I(Q)$ vs. Q) provide all information about the shape and size distributions within the sample. The following illustration shows the principle of SANS:

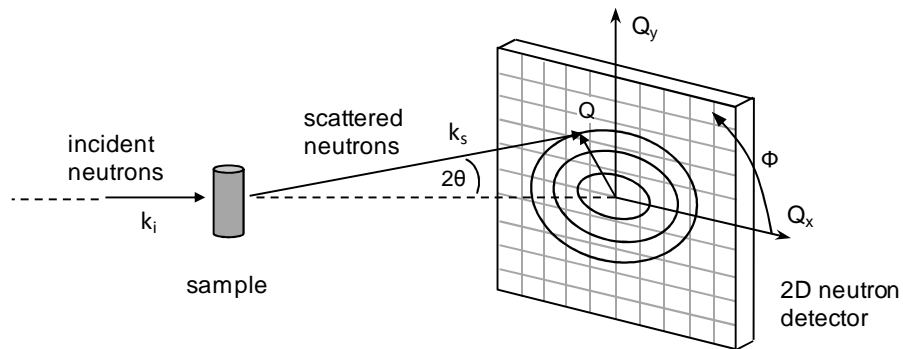


Figure 21: Principle of SANS

The SANS image obtained at the 2D position sensitive detector (Figure 22a) is converted into a 1-dimensional data set by plotting radially (azimuthal angle Φ) averaged diffraction spectra (Figure 22b) [24].

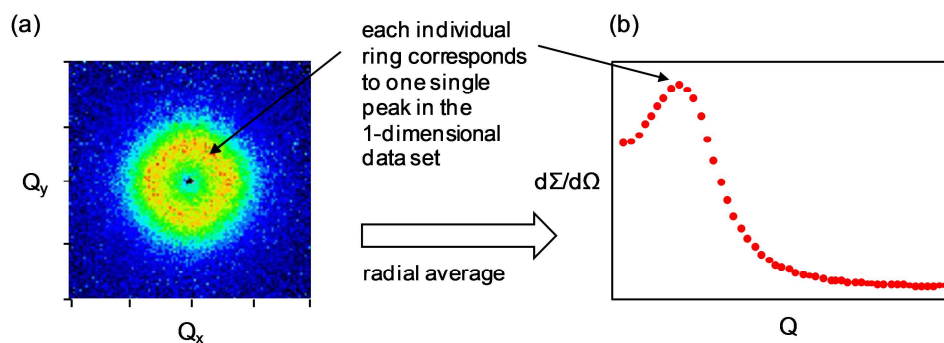


Figure 22: (a) An exemplary SANS image
(b) Radially averaged SANS pattern [24]

SANS instruments cover a typical Q -range from 0.001 to 0.5\AA^{-1} , while e.g. single-crystal or powder diffractometers and reflectometers operate at $Q > 0.5\text{\AA}^{-1}$ (VULCANs Q -range: $0.01 - 0.2\text{\AA}^{-1}$).

4.5.2 SANS Formalism

The macroscopic differential scattering cross section for each individual particle is given as

$$\frac{d\Sigma}{d\Omega}(\vec{Q}) = \frac{N}{V} \frac{d\sigma}{d\Omega}(\vec{Q}) [\text{cm}^{-1}], \quad (1. 44)$$

where N defines the number of atoms, V the sample volume and $d\sigma/d\Omega$ the differential scattering cross section as described in subchapter 4.3.1. By introducing the scattering length density ρ , which is defined as the sum of all scattering lengths b_i of the atoms within a defined volume V :

$$\rho = \frac{\sum_{i=1}^N b_i}{V} [\text{cm}^{-3}], \quad (1. 45)$$

the cross section can be written as

$$\frac{d\Sigma}{d\Omega}(\vec{Q}) = \frac{1}{V} \left| \int_V \rho(\vec{r}) e^{i\vec{Q}\vec{r}} d\vec{r} \right|^2, \quad (1. 46)$$

by substituting the sum with the integral over V . Appendix B includes the scattering lengths of all selected elements concerning 9-12% martensitic Cr-steels. In two-phase systems (e.g. particles or precipitates within the matrix) equation (1. 46) changes to the expression:

$$\frac{d\Sigma}{d\Omega}(\vec{Q}) = \frac{1}{V} (\rho_1 - \rho_2)^2 \left| \int_{V_1} e^{i\vec{Q}\vec{r}_1} d\vec{r}_1 \right|^2. \quad (1. 47)$$

The squared difference in the bracket ($= \Delta\rho^2$) is thus the difference in neutron scattering length densities between the particle and background ($=$ matrix) and is referred to as the neutron contrast factor. The previous basic formulas are valid for simplified materials with randomly distributed non-interacting particles

(= dilute systems). However, considering condensed matters with an interaction of particles, the macroscopic differential scattering cross section can be expressed by

$$\frac{d\Sigma}{d\Omega}(\vec{Q}) = n_P \Delta\rho^2 V_P^2 P(\vec{Q}) S(\vec{Q}), \quad (1.48)$$

where n_P is the number density of the particles/precipitates (number of particles N_P divided by the sample volume V : $n_P = N_P/V$), V_P corresponds to the particle volume (e.g. sphere: $V = 4\pi R^3/3$) and $P(Q)$ is the so-called form factor. The dimensionless $P(Q)$ describes the effects of interference of scattered neutrons from different sections of the same component and is given by

$$P(\vec{Q}) = |F(\vec{Q})|^2, \quad (1.49)$$

with $F(Q)$ as the form factor scattering amplitude which provides information about the shape and size of the particles. It is also important to note that the measured intensity in crystallography is (as often used in practice and introduced in subchapter 4.4.2.2) proportional to $d\Sigma/d\sigma$ and to the structure factor:

$$I_{hkl} \propto |F_{hkl}|^2. \quad (1.50)$$

The equation for the form factor of spherical particles with the radius R for instance, is

$$P(\vec{Q}) = \left(\frac{3[\sin(QR) - QR\cos(QR)]}{(QR)^3} \right)^2, \quad (1.51)$$

as assumed in the recently by Zickler et al. [38] conducted SANS study for the intermetallic γ' phase of a superalloy. Furthermore, the variable $S(Q)$ in (1.48) designates the structure factor, representing interparticle interferences of neutrons and is generally given as

$$S(\vec{Q}) = \frac{1}{N_P} \left\langle \sum_{i,j=1}^{N_P} e^{i\vec{Q}(\vec{R}_i - \vec{R}_j)} \right\rangle. \quad (1.52)$$

For the sake of completeness, it is necessary to use the Guinier and Porod approximations below and above the accessible Q-region as will be briefly discussed in the following.

4.5.2.1 Guinier and Porod Regime

In the low-Q region, the form factor and the scattering intensity, respectively, are functions of the radius of gyration R_g and can be calculated by using Guinier's law:

$$P(\vec{Q}) = |F(\vec{Q})|^2 = e^{-\frac{(QR_g)^2}{3}} \quad (1.53)$$

and

$$I(Q) = I_0 e^{-\frac{(QR_g)^2}{3}} \quad (1.54)$$

The radii of gyration for some chosen particles are listed in the Appendix C. In the high-Q region on the other hand, the SANS data can be obtained by using the approximation of Porod:

$$I(Q) \propto Q^{-4}. \quad (1.55)$$

4.5.3 Practical Application

Recently, this elastic scattering technique proved to be absolutely suitable for the study of particle size distributions and precipitation kinetics like e.g. in high-speed steels [37] or in nickel-iron-chromium-based alloys (superalloys) [38]. Since the materials properties greatly depend on different heat treatment processes (e.g. annealing, aging, tempering, quenching) and precipitation, it is of crucial importance to control the factors such as time and temperature in order to determine the particles size and distribution which may influence, inter alia, the materials strength and ductility.

It is also very important to make a distinction between magnetic (e.g. ferritic/martensitic 9-12%Cr steels) and non-magnetic materials (austenitic steels). In the case of magnetic materials, one has to consider an additional term for the formula for the macroscopic differential scattering cross section [39]:

$$\frac{d\Sigma}{d\Omega}(\vec{Q}) = \left(\frac{d\Sigma}{d\Omega}(\vec{Q})\right)_{\text{nucl.}} + \left(\frac{d\Sigma}{d\Omega}(\vec{Q})\right)_{\text{magn.}} \sin^2 \phi. \quad (1.56)$$

Radii, number densities, volume fractions as well as the FWHM of the particles at different temperatures during the heat treatment process as a function of time can be presented by means of the obtained SANS data. Leitner et al. [37], for instance, showed the different particle number density and volume fraction behaviors of medium-sized ($10\text{nm} > R > 1\text{nm}$) and small ($R < 1\text{nm}$) particles of a high-speed steel during tempering at 590°C . Zickler et al. [38] investigated the phase precipitation kinetics of the Ni-Fe-Cr-based alloy during in-situ aging treatments. The observed results of the differential cross section as a function of the scattering vector at different aging times (as-quenched up to 6.980 seconds) at a chosen temperature are demonstrated below.

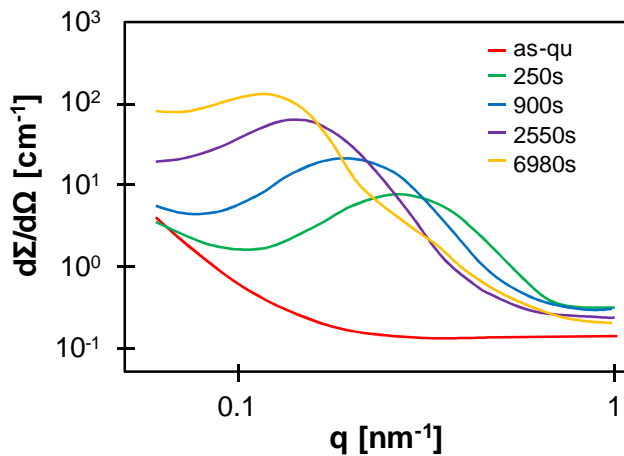


Figure 23: SANS pattern obtained at 1148K. Based on reference [38]

Furthermore, the γ' phase precipitate has been examined more closely by plotting the radius R , number density N , volume fraction f and FWHM over the aging time. The following figure illustrates the first 3 mentioned experimental results:

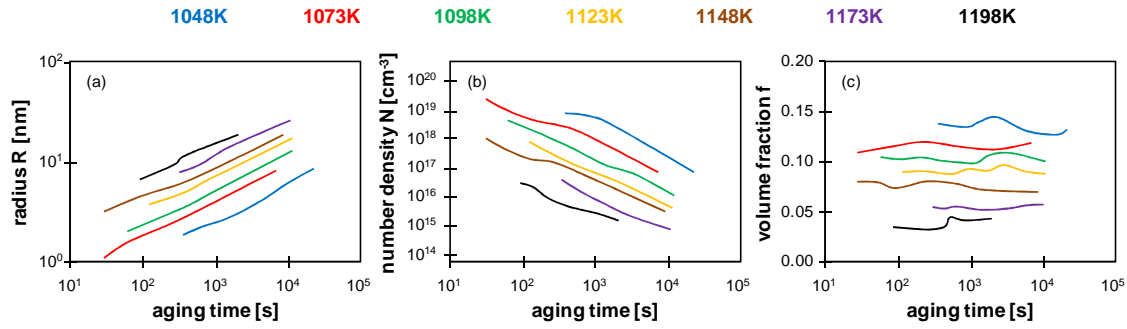


Figure 24: (a) Radius R is larger at higher temperatures and increases with increasing aging time (t) for each temperature level. (b) Number density N is smaller at lower temperatures and decreases with t . (c) Volume fraction f is smaller for high-temperature levels and stays nearly constant with increasing t . Charts are based on [38]

The full width at half maximum is smaller for lower temperature levels and slightly increases with increasing aging time [38].

4.6 Strain and Stress Analysis

Weak points like weldings may affect the performance of engineering components and can lead to immense economic and human losses. Residual and internal stresses arise from inhomogeneously distributed deformations in the material induced by various manufacturing processes like casting, machining, heat and surface treatments, hot and cold working processes and coatings [40, 41]. These influence the materials properties (e.g. strength, durability, wear and corrosion resistance) and may be one of the potential reasons for unanticipated defects like (intergranular) crackings which can cause premature failures and unexpected breakdowns, respectively.

4.6.1 Definition of Strain and Stress

The mechanical definition of stress is given by the second-order stress tensor

$$\sigma_{ij} = \frac{\partial F_i}{\partial A_j}, \quad (1.57)$$

where the direction of an applied force (= load) on a body is perpendicular to the plane A.

In a standardized reference system the stress tensor of a volume element can be expressed as

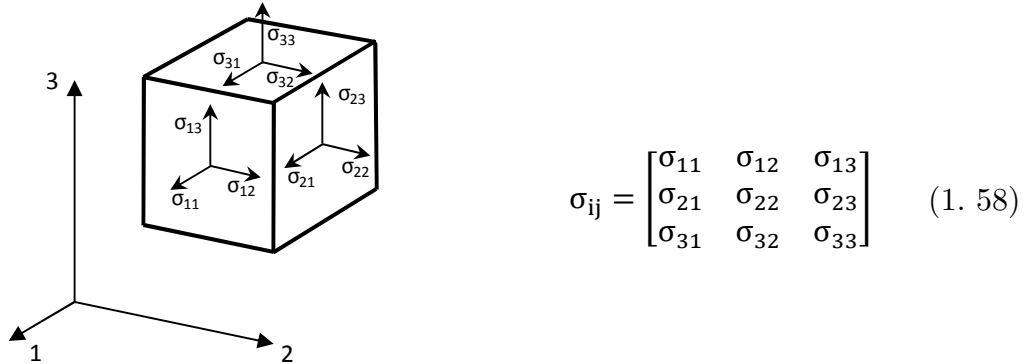


Figure 25: Stress components of a cubic volume element

The engineering stress (F is again the applied force and A_0 the cross-sectional plane) can be principally written as

$$\sigma = \frac{F}{A_0}. \quad (1.59)$$

Furthermore, the definition of strain of an infinitesimal material element is given as

$$\varepsilon_{ij} = \frac{1}{2} \left[\frac{\partial u_i}{\partial x_j} + \frac{\partial u_j}{\partial x_i} \right], \quad (1.60)$$

also known as the second-order strain tensor. The terms in square brackets are the displacement gradients. Strain in a referential system 1, 2, 3 is

$$\varepsilon_{ij} = \begin{bmatrix} \varepsilon_{11} & \varepsilon_{12} & \varepsilon_{13} \\ \varepsilon_{21} & \varepsilon_{22} & \varepsilon_{23} \\ \varepsilon_{31} & \varepsilon_{32} & \varepsilon_{33} \end{bmatrix}. \quad (1.61)$$

The engineering strain is defined by

$$\epsilon = \frac{l - l_0}{l_0}, \quad (1.62)$$

with l_0 as the original length and l the length after subjected to force F or stress σ (see strain-stress curve and tensile test).

The engineering stress can also be deduced after having obtained the strain components. For homogeneous and elastic materials the strain ε is linearly proportional to the stress σ and to the modulus of elasticity or Young's modulus E . For the macroscopic case and elastic response, this can be described via Hooke's law as

$$\sigma = E \cdot \varepsilon. \quad (1.63)$$

For three-dimensional microscopic problems the generalized Hooke's law is expressed as

$$\sigma_{ij} = C_{ijkl} \varepsilon_{kl} \quad (1.64)$$

and
$$\varepsilon_{ij} = S_{ijkl} \sigma_{kl}. \quad (1.65)$$

C_{ijkl} and S_{ijkl} are the fourth-order elastic stiffness (single-crystal elastic-) and compliance tensors, each with 81 components directed to kl [40].

4.6.2 Polycrystalline Materials

Considering the isotropy and the symmetry properties of the crystal lattice in the case of cubic polycrystalline materials (e.g. steels), the components of (1.64) and (1.65) get significantly reduced. Therefore the transformation of strain to stress is derived by the following formula:

$$\sigma_{ij} = \frac{E_{hkl}}{1 + \nu_{hkl}} \varepsilon_{ij} - \frac{\nu_{hkl} E_{hkl}}{(1 + \nu_{hkl})(1 - 2\nu_{hkl})} \delta \varepsilon_{kk}, \quad (1.66)$$

where E_{hkl} is the plane-specific Young's modulus, ν_{hkl} the Poisson's ratio of the cubic polycrystalline crystal and δ the Kronecker delta-function [31, 40]. Therefore, it's sufficient to measure only three strain components. The elastic constants E_{hkl} and ν_{hkl} can be determined with the approximation of Voigt and Reuss or with the self-consistent model of Kroner as described in [40].

4.6.3 Classification of Residual Stresses

Residual stresses can be classified in relation to the dimension into three types:

- type I residual (macro)-stresses σ_R^I around large crystal areas,
- type II residual (micro)-stresses σ_R^{II} at small crystal areas and
- type III residual (micro)-stresses σ_R^{III} within interatomic spacings [40].

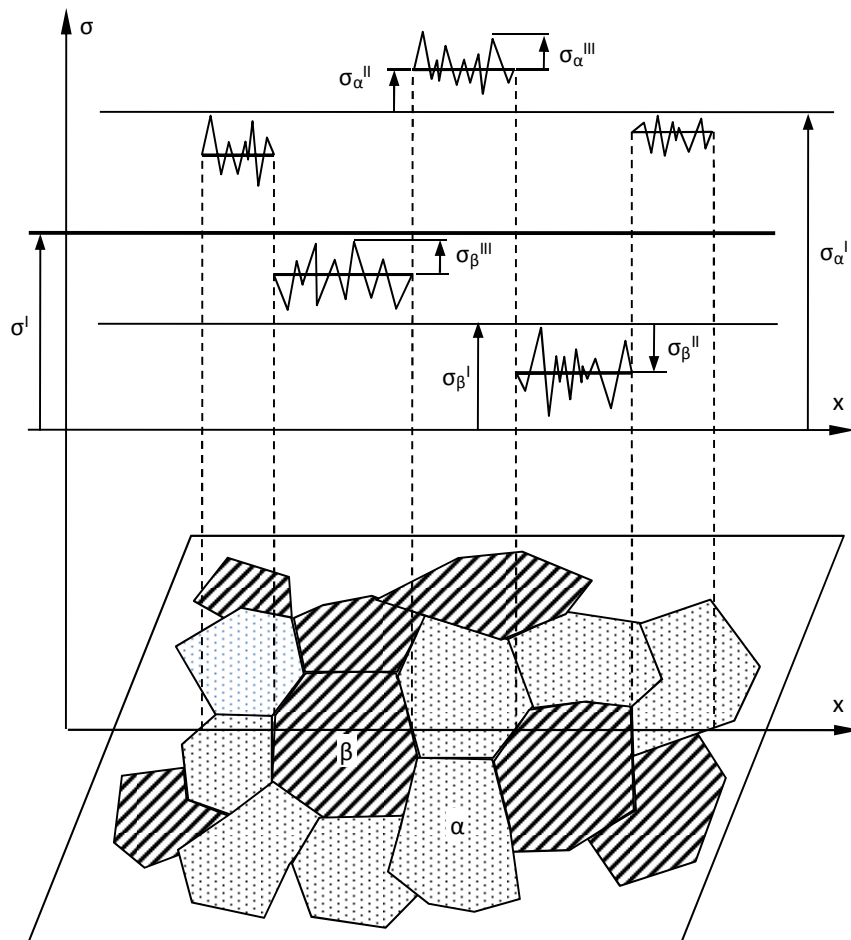


Figure 26: Superposition of the three orders of stresses in a two-phase (α and β) material. Compiled by the author and based on [40]

Type I stress corresponds to an average constant value over a specific grain-area in a crystal and meets more or less the macroscopic stress of the whole specimen. Intergranular type II stresses differ due to the elastic behavior and anisotropy and are constant over single grains. The latter shows various stress values within such grains, dislocations or grain boundaries (Figure 26).

4.6.4 Determination of the Reference Lattice Spacing d_{hkl}^0

As seen in equation (1. 39) the lattice spacing d_{hkl}^0 of the stress-free material is needed to calculate the shift in the time-axis and subsequently the elastic strain ε and the stress σ . The value of d_{hkl}^0 should be as accurate as possible to provide exact data for the operator. However, the stressless lattice spacing can vary greatly within very small dimensions and is often difficult to assess. This is probably caused by fabrication or machining processes, for instance due to thermo-mechanical treatments. There are various approaches to measure d_{hkl}^0 of the specimens. Stress-free powder measurements of the same material may be one but not always a precise variant to determine the lattice spacing. Another approach would be by measuring d_{hkl}^0 at another region, e.g. around the far edge of the component. Alternatively, one may cut an identical specimen (companion) into small parts and measure d_{hkl}^0 . If none of these approaches can be applied, then the operator may carry on with estimated stress-free lattice spacing data and report the error [42].

4.6.5 Volumetric Strain Mapping

Sophisticated neutron diffraction instruments are able to facilitate spatial mappings around sample areas such as welds. While uni-axial stress evaluations only need one measurement direction, multi-axial measurements require a volumetric system to image three-dimensional models. A simplified representation of strain mapping measurements is demonstrated below [34].

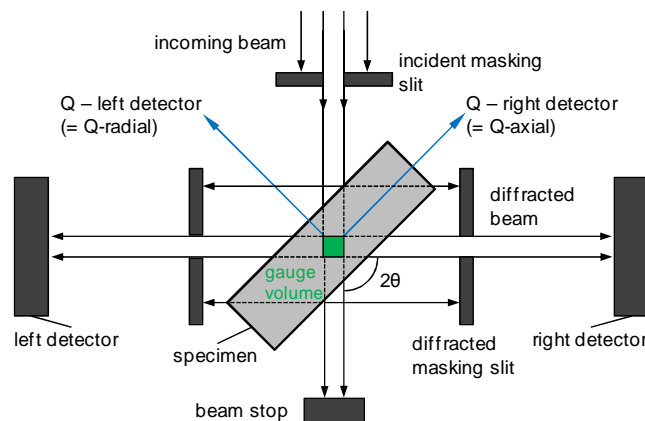


Figure 27: Principle of strain mapping

The sides with defined widths of the body along the incoming beam direction are defined by the incident and diffracted masking slits as shown above. Both detectors are arranged at an angle of $\pm 90^\circ$ to measure two perpendicular strain constituents simultaneously and to regulate more or less a cubic body. Other gauge volume shapes are also possible by varying the detector angle. Diffractometers like VULCAN have adjustable detectors with an angular coverage of 60° to 150° . A 3D-scanning can be obtained by moving the part through the gauge volume. VULCAN, for instance, is equipped with state-of-the-art technology and enables a volumetric strain mapping with a resolution of $1 \times 1 \times 1 \text{ mm}^3$ sampling volume of iron within 1min [34, 43]. It is about 30 times faster than other third-generation neutron diffractometers like the TOF spectrometer for materials research at temperature and stress (SMARTS) at the Lujan Center in New Mexico [44]. Diffracted masking slits are designed as radial collimators which usually collimate the scattered neutrons and constitute the image size on the detectors. Figure 28 provides a detailed three-dimensional view of the gauge volume with $\delta V = \Delta x \cdot \Delta y \cdot \Delta z$ defined by the apertures.

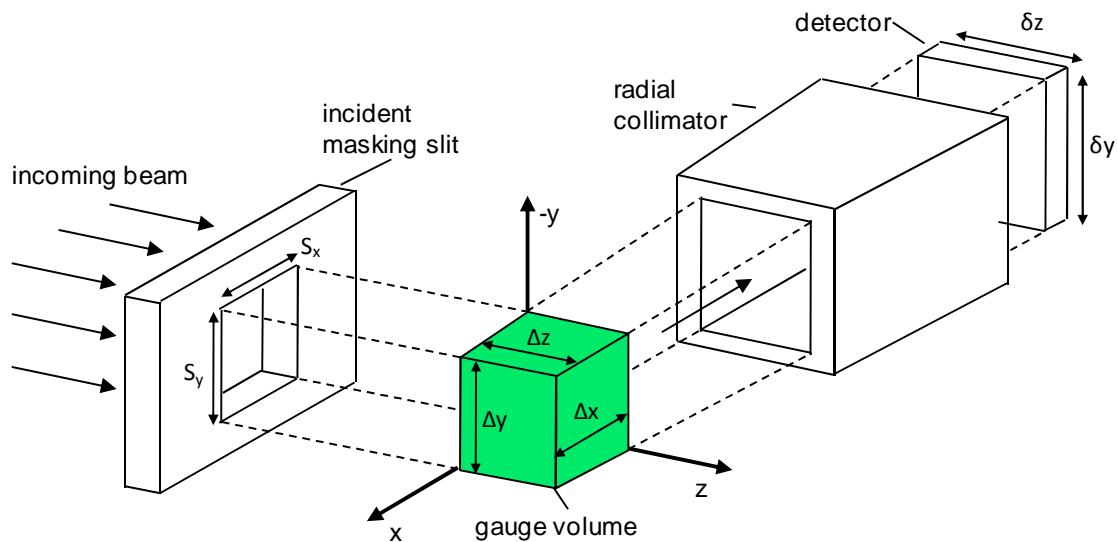


Figure 28: Illustration of the instrumental gauge volume. Based on [32]

This formation enables the determination of the strain component along the scattering vector Q , the resulting vector of the incident and scattered neutron beam.

4.6.6 Residual Stress Measurement by Neutron Diffraction in Welds

Information on residual stresses and the principle of strain mapping was addressed in the preceding sections. This subchapter is specifically dealing with the application of neutron diffraction for residual stress analysis in welded components.

4.6.6.1 Origin of Residual Stresses in Welds

Types of residual stresses in materials were already discussed in [4.6.3]. Residual micro- and macrostresses particularly in welds, both tensile and compressive, arise from inhomogeneous ongoing deformations. These result from volume changes caused by thermal expansion (thermal stresses), chemical and microstructural transformations (transformation residual stresses), changes in shape due to plastic deformations and connectivity changes due to macrodislocations. Thermal stresses during welding processes result from different temperature distributions in the material. The colder surrounding material hinders the expansion of the hotter metal of the welding zone leading consequently to forces and stresses, respectively. Higher temperatures decrease the yield strength of the material. This means that it makes it easier for thermal stresses to exceed this point and deform the welding zone plastically. By cooling down, this area is shrinking and is thus exposed to thermal tensions. Transformation residual stresses are generated due to e.g. austenite (γ) to ferrite (α) phase transformations in steels. This transformation induces a volume expansion during cooling and causes compressive residual stresses in the welding zone and tensile stresses in the surrounding material [41].

All these complicated procedures creating such residual stresses may influence fractures like Type IV crackings during service.

4.6.6.2 Practical Example – Bead-on-Plate Weld Specimen

Recently, many researchers and scientists already applied the neutron diffraction technique to observe strain and stress distributions in different components. Pratihari et al. [45] for instance performed a complete measurement in a 316L stainless steel bead-on-plate weld specimen^b using the TOF ENGIN-X diffractometer at the ISIS neutron source, UK. The two detectors of the instrument were arranged at a common angle of $2\theta = \pm 90^\circ$ to measure the strains simultaneously as described in (4.6.5). A schematic view of the welded specimen and the origin of the coordinate system are shown in the figure below.

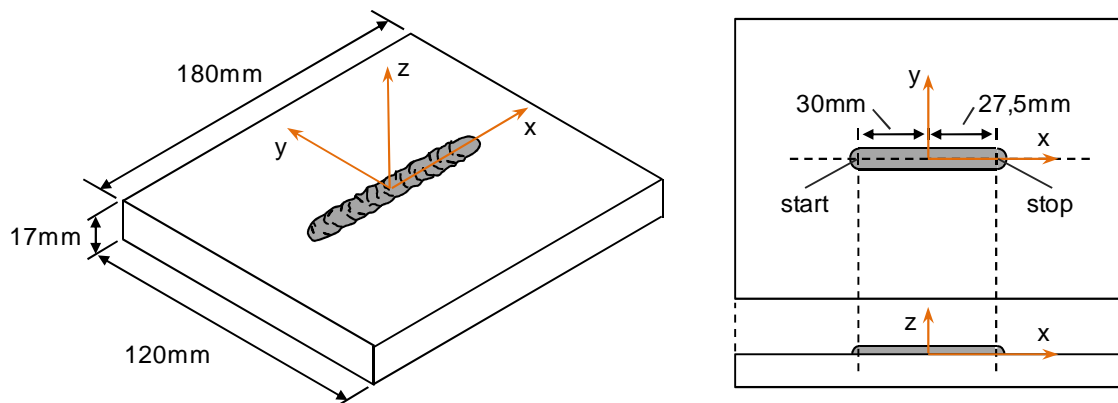


Figure 29: Bead-on-plate weld specimen [45]

The measurements were carried out along the longitudinal LD (along the welded beam towards the x-axis), transverse TD to the weld (along the y-axis) and along the normal direction ND perpendicular to the x-y plate surface. The gauge volume of the spatial strain mapping was defined with a resolution of $2 \times 2 \times 2 \text{mm}^3$. GSAS was utilized to observe the diffraction patterns and to fit the peaks in order to determine the elastic strain values and further the stresses by using Hooke's law. The strainless reference lattice spacing d_{hkl}^0 was measured from the corner of the part. Furthermore, the strain was measured at a depth of 2mm to avoid a potential influence of the weld filler material on d_{hkl}^0 .

^b using automated Tungsten Inert Gas (TIG) Welding

The experimental results have demonstrated that around the weld bead there were high tensile residual stresses along the longitudinal and transverse direction, even an increase of the tension in the transverse direction. Compressive residual strains were measured along the normal direction.

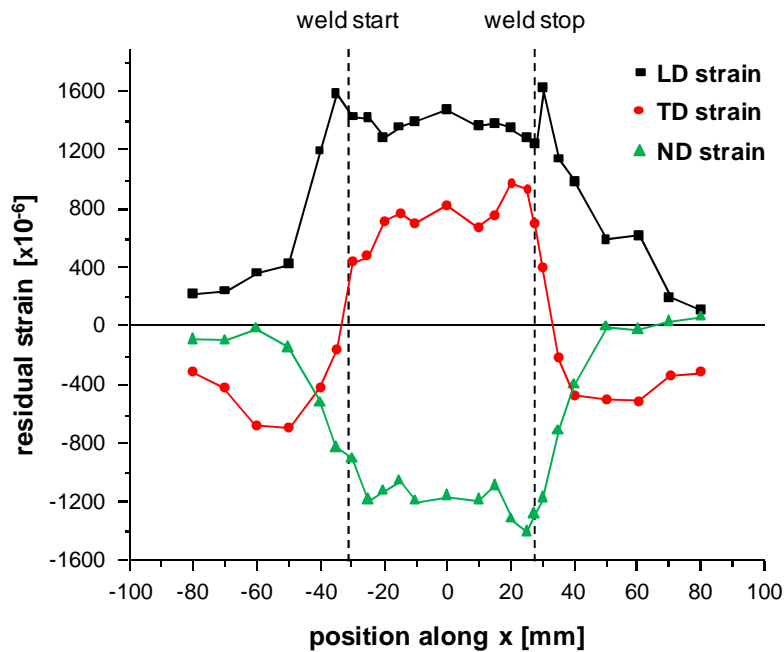


Figure 30: Residual strain distribution along x at z = -2mm [45]

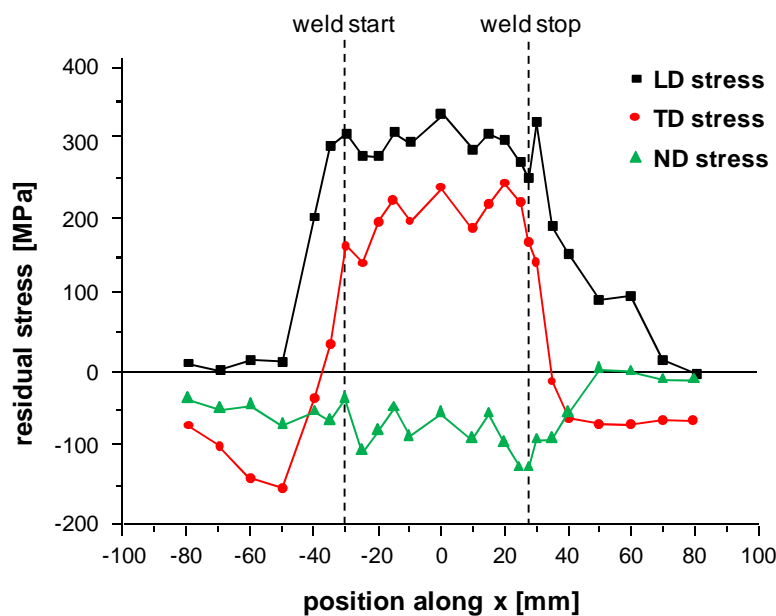


Figure 31: Residual stress distribution along x at z = -2mm [45]

Apart from that, a through-thickness transverse residual strain profile showed a high residual strain concentration shortly before the weld-stop at $x = 27.5\text{mm}$:

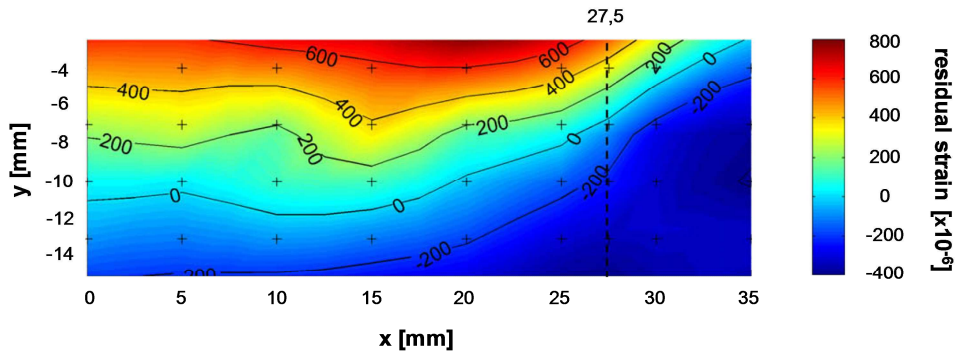


Figure 32: Through-thickness transverse residual strain profile [45]

All the residual strain and stress profiles along and transverse to the welding direction can be found in [45].

4.7 Texture Analysis

Polychromatic neutrons at pulsed spallation sources are being more and more frequently used for texture analysis in materials science and engineering. Neutrons differ from other diffraction techniques like XRD by virtue of the fact that they undergo very weak interactions with matter. This provides on the one hand a high penetration capability of neutrons which allow the study of bulk components, and on the other hand low absorptions for in-situ investigations of the changes in texture, e.g. during phase transformations.

4.7.1 Basics

The texture can be defined as the distribution of preferred crystallographic orientation in polycrystalline materials and affects the materials mechanical and physical properties such as yield strength, magnetic properties, electrical conductivity and permeability. Textures evolve during growth (e.g. stress and magnetic fields or temperature gradient), during plastic deformation (e.g. slip), recrystallization or during phase transformations. Textures may influence the deformation characteristics of metals e.g. during deep drawing processes producing inhomogeneous edges (earing effect, see [46]). Texture strongly

depends on different factors like various mechanical treatments or aging and can change over time. This demands the fundamental understanding of texture itself as well as advanced testing techniques to observe changes in texture when performing in-situ studies [46, 47].

4.7.2 Presentation of Orientations

A quantitative texture analysis requires both crystal and orthogonal sample (specimen) coordinate system relations. The sample coordinate system (a, b, c) is mostly set according to the forming process such as rolling (a = RD – rolling direction, b = TD – transverse direction and c = ND – normal direction, perpendicular to the RD – TD plane). Further, the crystal coordinate system (x, y, z) is usually defined by using the Miller indices (x = [100], y = [010] and z = [001]). The figure below shows the orientation of a unit cube within a sample plate:

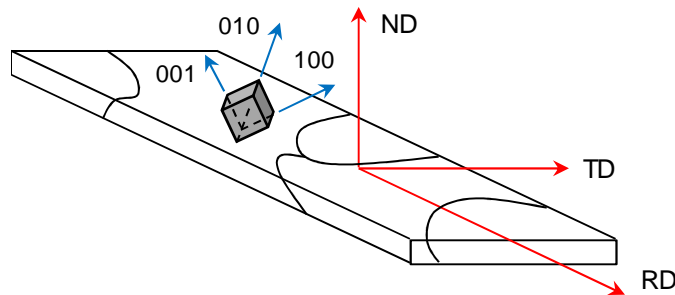


Figure 33: Sample and crystal coordinate system

4.7.3 Euler Angles

The sample coordinate system has to be transformed into the crystal system by introducing the rotation g and the three Euler angles in order to define the crystal orientation of each grain. The superposition can be either done with the Roe/Matthies convention for Euler angles (α , β , γ) or by means of the most widely-used Bunge convention (g ($\varphi_1 = \alpha + \pi/2$, $\Phi = \beta$, $\varphi_2 = \gamma - \pi/2$)) (see Wenk et al. [47]). φ_1 is the first rotation around the z-axis generating the new x' and y'-axis (pink). Φ is the rotation around x' bringing the y'-axis to y''

and z to z' (green). Finally, the rotation φ_2 around z' creates the final orientation of the crystal coordinate system (blue) with x'' ($=100$), y'' ($=010$) and z' ($=001$). The transformation of the sample (red) onto the crystal coordinate system (blue) is demonstrated as follows:

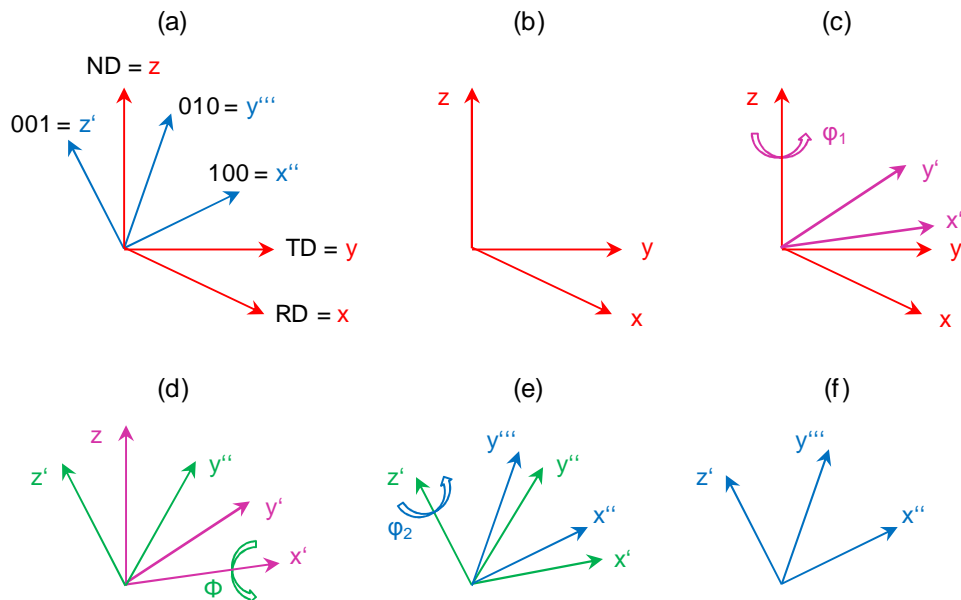


Figure 34: Definition of the Euler angles(a) Superposition of the sample coordinate system (SCS, red) and the crystal coordinate system (CCS, blue). (b) Initial position of SCS. (c) First Euler rotation φ_1 around the z -axis. (d) Rotation Φ around the new x' -axis. (e) Third and last rotation φ_2 around the z' -axis. (f) Final CCS

This is of fundamental importance for the orientation distribution functions as described in subchapter 4.7.6.

4.7.4 Pole Figures

Graphical representations of preferred crystallographic orientations can be realized through pole figure measurements. These are two-dimensional projections (often stereographic) and represent the orientation distribution of crystals with respect to the specimen axis system [46, 47]. Imagine a grain's atomic and crystal structure of a metallic sample: By moving a unit cell of the crystal in its initial orientation to a sphere with the same defined sample coordinate system (RD , TD and ND , respectively), the normals of the lattice

planes of the crystal unit cell ($[100]$, $[010]$, $[001]$) intersect the surface of the sphere. By connecting the intersection points with the “south pole” P, the connection lines intersect the projection plane p. These spots on p are presenting the pole figures. The figure below demonstrates a simplified presentation of the orientation of a unit cube by means of stereographically projected pole figures.

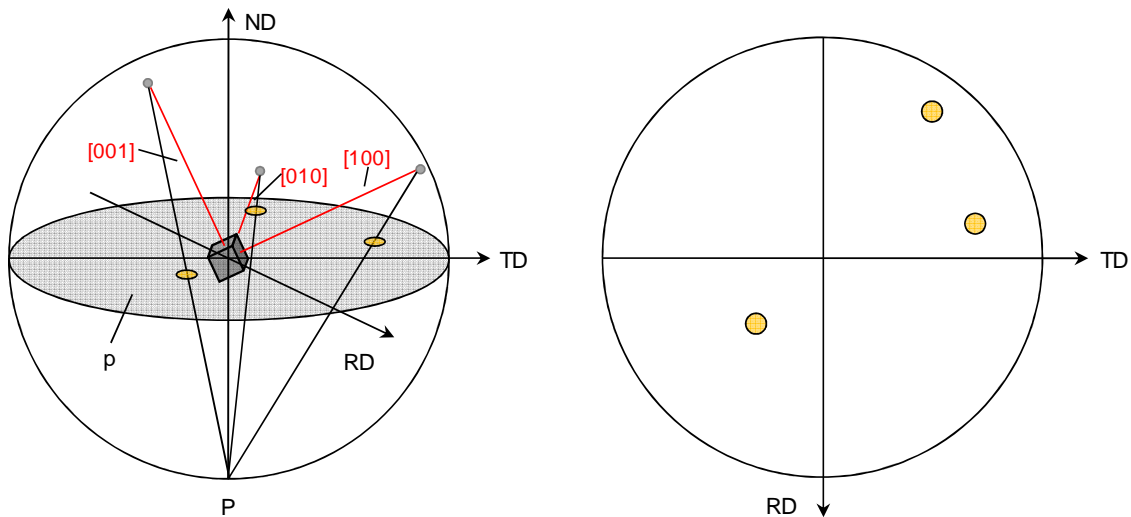


Figure 35: Stereographic projection of a unit cube (single crystal)

A very good step by step description of a stereographic projection construction for a single grain of an fcc crystal structure in a cold rolled aluminum plate gives [48].

4.7.5 Inverse Pole Figures

Inverse pole figures display the orientation distribution of a sample direction (usually parallel to the ND-plane) with respect to the crystal coordinate system. These are more adequate for symmetrical crystals and are typically displayed as triangular parts of the “standard projection” because of crystal symmetries e.g. in cubic systems. Here, selected orientations of a single crystal are projected onto the equatorial plane. Following figure shows the specific oriented unit crystal and the hatched segment $[001]$ $[011]$ $[111]$ triangle segment of the standard projection [49].

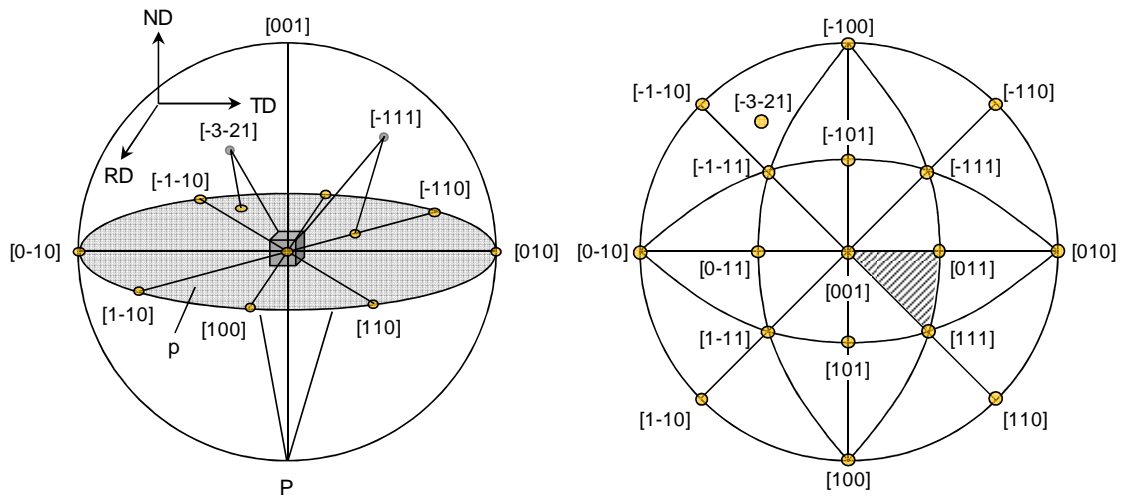


Figure 36: Inverse pole figure construction

4.7.6 Orientation Distribution Function

Three-dimensional textures in polycrystalline materials can be described and quantified by an orientation distribution function (ODF) which can be calculated from a few measured pole figures after background intensity corrections. Conversely, this means that the pole figures are the two-dimensional projections of the 3D ODF. This mathematical function describes the probability of finding crystal orientations with respect to the sample coordinate system [47]. The ODFs are plotted as 2D sections ($\varphi_1 - \Phi$ plane) in the three-dimensional Euler space (cube with axis φ_1 , Φ and φ_2). The angle φ_2 (or γ in the case of the Roe/Matthies convention) is presented as each orientation distribution section (see case study in subchapter 4.7.7).

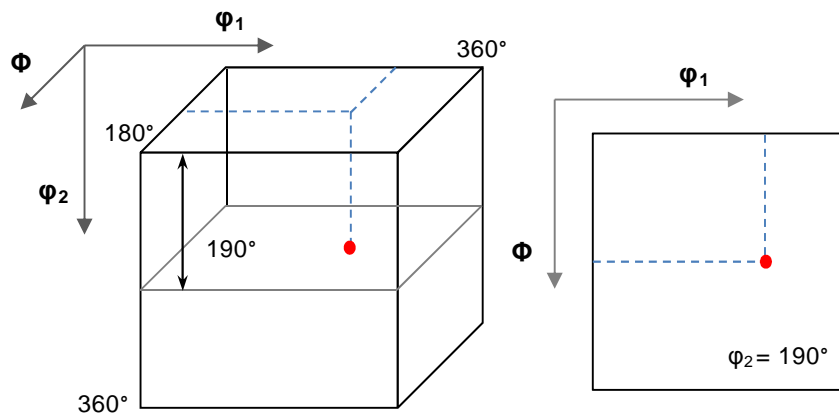


Figure 37: Euler space

The previous image demonstrates the Euler space for no sample geometry (asymmetric unit). Dependent on the crystal symmetry of the sample to be investigated the range of the Euler angles may get reduced (e.g. $\varphi_1 = \Phi = \varphi_2 = 90^\circ$ for cubic crystal and orthonormal sample symmetries) [50].

The ODF can be obtained with the widely used WIMV (Williams-Imhof-Matthies-Vinel) algorithm or the extended WIMV (E-WIMV) with improved refinement properties, with the vector, or with the maximum entropy method. These work in direct space based upon algorithms of tomography. Another option would be the harmonic method which works in Fourier space. Here, the pole figures are generated from the spherical harmonic coefficients, e.g. via Rietveld refinement of diffraction data. Texture analysis programs which calculate the ODF from pole figures are for instance BEARTEX, LaboTex, MulTex, popLA and TexTools [47].

4.7.7 Texture Analysis with TOF Neutron Diffractometers

Texture information or orientation distribution can also be taken from TOF neutron diffraction profiles where the diffraction peak intensities, which are directly related to the ODF values, characterize the materials texture. This can be either done with harmonic methods in the Rietveld package, which is implemented in GSAS (e.g. POLFPLOT – pole figure plotting program, [35]), MAUD (Material Analysis Using Diffraction) or with discrete methods in MAUD (VULCAN primarily uses the software package MAUD for texture analysis). Discrete methods provide quantitative texture representations whereas harmonic techniques are used for qualitative data. Rietveld with GSAS is characterized by fast analytical computations, but is limited to the harmonic method and can only accept a maximum of 99 diffraction spectra. MAUD on the other hand is slower due to numerical calculations, but is advantageous for the use of algorithms both in direct (e.g. E-WIMV) and in Fourier space (MAUD and GSAS harmonic method) to derive the ODFs [51].

Current sophisticated TOF instruments like VULCAN or the HIPPO (High-Pressure-Preferred Orientation) diffractometer at the pulsed spallation neutron source LANSCE in New Mexico enable rapid and efficient texture measurements.

Matthies et al [51], for instance, performed a quantitative texture examination of an ECAP (equal-channel angular-pressed) aluminium sample using HIPPO where the observed results showed strong orientation distributions of the sample. The multi-detector system, the schematic view of the instrument and its characteristics can be seen in [51]. The measurement was carried out at three detector banks ($2\theta = 40^\circ, 90^\circ$ and 140°) where a rotation around a single axis was sufficient for texture analysis. The diffraction spectra within one bank revealed different peak intensities at different rotation positions illustrating a strong textured material. The following figure shows the recorded spectra within $0.8 - 2.6\text{\AA}$ in four rotations ($0^\circ, 45^\circ, 67.5^\circ$ and 90°) at the 40° detector bank:

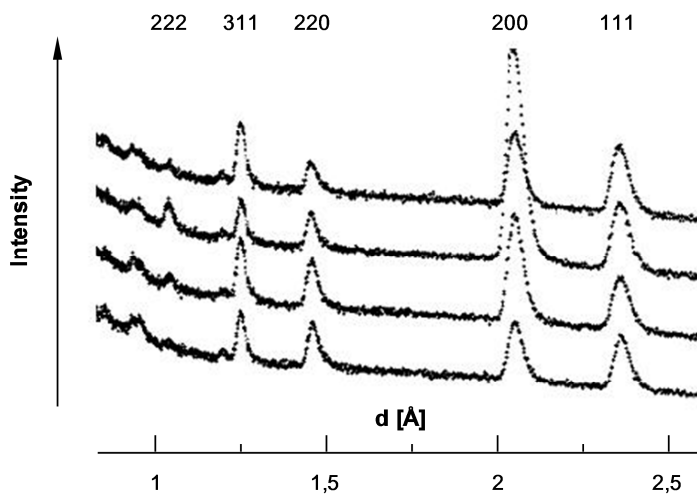


Figure 38: TOF neutron diffraction spectra of ECAP aluminium recorded at HIPPO on a 40° detector bank in 4 rotation positions. Peak intensity deviations indicate a textured material [51]

The texture data for the aluminium sample was analyzed with the four software packages as mentioned in the first paragraph of this subchapter. The ODFs were represented by using the Roe/Matthies convention as described in (4.7.3):

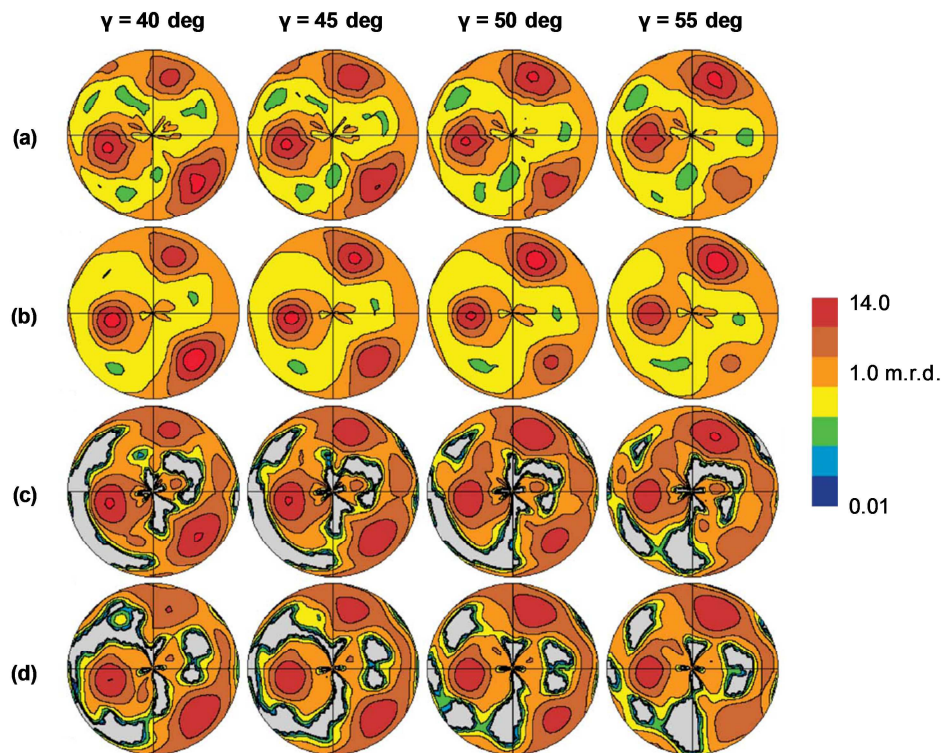


Figure 39: Orientation distribution functions of ECAP Aluminium determined at the HIPPO diffractometer. The gamma values correspond to the third Euler angle. (a) GULUWIMV^c (universal WIMV-related program). (b) MAUD E-WIMV. (c) MAUD harmonic method, $L = 12$. (d) GSAS harmonic method, $L = 12$. m.r.d. stand for “multiples of random distribution” which describe the pole intensity values. L stands for the logarithmic scale [51]

^c GULU: G for remaining ghost correction, U for universal, L for hole (German for “Loch”) and finally U for incomplete (German for “unvollstaendig”) [51]

Furthermore, recalculated pole figure plots were created to compare the obtained results:

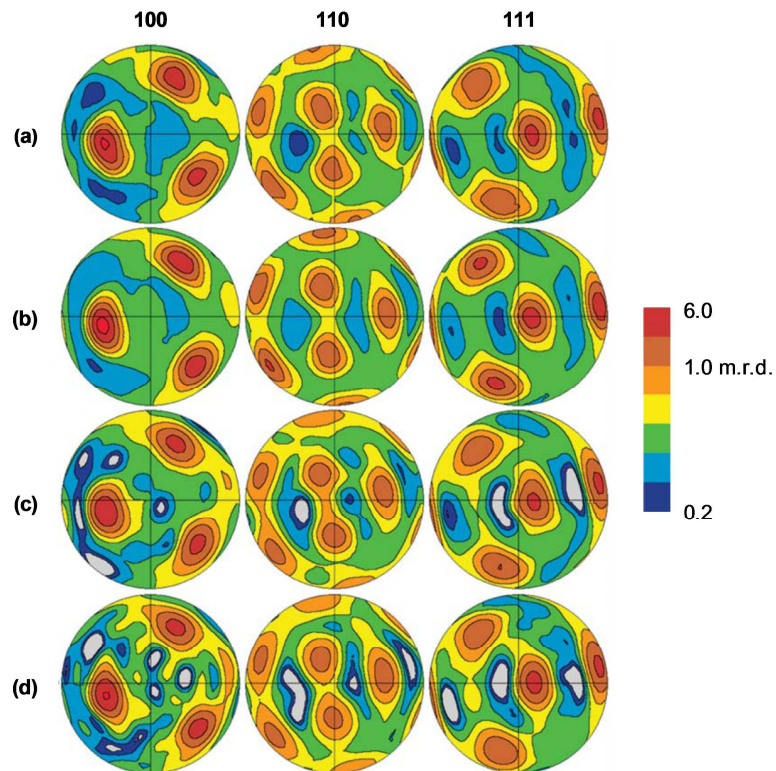


Figure 40: Pole figures of ECAP aluminium in selected crystal orientations 100, 110 and 111. (a) Recalculated pole figures from GULUWIMV ODF. (b) Recalculated pole figures from MAUD E-WIMV. (c) Calculated pole figures from MAUD harmonic method ($L = 12$). (d) Pole figures from GSAS data [51]

4.8 Deformation Analysis

Further research areas using neutron diffraction include fundamental studies of the deformation behavior of polycrystalline materials. The term deformation can be described and treated on the same basis as strain when an applied load such as tensile, compressive, bending or torsional forces are acting on a workpiece. These impacts deform the material elastically or plastically [52].

Neutron diffraction for deformation studies is carried out in-situ during mechanical testing (mainly during tensile tests) at room or simulated service temperatures using specially designed furnaces. The strain, both on a macroscopic and microscopic level, are determined as a function of the applied stress in order to obtain important information about the materials properties under load and at elevated temperatures (flow curves).

4.8.1 Elastic and Plastic Deformation

At low temperatures most of the materials exhibit an elastic behavior. External loadings generate reaction forces within the body, but they do not result in lasting changes in size and shape in the elastic range of the material. After unloading and deformation they get back to their original shape again. The linear elasticity and the stress-strain relation of the material are principally based upon Hooke's law as shown in (4.6.1) [52].

Crystalline materials basically offer the possibility of a plastic deformation through the presence of lattice defects (defect structure). Plastic deformation (= change of the defect structure) can be described by the motion of dislocations: This happens by the slip of crystal regions parallel to atomic layers of the crystal lattice. Slip is generally induced along certain crystallographic slip planes with the highest density of atoms under shear stress. Dislocation motion in slip systems (slip plane and orientation) occurs as soon as τ exceeds a critical value (critical shear stress τ_{crit}) depending on temperature, strain rate and several material parameters such as type of crystal lattice, its solid solution and

distribution of precipitates. The following illustration demonstrates the slip system of a monocrystalline tensile specimen exposed to uniaxial forces F .

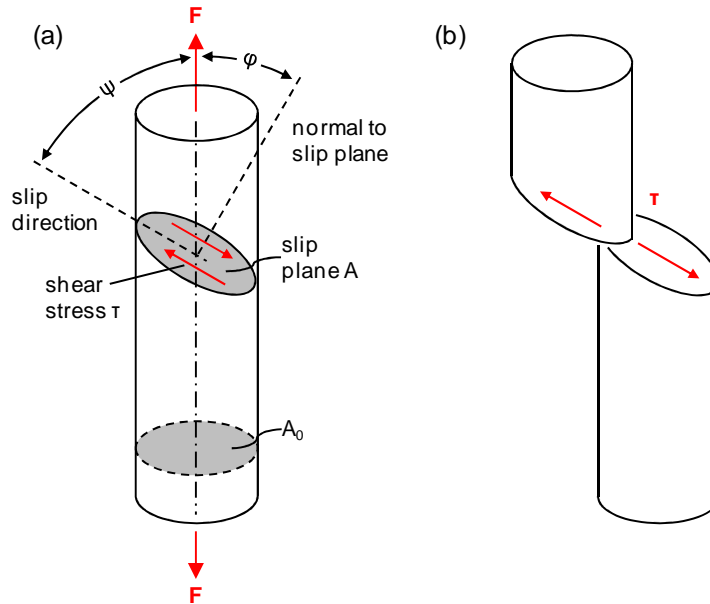


Figure 41: Cylindrical monocrystalline specimen subjected to uniaxial tensile stress. (a) Specimen with slip system. Uniaxial applied stress is equal F divided by A_0 . (b) Deformed specimen; slip along the slip plane starts at a critical shear stress τ_{crit} . Compiled by the author and based on [52]

The effective resulting shear stress in the slip system is given by Schmid's law as

$$\tau = \frac{F}{A_0} \cos \psi \cos \varphi = \sigma \cos \psi \cos \varphi. \quad (1.67)$$

Another possibility of a plastic deformation is the mechanism of the so-called twinning. Here, a crystal region is flipped on the slip plane to the twinning position (mirroring on a lattice plane) showing rearranged but undistorted crystal structures [52]. The third modification of plastic deformation is the thermodynamically effected and stress induced martensitic transformation [53].

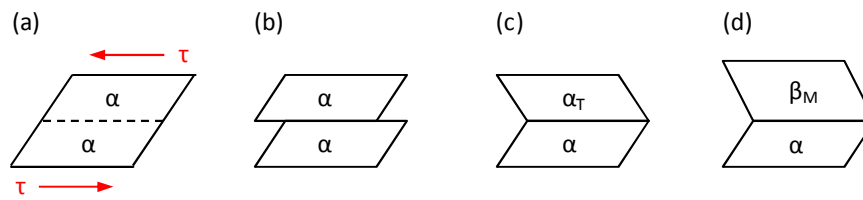


Figure 42: Types of plastic deformation. (a) External mechanical stress acting on a crystal system. (b) Slip. (c) Twinning. (d) Stress induced martensitic transformation. Compiled by the author and based on [53]

4.8.2 In-situ Deformation Studies

In-situ neutron diffraction measurements can be either carried out at room- or elevated temperatures. High-temperature creep tests, where the typical creep rupture times are more than several hundred or thousands hours (depending on the testing temperature and applied stress), are not always feasible for time and cost reasons. The experiments are based on interrupted creep tests (e.g. interruption of the creep tests at Graz University of Technology and resumption at VULCAN), where the discontinuance does not affect the creep behavior of the material. Main differences may appear in the mechanisms of the creep behavior of the performed test compared to the real creep-exposed material in service due to the shorter time frame and potentially increased temperatures and loads to induce the premature creep failure. The aim of the investigations is, however, to determine the in-situ macroscopic mechanical as well as lattice strain responses to the applied stress during tensile loading.

Some recent papers about neutron diffraction studies of different metallic alloys during deformation have already been published. Most of the experiments were based on room temperature tensile tests [54, 55, 56] or the tests were conducted at relatively low temperatures (50°C and 100°C) [57]. However, creep behavior of high-temperature materials, such as ferritic/martensitic 9%Cr steels used in power generation plants, are of great interest. Unfortunately, there is a dearth of literature on in-situ neutron diffraction measurements of high-temperature creep or tensile tests.

Daymond and Bouchard [58], for instance, examined a 316H stainless steel under loading at 20°C to 650°C and obtained very promising results. Neutron diffraction was performed at the ENGIN-X diffractometer at ISIS. Distinctive reflection peaks of the recorded diffraction spectra with regard to the lattice spacing were selected, where each diffraction peak stated a family of grains with a preferred crystal orientation (chosen crystallographic planes: 111, 311 and 200). GSAS was used to fit the peaks and obtain diffraction data. The data evaluation was done at a loading rate of 0.5MPa/s and at constant stresses. Furthermore, the measured experimental results and elastic-plastic behavior has been compared to the simulations of self-consistent models resulting in quite good agreement. Macroscopic strain and lattice strain responses under tensile loading at six different temperatures (20°C, 175°C, 300°C, 425°C, 550°C, 650°C) have been identified and analyzed. The 300°C, 425°C, 550°C curves showed typical characteristics of dynamic strain aging (DSA)^d [59] under uniform loading. Lines represent predictions and points measured data (Figure 43).

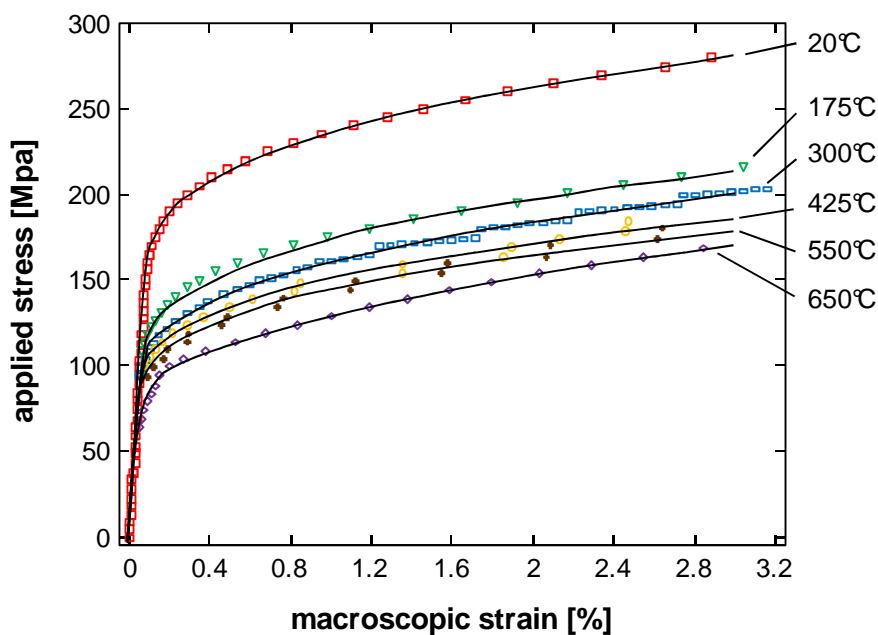


Figure 43: Macroscopic stress-strain curves at various temperatures

^d “Dynamic strain aging (DSA) in solid solutions is described as diffusion of solute atoms to mobile dislocations, temporarily arrested to obstacles. As a consequence, the solute concentration experienced locally by the dislocations depends on the time of arrest and the solute diffusion coefficient.” [59]. The characteristics can be seen in the inhomogeneous deformation (jerky flow), called “Portevin-Le Chatelier effect”.

The measured elastic lattice strain data of the grain families parallel and transverse to the loading direction showed a linear response within the macroscopically elastic regime (around 170-180MPa). Diversities of the different curve slopes of grain families depend on the elastic anisotropy. As the applied stress is further increased, the 200 families showed a change in slope representing a nonlinear relationship (Figure 44).

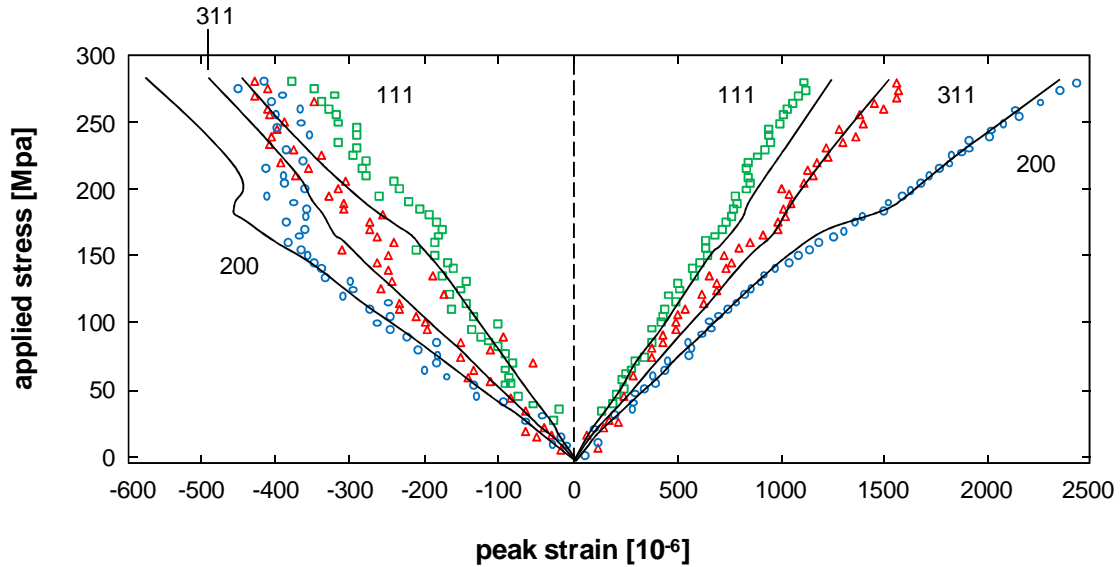


Figure 44: Transverse and axial grain family strains (111, 311 and 200) at room-temperature. Points are based on single peak fit and are presented without error ranges

Within the linear elastic regime the elastic constants were determined as a function of temperature by means of the method of least-squares (curve fitting to the experimental data) both in normal and transverse direction. The single-crystal elastic constants C_{ijkl} were calculated by using the approximation of Voigt and Reuss and the model of Kroner [40, 58].

Moreover, the observed plastic intergranular strains (difference between total strain and extrapolated elastic line) at different temperatures were compared with the predicted values (Figure 45). However, at a temperature of 650°C the measured values did not agree with the values of the used models. This can be especially seen for the 311 grain family, where the predictions show small compressive strains, while the measured points are within the tensile range.

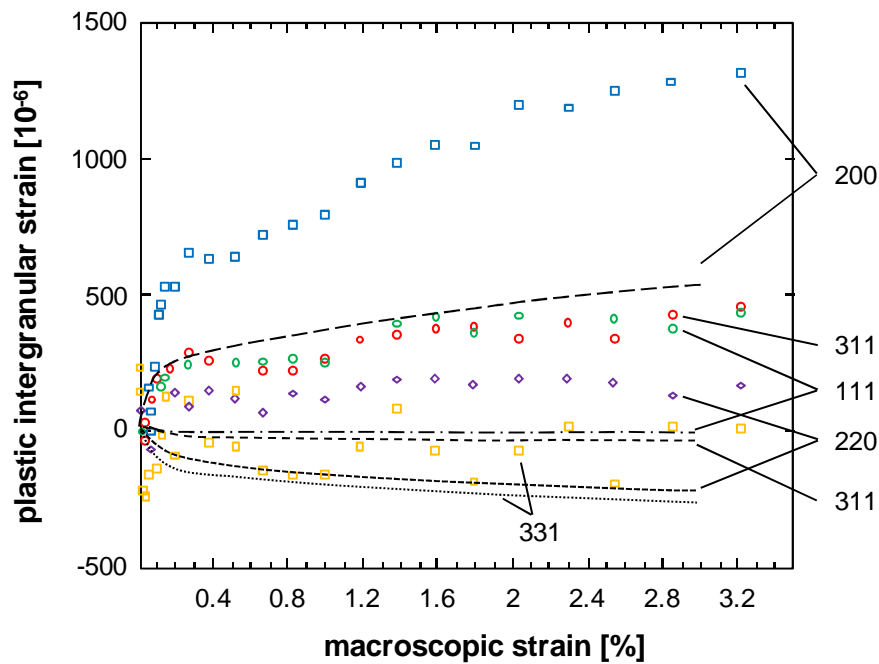


Figure 45: Axial plastic intergranular strains at 650°C

This can be more or less attributed to other and newer activated deformation mechanisms and grain boundaries which have become softer at elevated temperatures (creep) instead of the common slip as the prevailing mechanism. The real causes of these complex processes are still not completely understood [58].

4.9 Phase Transformation Analysis

It is very important to study the mechanisms of phase transformations and to understand how phases originate and how they are distributed within the material. These have a strong influence on materials properties and can be controlled among other things during heating/cooling and thermo-mechanical treatments. Neutron diffraction provides an observation of diffusional as well as diffusionless and time-dependent transformations in-situ, and is therefore a very appropriate and powerful technique to monitor e.g. martensitic transformations and precipitation processes.

4.9.1 Basics

In materials science and engineering the phase is a spatially homogeneous area with certain physical parameters such as density, structure and chemical composition. Phase transformations are categorized in homogeneous and heterogeneous transformation. The first is characterized by a concurrent appearance throughout the parent phase without any nucleation and includes spinodal decomposition and order-disorder transformation processes. Heterogeneous transformation on the other hand occurs by nucleation as well as growth and make up the bulk of phase transformations in materials and are classified in

- growth controlled by heat transfer (solidification of pure metals),
- growth controlled by heat and mass transfer (solidification of alloys),
- athermal growth (glissile interface), e.g. diffusionless martensitic transformation, and in
- thermally activated growth by individual movement of atoms to and across the interface between the parent and product phases (interface controlled if no change is evinced in composition and/or diffusion controlled by diffusion of atoms) [60].

Continuous reactions can be both interface and/or diffusion controlled e.g. precipitation- and dissolution processes whereas discontinuous reactions are only diffusion controlled and include eutectoid growth and discontinuous precipitation [60]. All these basics are important to understand the microstructural evolution during thermal and thermo-mechanical controlled processes (TMCP).

4.9.2 In-situ Study during Phase Transformations

Diffraction using neutrons can provide important data during different phase transformations. This high-class method has already been successfully employed by Tomota et al. [61] for an engineering steel to determine the microstructural

development during heating/cooling and TMCP. The testing was carried out using ENGIN-X at ISIS on a low alloyed steel sample with a starting microstructure of martensite. By an increase of the temperature, it could be observed that the FWHM decreased due to the decreasing of the tetragonality of martensite. A peak shift due to the thermal expansion could also be monitored. Changes in the observed diffraction profiles with further heating showed the slow growth of fcc-austenite (γ) grains where the microstructure became fully austenitic at around 1173K. The variation of the lattice parameters of γ could be attributed to the decrease of the carbon concentration. The subsequent continuous cooling revealed the transformation of austenite to body-centered cubic (bcc) -ferrite (α) and eutectoid pearlite (lamellar ferrite-cementite structure). In addition, no austenite could be observed of less than 560°C (833K). At room temperature, the peak intensity of the diffraction profile was higher than the initial microstructure characterizing a strongly textured material (Figure 46).

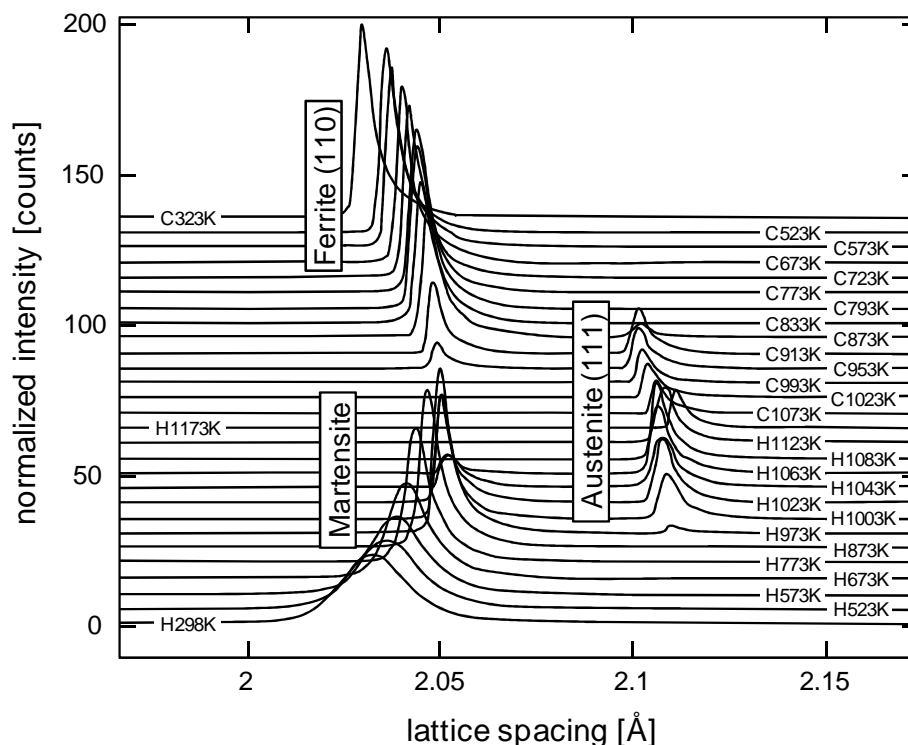


Figure 46: Observed diffraction profiles during heating (H) and cooling (C) on a low alloyed steel. Starting microstructure is martensite, complete austenization at 900°C (1173K) and transformation to ferrite after cooling [61]

The experiments during TMCP (heating: 5K/s, austenization: 1173K, cooling down and holding at 913K and 25% compression during this isothermal process) indicated two different results by comparing them with the observed diffraction profiles before compression: After compression the material showed a texture evolution of both α and retained γ (change in intensity) and an acceleration of ferrite transformation by plastic deformation [61].

In summary, the measurements have shown that in-situ neutron diffraction also provides quite accurate results for such experiments e.g. like in-situ synchrotron x-rays. Future instruments like VULCAN with a better time resolution may enable more precise examinations of quick processes like martensitic transformations.

5. The Spallation Neutron Source at Oak Ridge

The Spallation Neutron Source or SNS is located at Oak Ridge National Laboratory (ORNL) in Tennessee, USA. It is an accelerator-based world-class facility built in April 2006 and produces the most intense and brightest pulsed neutron beams in the world. The construction and installation took place within the framework of six U.S. Department of Energy (DOE) national laboratories.

The pulses of neutrons are used in diverse scientific and technical fields of research such as medicine, telecommunications, biotechnology, manufacturing and information technology. The neutron scattering instruments act like flashing strobes which provide a fast illumination of objects and support scientists to understand and engineer materials properties at the atomic level without damaging the parts. Figure 47 shows the central laboratory and office complex (left curved building) as well as the center for nanophase materials sciences on the right. The rectangular building in the back is the SNS instrument hall including the engineering materials diffractometer VULCAN [62,63].

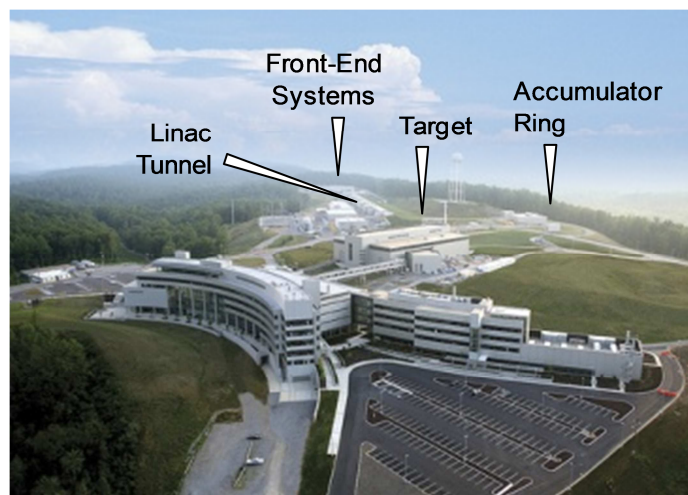


Figure 47: Aerial view of the SNS in Oak Ridge. Most of the accelerators are located underground. ORNL Neutron Sciences [62]

Technical parameters of the SNS are listed in the Appendix D.

5.1 Functionality

Basically the SNS consists of five major objects for the entire neutron generation process:

- 1) front-end system
- 2) linear accelerator (linac)
- 3) accumulator ring
- 4) target and
- 5) neutron detector instruments.

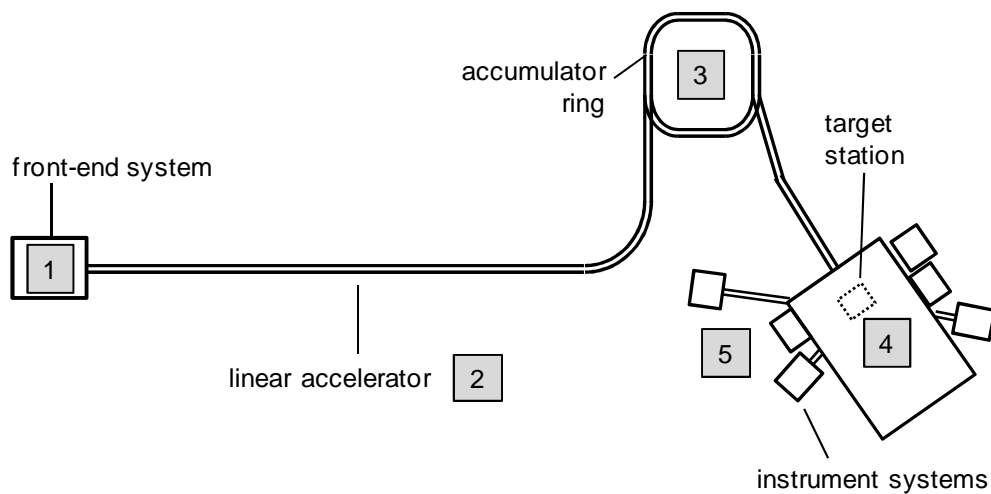


Figure 48: Layout of the SNS facility

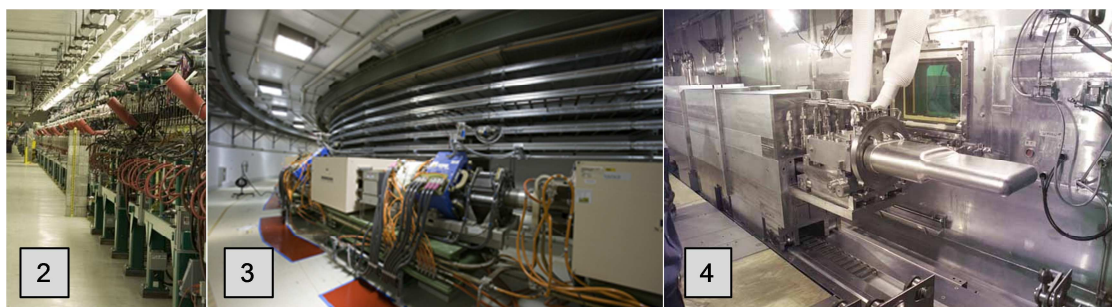


Figure 49: Linear accelerator with a length of 331m (left). Middle: Accumulator ring tunnel. Right: Liquid mercury target inside the building [62]

5.1.1 Front-End System

The front-end system contains an ion source, which produces negatively charged hydrogen H^- ions (each H-atom has two electrons instead of one, and one proton). The negative hydrogen ions are cut into minipulses of 645 nanoseconds duration and initially accelerated to kinetic energies about 2.5MeV. These are particularly well suited for the acceleration at the subsequent step and can be efficiently injected into the accumulator ring in the third step.

5.1.2 Linac

The linear accelerator (made up of three different types) focuses the injected ions into a pulsed beam and accelerates it to very high energies from 2.5 from the first step to 1000MeV. Superconducting radio-frequency cavities of niobium around metal realize the highest speed of the ions. Thus, the particles reach a velocity of approximately 90% of the speed of light. A magnetic lattice focuses and steers the beam through the cavities. Special mounted devices supply the operators with useful data about the suitability for the injection into the accumulator ring which will be described in the following.

5.1.3 Accumulator Ring

The high-energy beam from the linac stage enters the accumulator ring tunnel (ring circumference: 248m). Here, the H^- particles are passed through a carbon foil that strips off each ion's two electrons, producing positively charged hydrogen ions and hence protons. The protons keep on circulating in the tunnel ring where they accumulate in bunches for over 1000 turns. Thereupon, the proton bunches are kicked out abruptly producing proton pulses less than 10^{-6} seconds directed at the target bombarding it 60 times a second.

5.1.4 Target

The energetic 1GeV proton beam strikes a liquid mercury (Hg) target, leaving a highly excited nucleus producing millions of neutrons (= spallation). This heavy metal, which is being used for the first time in neutron spallation sources, possesses rather better properties compared to other solid targets such as tantalum at the ISIS or tungsten at LANSCE. The liquid state (the only metal which is liquid at room temperature) can better dissipate the generated heat from the collisions and has better energy-absorbing characteristics. Furthermore, it is an element with a high atomic number (number of electrons/protons: 80, number of neutrons: 121) being able to produce a large amount of neutrons. Moreover, mercury is not sensitive to radiation damages.

5.1.5 Neutron Detector Instruments

The generated neutrons from the spallation process are formed into specific high-intense or very bright beams. Before that, the produced high-energy neutrons need to be cooled down to 0.1 – 10 meV for scientific purposes (see chapter 4.2.2). The moderation is carried out with water (running at 290K) to generate thermal and liquid hydrogen (20K) to generate cold neutrons. Afterwards, these are guided to the respective neutron detector instrument and are appropriate for materials research. At present, there are 14 instruments available, 5 are to be commissioned in the next few years and 3 are under development or in the planning stage on a total number of 18 neutron beam shutters [62]. The SNS hall and its instruments are given in the Appendix E. A brief description of the individual scattering instruments gives reference [63]. The engineering materials diffractometer VULCAN will be treated separately in the next section.

5.2 The Engineering Materials Diffractometer VULCAN

VULCAN at the SNS in Oak Ridge, which is named after the Roman god of fire and metal working, is one of the world's leading engineering diffractometers, facilitating unprecedented insights into the behavior of materials and components. The engineering design started in November 2003 and three years later the ground-breaking was set for the VULCAN-building. Finally in June 2009, the shutter was opened for the first time and the whole instrument is currently almost ready for complete measurements (some upgrades are still on running). Figure 50 shows the CAD-model of VULCAN and its area of operation [64].

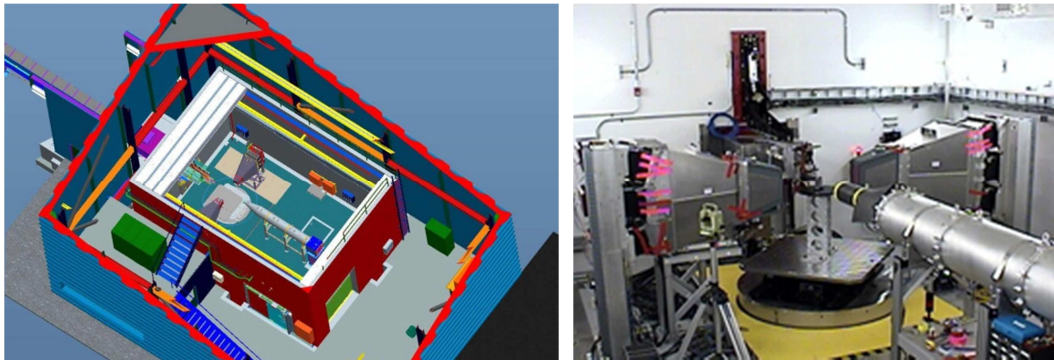


Figure 50: VULCAN diffractometer at the SNS
Left: CAD-Model. Right: Area of operation [64]

The application of the machine covers a wide range of research activities. However, the main fields of use are strain-stress measurements and deformation studies. High-intense neutron fluxes on the specimens enable fast recording of the diffraction spectra providing beneficial real-time measurements of material kinetics. The coupling of a SANS instrument with the VULCAN diffractometer offers a unique possibility to observe extraordinary results simultaneously by combining and exploiting the capabilities of both tools. This is of particular interest for phase transformation analysis at manifold length scales, which can be performed in sub-seconds. The technical characteristics and schematic layout are summarized below [64, 65, 66].

Table 7: Specifications of VULCAN [64]

Moderator	Decoupled poisoned water
Source-to-sample-distance (L_1)	43.5m
Sample-to-detector-distance (L_2)	1.5 – 2m
Detector angular coverage	$60^\circ < 2\theta < 150^\circ$
Wavelength bandwidth	0.9 – 2.2Å
Resolution	0.2 % in high-resolution mode. This configuration is adequate for common engineering components of iron and aluminium (resolution of around 20 peaks). The resolution Q can go up to 0.6 %, depending on the detector angle.
Flux on sample [n/s/cm ²] see Figure 52	3.0×10^7 in high-resolution mode 1.2×10^8 in high-intensity mode
Gauge volume	3-dimensional strain mapping with a sample gauge volume of 1mm ³ . Single directional mapping (1D) with a spatial resolution of 0.1mm. Measurement time of minutes for both cases.
SANS Q-range	$0.01 - 0.2 \text{Å}^{-1}$

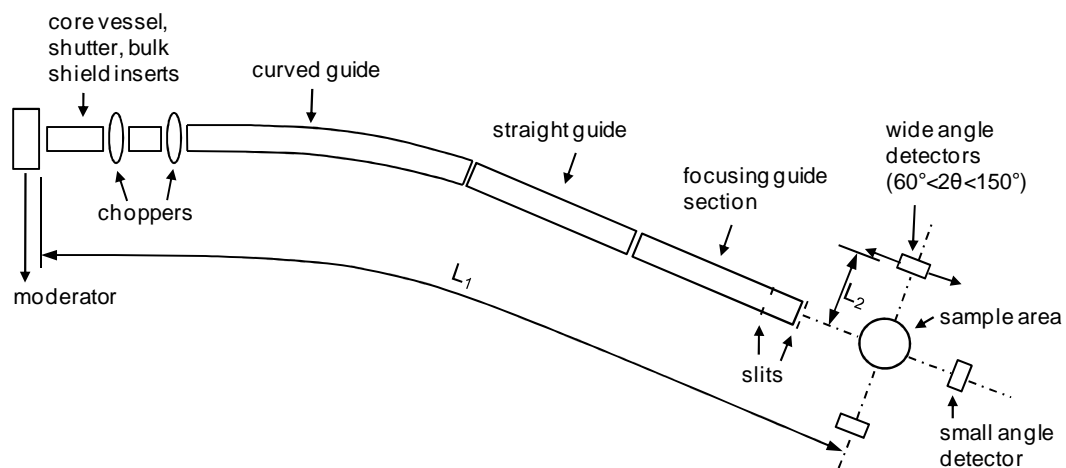


Figure 51: Schematic layout of VULCAN. Compiled by the author and based on [66]

The wavelength spectra both in high-intensity and high-resolution mode at VULCAN are illustrated below.

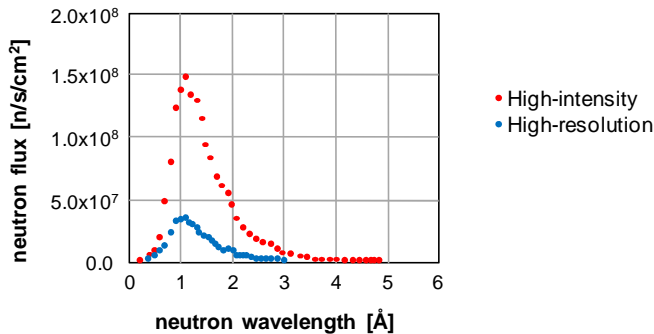


Figure 52: Wavelength distribution at VULCAN. Compiled by the author and based on reference [65]

The features of VULCAN will open up extensive opportunities for scientists such as in-situ studies of materials during processing to illustrate the temperature distribution, texture evolution, residual stress distributions as well as precipitation behaviors. In-situ loading and deformation studies of alloys and amorphous materials at elevated or cryogenic temperatures with about 20 well-defined reflections may realize the investigation of complex creep and fatigue failures. Further fields of application are surface strain/stress measurements and microstructure changes of e.g. coated, shot- or hammer peened components [64].

5.2.1 Sample Environment

The SNS provides a wide range of auxiliary equipment to simulate specific conditions such as thermal stresses and loadings and to set the specimens into a state, as they are exposed during service. Its sample environment inventory includes liquid helium cryostats, closed cycle refrigerators, furnaces, magnet systems, ultra-low temperature devices, high pressure cells, load-frames and special environments such as controlled humidity cells. These accessory testing units are often developed through collaboration and are particularly custom-made for the appropriate SNS instruments or may be shared at the different beam lines within the facility. Some are still in an experimental stage in order to enhance the technological capabilities and to tap the full potential of the neutron scattering technique [62].

VULCAN principally uses specific equipment such as a multi-axial load-frame, an ILL vacuum furnace and a heavy duty sample table. The main features of these relevant instrumentations are presented in the next sections.

5.2.1.1 VULCAN load-frame

Basically, load-frames are designed to meet the demands of scientists and engineers in R&D and quality control by studying the elastic and plastic behavior of materials as well as phase transformations under certain complex loading conditions. They are used to perform in-situ deformation studies (e.g. tension, compression or torsion) in order to obtain a multitude of information concerning materials properties. These include among other things the fatigue limit, yield strength, Young's modulus, tensile and compressive strength, ductility and creep relaxation properties.

The multi-axial high-capacity load-frame (Figure 53), funded by the National Science Foundation (NSF), is the major load-frame at VULCAN and features a load capacity of 100kN both for tension and compression, 400Nm for torsion and up to 30Hz for dynamic multi-axial fatigue tests. There are also some smaller load-cells available for smaller samples (cross sections: $\sim 1.5 - 8\text{mm}$).

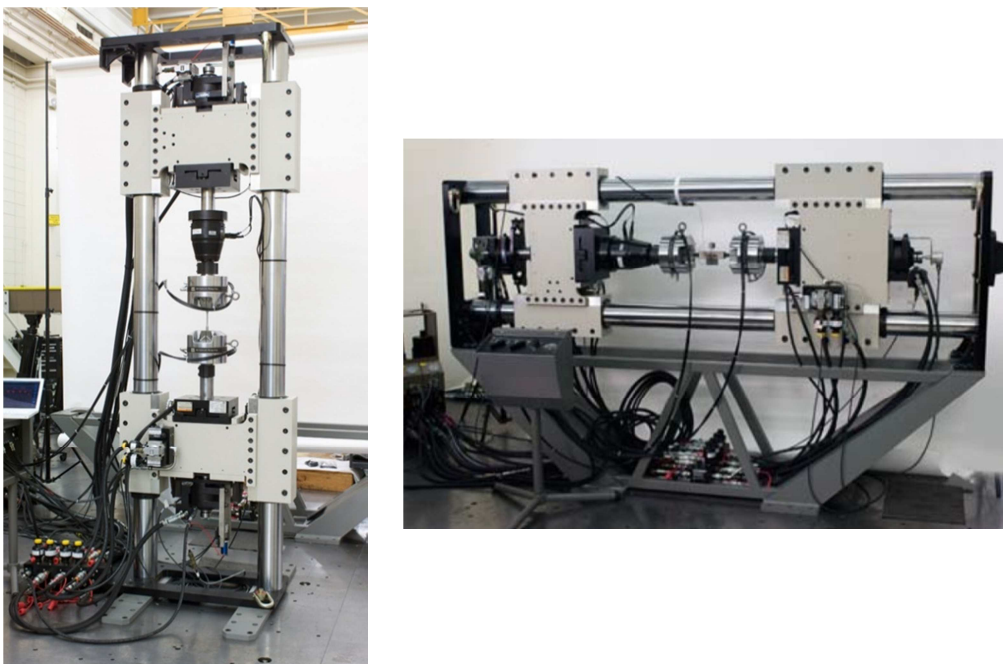


Figure 53: VULCAN high-capacity load-frame [62]

This device uses opposing actuators, ensuring that the sample gauge volume is fixed in space, which is particularly interesting for multiprobe analysis. Thus, other testing instruments such as an optical microscope can be attached to observe e.g. the evolution of surface cracks simultaneously. Furthermore, the machine can be positioned either vertically or horizontally (Figure 53) [62, 67].

Past issues of in-situ measurements at VULCAN evinced the promising scientific capabilities of the instrument, even though smaller uniaxial in-house load-frames have been successfully utilized. Upon consultation with the instrument scientist leader Mr. Ke An, it is also possible to execute in-situ thermo-mechanical tests on metallic samples up to 1000°C by induction heating.

5.2.1.2 ILL 1800°C Furnace

The 1800°C vacuum furnace (Figure 54), designed by the ILL of Grenoble, is a proven tool to generate ambient temperatures of 1600°C, for short periods even up to 1800°C.

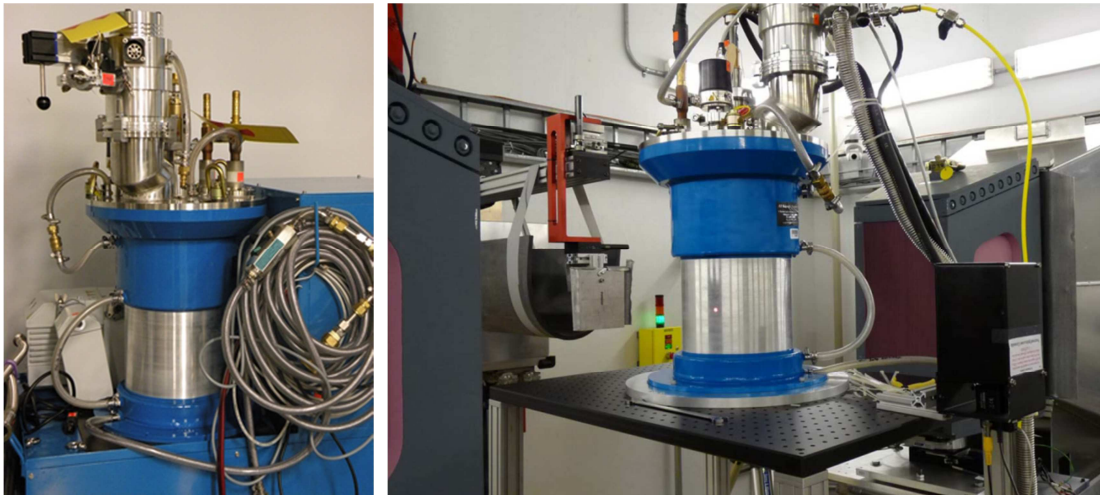


Figure 54: The ILL 1800°C vacuum furnace. Right: Mounted at the VULCAN instrument [62]

It consists of an aluminium body shell and in-house created high-temperature sample containers made of vanadium, especially customized for the instrument layout of VULCAN. These include two different sample cells, where the

specimens may be stabilized by either a screw or a wire. Niobium shielding and heating elements realize the heat storage within the furnace.

Furthermore, window segments made of niobium and aluminium enable a whole 360° access of the neutrons in the scattering plane [62].

In-situ neutron diffraction studies of phase transformations, crystallization and recrystallization in metals and alloys as well as in bulk metallic glasses can be monitored using the ILL vacuum furnace at the VULCAN diffractometer.

5.2.1.3 Heavy Duty Sample Table

The sample table is the central part of the instrument, conceptualized to position huge industrial components with a weight up to 2 tons (Figure 55). It weighs around 10 tons with a table surface of 2.5m². This device is marked by its highly precise position accuracy of 0.01mm and enables a large shift of the x, y and z-axis of 0.5m with a full rotation of 360°. In the retracted state, the top surface is positioned at 1.5m from the center line of the neutron beam, facilitating measurements of parts up to 3m in height [62].



Figure 55: Heavy duty sample table [62]

This apparatus is of special interest for neutron diffraction studies of whole prefabricated elements such as tubing segments for thermal power plants.

Last but not least, a possible experimental setup at VULCAN for creep-exposed specimens from the IWS institute will be discussed next.

6. Possible Experimental Procedures at VULCAN

Different materials testing methods are often insufficient to investigate and understand the in-situ materials behavior under simulated and complex conditions. TOF neutron diffraction at the SNS may enable scientists to gain unique insights into the unexplained high-temperature mechanisms of the HAZ in creep-exposed 9%Cr crosswelds that were previously infeasible.

This chapter presents a possible experimental setup at VULCAN in order to execute future in-situ diffraction analysis, in fact an interrupted high-temperature creep test of the running IWS samples (chapter 4.8.2). As described before, this state-of-the-art engineering diffractometer allows users to conduct highly-resolved and rapid thermo-mechanical experiments, by using the load-frame coupled with an appropriate induction heating system. The focus will be on the determination and monitoring the intergranular strain evolutions, consequently the residual stresses, macroscopic strain-stress relations and other simultaneously occurring phenomena under loads.

6.1 Testing Materials

The material is the martensitic steel grade NPM4 as briefly introduced in chapter 3.3. The chemical composition of this material is given in the following table.

Table 8: Chemical composition of NPM4

		Analysis (wt. %)						
NPM4	C	Si	Mn	P	S	Cr	Ni	V
	0.09	0.299	0.509	0.001	0.003	9,26	-	0.199
	W	Nb	N	Al	B	Co	Ti	
2.92	0.05	0.01	0.004	0.0114	2.88	-		

The steel was austenized at 1150°C for 1 hour and air-cooled, and tempered at 770°C for 4 hours and subsequently cooled in air as well. The experiments will include in-situ tensile tests of welded creep-samples at elevated temperatures

according to DIN EN 10002-5 with the aim to monitor the different occurring phenomena in the HAZ. Welded plates were cut into slices which were turned to specific cylindrical samples as illustrated in Figure 57.



Figure 56: Welded creep specimen NPM4

The sample geometry is shown below.

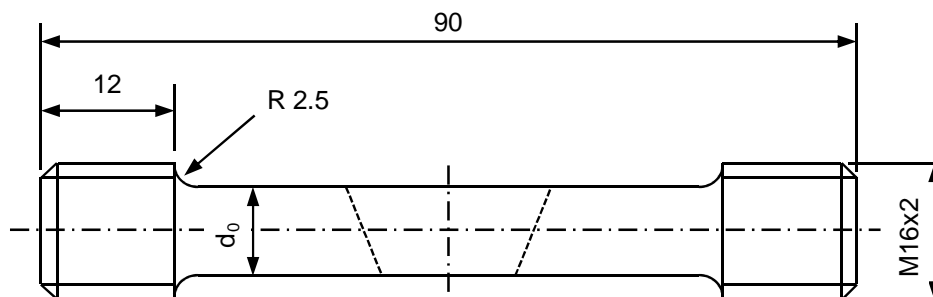


Figure 57: Sample geometry of cross-welded specimens. The weld metal zone is symbolically presented as a dashed line

6.2 Sample Preparation

The VULCAN multi-axial high-capacity load-frame with 100kN will be used for the in-situ neutron diffraction studies at ambient temperatures. Since the stress (1. 59) is defined as

$$\sigma = \frac{F}{A},$$

where F is the force and A the effective cross-section, one can write

$$\sigma = \frac{100.000 \text{ [N]}}{\left(\frac{9}{2}\right)^2 \pi \text{ [mm}^2\text{]}} = 1571.9 \left[\frac{\text{N}}{\text{mm}^2} \right].$$

This is the maximum tensile and compression load for $d_0 = 9\text{mm}$. Taking the effect of the necking phenomena into consideration, this max load should be sufficient for the tensile tests at each temperature level.

For the in-situ experiments at elevated temperatures, the use of the smaller load-frame with the induction heating system should be sufficient. For the purpose of both versions the schematic layout of the experiment demonstrated in Figure 58.

The detectors are arranged at a fixed angle of $\pm 90^\circ$ to record the scattering vectors both parallel and perpendicular to the loading direction at the same time. The specimen has to be moved along certain directions with a defined small gauge volume of e.g. $1 \times 1 \times 1 \text{mm}^3$. At other diffractometers it was difficult to work with small gauge volumes, since the measurements would simply take too long. In addition, the VULCAN instrument is equipped with an integrated SANS detector to observe important data about e.g. the change in shape and size of nanoparticles in the material simultaneously.

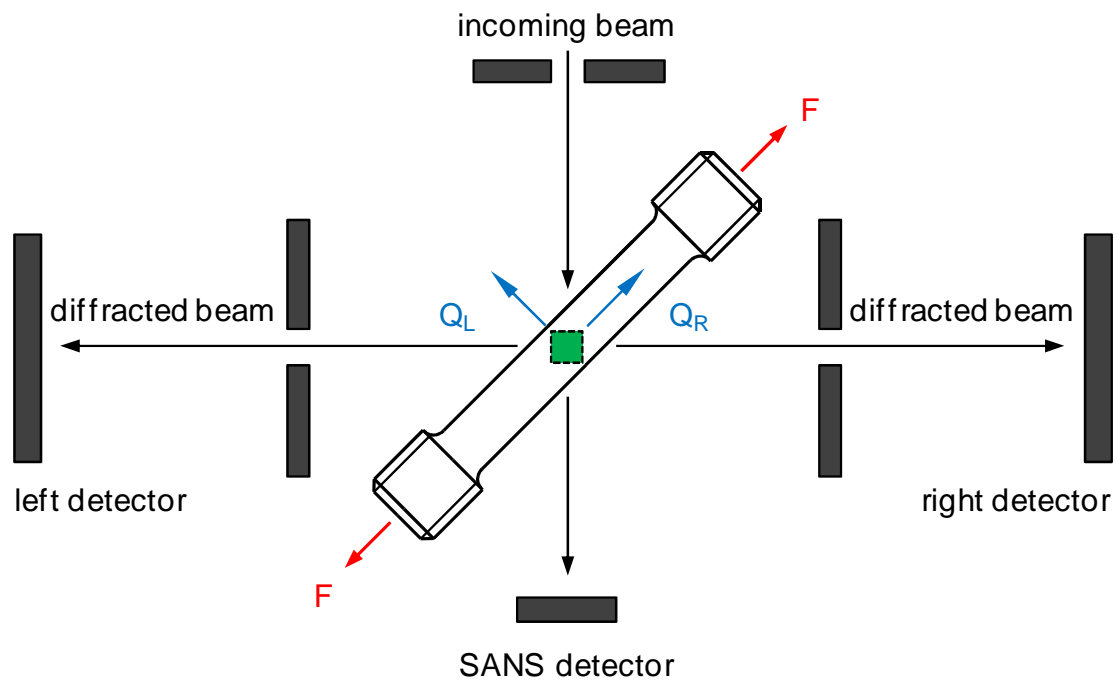


Figure 58: Arrangement of the in-situ neutron diffraction experiment during mechanical testing and induction heating at VULCAN. Q_L = scattering vector left detector (Q-radial). Q_R = scattering vector right detector (Q-axial). The small green square characterizes the sample gauge volume

6.3 Data Analysis

By detecting the time-of-flight of the neutron beam of a wavelength spectrum of $0.9 - 2.2\text{\AA}$, it is now possible to determine the interplanar spacings d_{hkl} using Bragg's law:

$$d_{hkl} = \frac{\lambda}{2\sin\theta_{hkl}}$$

The diffraction patterns are then plotted as a function of these recorded lattice spacings and the intensities by using the GSAS software and the Rietveld method. Each individual peak of the obtained diffraction profile corresponds to a certain $\langle hkl \rangle$ reflection of grain families. The changes in the spectra give different information about the materials condition during loading and heating as described in subchapter 4.4.2.1.

In order to get the strain/stress –values, a reference lattice spacing d_{hkl}^0 of the stress-free material needs to be determined beforehand. In the case for the welded specimens it may be necessary to measure d_{hkl}^0 between the HAZ and the shaft shoulder. The elastic lattice strain may then be ascertained using equation (1. 39)

$$\varepsilon = \frac{d_{hkl} - d_{hkl}^0}{d_{hkl}^0},$$

and further using Hooke’s law (1. 63) and (1. 66) to determine the macroscopic and microscopic stress values. The strain responses both intergranular and macroscopic during tensile tests at defined temperature levels (e.g. [58]) may indicate useful data of e.g. accelerated grain boundary sliding by exceeding a certain threshold initiated through different occurring mechanisms within the material. One may also calculate the evolution of the dislocation density during deformation as a function of the microstrain. Other important information may be obtained by recording the texture changes during the tests. VULCAN uses special programs such as POLFPLOT for pole figure plotting. Here, one may see the changes in individual grain family orientations during tensile loading.

Furthermore, the development of precipitates and intermetallic phases may be monitored with the coupled SANS instrument with the respective software in order to observe, inter alia, the changes in volume fraction and number density of the particles. The occurring coarsening effects may be also of great interest.

Finally, chapter 8 summarizes the content of this work and gives a brief perspective on the future of the neutron diffraction technology.

7. Summary and Outlook

USC components such as piping systems of advanced 9%Cr steels are widely used in power generation plants. Welding in all its forms is the most common joining technology utilized in such industries and will also remain in the future. Welding processes strongly influence the materials creep properties and decrease the creep rupture strength up to half of the base metal strength. Premature creep failures basically occur within the fine-grained or intercritical region of the HAZ after some time in service which may lead to cracks and breakdowns, respectively. Long-term creep tests have shown that type IV cracking in martensitic 9%Cr steels is the most noted and prevalent failure mode. This immediately raises the question, which factors really induce this phenomenon. Despite intensive efforts, the mechanism of type IV cracking has not yet been completely clarified. Therefore, various approaches have been used to substantiate the reasons for these defects with the aim of extending the service life significantly.

Neutron diffraction, for instance, is one of the most promising techniques to study this complex processes in-situ by using appropriate supplementary equipment to simulate the impacts of in-service conditions such as temperature, compression or tensile loads. It is a very attractive and complementary tool compared to other diffraction methods and enables the investigation of bulk parts. However, the target was to show the possibilities of diffraction using neutrons and the potential opportunities for future purposes.

In a first step of the present study, the fundamentals of neutron scattering and its advantages have been explained, followed by a demonstration of the different capabilities by applying this method to engineering science. These include strain and stress, texture, deformation as well as phase transformation analysis. Each chapter contains the theoretical principles of each field of application and is rounded off with previous conducted experiments by scientists and engineers around the world. Additionally, a presentation of the SNS in Oak Ridge and of the sophisticated time-of-flight engineering materials diffractometer VULCAN

was shown in a separate chapter. VULCAN provides rapid and high-resolution measurements of bulk samples and was recently put into operation. The device uses coupled diffraction and SANS instruments, enabling the observation of several mechanisms simultaneously. The instrument uses specific software like GSAS or Rietveld to compute and display quantitative and qualitative diffraction data. It is expected that it may realize unprecedented insights into the high-temperature response of cross-welded structures, since there is a lack of understanding of the microstructural effects on the strain/stress evolution during high-temperature creep.

Last but not least, an experimental setup at VULCAN for the study of creep-exposed weld-specimens was presented. The use of VULCAN may contribute to a better understanding of strain/stress and creep rupture behavior in order to overcome the type IV phenomenon.

List of Literature

- [1] Streicher, W. (2010). Energy and Environment - Lecture Notes. Graz: Graz University of Technology.
- [2] Booras, G. S., Viswanathan, R., Weitzel, P., & Bennett, A. (2003). Economic Analysis of Ultra-Supercritical PC Plants. *Pittsburgh Coal Conference*. University of Pittsburgh.
- [3] Klueh, R. L., & Harries, D. R. (2001). *High-Chromium Ferritic and Martensitic Steels for Nuclear Applications*. West Conshohocken, PA, USA: ASTM International.
- [4] Cerjak, H., & Mayr, P. (2008). Creep Strength of Welded Joints of Ferritic Steels. In F. Abe, & T. U. Kern, *Creep-Resistant Steels* (pp. 472-503). Boca Raton, FL, USA: CRC Press.
- [5] *Spallation Neutron Source*. (2011). Retrieved February 22, 2011, from Oak Ridge National Laboratory - Neutron Sciences: <http://neutrons.ornl.gov/>
- [6] Abe, F. (2008). Introduction. In F. Abe, T. U. Kern, & R. Viswanathan, *Creep-Resistant Steels* (pp. 3-14). Boca Raton, FL, USA: CRC Press.
- [7] Sommitsch, C. (2010). Materials Science - Lecture Notes. Graz: Graz University of Technology.
- [8] Kassner, M. E., & Pérez-Prado, M. T. (2004). *Fundamentals of Creep in Metals and Alloys*. Oxford, UK: Elsevier Ltd.
- [9] ECCC Data Sheet: Steel 91. (2005).
- [10] ECCC Data Sheet: Steel ASTM Grade 92. (2005).
- [11] ECCC Data Sheet: Steel E911. (2005).
- [12] Scarlin, B., Kern, T. U., & Staubli, M. (2005). The European Efforts in Material Development for 650°C USC Power Plants - COST522. In R. Viswanathan, D. Gandy, & K. Coleman, *Advances in Materials Technology for Fossil Power Plants - Proceedings from the 4th International Conference* (pp. 80-99). South Carolina, USA: ASM International.

- [13] Mayr, P. (2007). Evolution of Microstructure and Mechanical Properties of the Heat Affected Zone in B-containing 9% Chromium Steels - Doctoral Thesis. Graz: Graz University of Technology.
- [14] Bauer, M. (2009). *"Lebensdaueroptimierung von Schweißverbindungen martensitischer Stähle für Hochtemperaturanwendungen"* - Doctoral Thesis. Stuttgart: Materials Testing Institute University of Stuttgart.
- [15] Ennis, P. J., & Filemonowicz, C. (2002). Recent Advances in Creep-Resistant Steels for Power Plant Applications. In *OMMI - Power Plant: Operation Maintenance and Materials Issues Vol. 1, Pt. 1* (pp. 1-28).
- [16] Kern, T.-U., Mayer, K. H., Donth, B., Zeiler, G., & DiGianfrancesco, A. (2010). The European Efforts in Development of new High-Temperature Rotor Materials - COST536. *9th Liège Conference on Materials for Advanced Power Engineering*.
- [17] Mayr, P., Mendez-Martin, F., Holzer, I., Agüero, A., González, V., Baumgartner, S., et al. (2009). Experience with 9Cr3W3CoVNbBN Base Material and Crosswelds at 650°C for Implementation in USC Power Plants. *Proceedings of the 3rd Symposium on Heat Resistant Steels and Alloys for High Efficiency USC Power Plants*. Tsukuba, Japan: NIMS.
- [18] Abe, F. (2008). Strengthening Mechanisms in Steel for Creep and Creep Rupture. In F. Abe, T. U. Kern, & R. Viswanathan, *Creep-Resistant Steels* (pp. 279-304). Boca Raton, FL, USA: CRC Press.
- [19] Sonderegger, B. (2005). Charakterisierung der Substruktur in modernen Kraftwerkswerkstoffen mittels der EBSD Methode - Doctoral Thesis. Graz: Graz University of Technology.
- [20] Francis, J. A., Mazur, W., & Bhadeshia, H. D. (2006). Type IV Cracking in Ferritic Power Plant Steels. In *Materials Science and Technology Vol.22, No.12* (pp. 1387-1395).
- [21] *Nobel Prize in Physics*. (2011). Retrieved March 15, 2011, from Official Website of the Nobel Prize: http://nobelprize.org/nobel_prizes/physics/laureates/
- [22] Carpenter, J. (2010). *Neutron Sources for Materials Research*. Oak Ridge National Laboratory: Lecture Notes.
- [23] Pynn, R. (2010). *An Introduction to Neutron Scattering*. Oak Ridge National Laboratory: Lecture Notes.

-
- [24] Bauer, E. (2011, March). Neutrons and Instrumentation. *NESY-7th International Winter School on Neutrons and Synchrotron Radiation*.
- [25] *Radioactive Wastes - Myths and Realities*. (2011). Retrieved March 20, 2011, from World Nuclear Association: <http://www.world-nuclear.org/info/inf103.html>
- [26] Carpenter, J. (2004). *Neutron Production, Moderation and Characterization of Sources*.
- [27] Squires, G. L. (1978). *Introduction to the Theory of Thermal Neutron Scattering*. Cambridge, UK: Cambridge University Press.
- [28] Sears, V. F. (1992). Neutron Scattering Lengths and Cross Sections. In *Neutron News Vol. 3, No.3* (pp. 26-37).
- [29] de Novion, C. H. (2003). The use of Neutrons for Materials Characterization. In M. E. Fitzpatrick, & A. Lodini, *Analysis of Residual Stress by Diffraction using Neutron and Synchrotron Radiation* (pp. 3-27). London: Taylor & Francis.
- [30] Windsor, C. G. (1986). Experimental Techniques. In K. Sköld, & D. L. Price, *Methods Exp. Phys. 23A* (pp. 197-257). Orlando: Academic Press Inc.
- [31] Withers, P. J. (2007). Mapping Residual and Internal Stress in Materials by Neutron Diffraction. In *C. R. Physique 8* (pp. 806-820).
- [32] Santisteban, J. R., Daymond, M. R., James, J. A., & Edwards, L. (2006). ENGIN-X: A Third-Generation Neutron Strain Scanner. In *Journal of Applied Crystallography 39* (pp. 812-825).
- [33] Sprauel, J. M. (2003). Study of Second- and Third-Order Stresses. In M. E. Fitzpatrick, & A. Lodini, *Analysis of Residual Stress by Diffraction using Neutron and Synchrotron Radiation* (pp. 78-96). London: Taylor & Francis.
- [34] Wang, X. L. (2006). The Application of Neutron Diffraction to Engineering Problems. *Journal of the Minerals, Metals and Materials Society Vol. 58 no. 3*, pp. 52-57.
- [35] Larson, A. C., & Von Dreele, R. B. (2004). *General Structure Analysis System GSAS (Report LAUR 86-748)*. Los Alamos, New Mexico: Los Alamos National Laboratory.

- [36] Lelong, G., Price, D. L., & Saboungi, M. L. (2011). Scattering Techniques. In N. Kanellopoulos, *Nanoporous Materials - Advanced Techniques for Characterization, Modeling and Processing* (pp. 3-52). Boca Raton FL - USA: Taylor & Francis.
- [37] Leitner, H., Staron, P., Clemens, H., Marsoner, S., & Warbichler, P. (2005). Analysis of the Precipitation Behaviour in a High-Speed Steel by means of Small-Angle Neutron Scattering. In *Materials Science and Engineering A 398* (pp. 323-331).
- [38] Zickler, G. A., Schnitzer, R., Radis, R., Hochfellner, R., Schweins, R., Stockinger, M., et al. (2009). Microstructure and Mechanical Properties of the Superalloy ATI Allvac® 718Plus™. In *Materials Science and Engineering A 523* (pp. 295-303).
- [39] Coppola, R., Fiori, F., Little, E. A., & Magnani, M. (1997). A Microstructural Comparison of two Nuclear-Grade Martensitic Steels using Small-Angle Neutron Scattering. In *Journal of Nuclear Materials 245* (pp. 131-137).
- [40] Lodini, A. (2003). Calculation of Residual Stress from Measured Strain. In M. E. Fitzpatrick, & A. Lodini, *Analysis of Residual Stress by Diffraction using Neutron and Synchrotron Radiation* (pp. 47-59). London: Taylor & Francis.
- [41] Radaj, D. (2002). *Welding Residual Stresses and Distortion - Calculation & Measurement*. Düsseldorf: DVS Verlag.
- [42] Winholtz, R. A. (2003). Characterization of Macro stresses. In M. E. Fitzpatrick, & A. Lodini, *Analysis of Residual Stress by Diffraction using Neutron and Synchrotron Radiation* (pp. 60-77). London: Taylor & Francis.
- [43] *Engineering Materials Diffractometer (VULCAN)*. (2011). Retrieved April 5, 2011, from Oak Ridge National Laboratory - Neutron Sciences: <http://neutrons.ornl.gov/instruments/SNS/VULCAN/>
- [44] Holden, T. M. (2000). *SNS Report IS-1.7.9-6055-RE-A-00*. Retrieved February 6, 2011, from <http://neutrons.ornl.gov/instruments/SNS/VULCAN/>
- [45] Pratihari, S., Turski, M., Edwards, L., & Bouchard, P. J. (2009). Neutron Diffraction Residual Stress Measurement in a 316L Stainless Steel Bead-on-Plate Specimen. *International Journal of Pressure Vessels and Piping*, pp. 13-19.
- [46] Brokmeier, H. G., & Yi, S. B. (2008). Texture and Texture Analysis in Engineering Materials. In W. Reimers, A. R. Pyzalla, A. Schreyer, & H. Clemens, *Neutrons and Synchrotron Radiation in Engineering Materials Science* (pp. 57-77). Weinheim: Wiley-VCH Verlag GmbH & Co.

- [47] Wenk, H. R., & Van Houtte, P. (2004). Texture and Anisotropy. In *Rep. Prog. Phys.* 67 (pp. 1367-1428).
- [48] *Stereographic Projection Construction*. (2011). Retrieved April 27, 2011, from aluMATTER: <http://aluminium.matter.org.uk/content/html/eng/0210-0010-swf.htm>
- [49] Verlinden, B., Driver, J., Samajdar, I., & Doherty, R. D. (2007). *Thermo-Mechanical Processing of Metallic Materials*. Oxford: Elsevier Ltd.
- [50] Engler, O., & Randle, V. (2010). *Introduction to Texture Analysis: Macro- and Microtexture & Orientation Mapping 2nd Ed.* Taylor & Francis.
- [51] Matthies, S., Wenk, H. R., Lutterotti, L., & Vogel, S. C. (2005). Quantitative Texture Analysis with the HIPPO Neutron TOF Diffractometer. In *Journal of Applied Crystallography* (pp. 462-475).
- [52] Roos, E., & Maile, K. (2005). *Werkstoffkunde für Ingenieure*. Berlin: Springer-Verlag GmbH.
- [53] Hornbogen, E., Eggeler, G., & Werner, E. (2008). *Werkstoffe: Aufbau und Eigenschaften von Keramik-, Metall-, Polymer- und Verbundwerkstoffen. 9th Edition*. Berlin: Springer-Verlag GmbH.
- [54] Jia, N., Lin Peng, R., Brown, D. W., Clausen, B., & Wang, Y. D. (2008). Tensile Deformation Behavior of Duplex Stainless Steel Studied by In-Situ Time-of-Flight Neutron Diffraction. In *Metallurgical and Materials Transactions A, Vol. 39A no. 13* (pp. 3134-3140).
- [55] Weisser, M. A., Evans, A. D., Van Petegem, S., Holdsworth, S. R., & Van Swygenhoven, H. (2011). In situ Room Temperature Tensile Deformation of a 1% CrMoV Bainitic Steel using Synchrotron and Neutron Diffraction. In *Acta Materialia, Vol. 59, Issue 11* (pp. 4448-4457).
- [56] Li, D. F., O'Dowd, N. P., Davies, C. M., & Zhang, S. Y. (2011). Microscale Prediction of Deformation in an Austenitic Stainless Steel under Uniaxial Loading. In *European Journal of Mechanics A/Solids* (pp. 1-13).
- [57] Muránsky, O., Sittner, P., Zrník, J., & Oliver, E. C. (2009). In-Situ Neutron Diffraction Investigation of the collaborative Deformation-Transformation Mechanism in TRIP-assisted Steels at Room and Elevated Temperatures. In *Nuclear Instruments and Methods in Physics Research A 600* (pp. 313-315).

- [58] Daymond, M. R., & Bouchard, P. J. (2006). Elastoplastic Deformation of 316 Stainless Steel Under Tensile Loading at Elevated Temperatures. In *Metallurgical and Materials Transaction A Vol. 37A* (pp. 1863-1873).
- [59] Van Den Beukel, A. (1975). Theory of the Effect of Dynamic Strain Aging on Mechanical Properties. In *Physica Status Solidi A 30* (pp. 197-206).
- [60] Sharma, R. C. (2002). *Phase Transformations in Materials*. New Delhi: CBS Publishers.
- [61] Tomota, Y., Xu, P. G., Kamiyama, T., & Oliver, E. C. (2009). In-situ TOF Neutron Diffraction during Phase Transformation in an Engineering Steel. In *Nuclear Instruments and Methods in Physics Research A 600* (pp. 313-315).
- [62] *Spallation Neutron Source*. (2011). Retrieved June 7, 2011, from Oak Ridge National Laboratory - Neutron Sciences: <http://neutrons.ornl.gov/>
- [63] Mason, T. E., Abernathy, D., Anderson, I., Ankner, J., Egami, T., Ehlers, G., et al. (2006). The Spallation Neutron Source in Oak Ridge: A powerful Tool for Materials Research. In *Physica B 385-386* (pp. 955-960).
- [64] *Engineering Materials Diffractometer (VULCAN)*. (2011). Retrieved June 8, 2011, from Oak Ridge National Laboratory - Neutron Sciences: <http://neutrons.ornl.gov/instruments/SNS/VULCAN/>
- [65] Wang, X. L., Holden, T. M., Rennich, G. Q., Stoica, A. D., Liaw, P. K., Choo, H., et al. (2006). VULCAN - The Engineering Diffractometer at the SNS. In *Physica B 385-386* (pp. 673-675).
- [66] Wang, X. L., & Stoica, A. D. (2009). Focusing Neutron Guides for VULCAN - Design Aspects, Estimated Performance and Detector Deployment. In *Nuclear Instruments and Methods in Physics Research A* (pp. 309-312).
- [67] An, K., Skorpenske, H. D., Stoica, A. D., Ma, D., Wang, X. L., & Cakmak, E. (2011). First in-situ Lattice Strains Measurements under Load at VULCAN. In *Metallurgical and Materials Transactions A, Vol. 42, No. 1* (pp. 95-99).

Appendix

Appendix A:

Pulsed Spallation Neutron Sources and Main Parameters

Neutron Source	KENS	IPNS	LANSCE	ISIS	SNS	JSNS	CSNS	ESS
Organization	High-E Acc. Research Org.	Argonne National Lab.	Los Alamos National Laboratory	Rutherford Appleton Laboratory	Oak Ridge National Laboratory	Japan Atomic Energy Agency	Institute of High Energy Physics	
Location	Tsukuba, Ibaraki, Japan	Argonne, Illinois, USA	Los Alamos, New Mexico, USA	Didcot, Oxfordshire, UK	Oak Ridge, Tennessee, USA	Tokai, Ibaraki, Japan	Dongguan, Guangdong, China	Lund, Sweden
Proton beam power on target [kW]	4,5	7	56	160	1400	1000	100	5000
Proton beam kinetic energy on target [MeV]	500	450	800	800	1000	3000	1600	1333
Average beam current on target [μ A]	9	15	70	200	1400	333		7500
Pulse repetition rate [Hz]	20	30	20	50/10 (2 targets)	60	25	25	16 (long pulse)
Target material	tungsten	depleted uranium	tungsten	tantalum	mercury	mercury	tungsten	mercury
Moderator	S-CH ₄ /H ₂ O	S-CH ₄ /L-CH ₄	L-H ₂ /H ₂ O	L-H ₂ /L-CH ₄ /H ₂ O	L-H ₂ /H ₂ O	L-H ₂	L-H ₂ /L-CH ₄ /H ₂ O	L-H ₂
Number of instruments	15	12	7	29 (22 TS1 / 7 TS2)	24	23		20
Operation	1980-2005	1981-2008	1983	1985 (TS1) 2008 (TS2)	2006	2008	2014	2019

Abbreviations:

KENS:	KEK ^a Neutron Source
IPNS:	Intense Pulsed Neutron Source
LANSCE:	Los Alamos Neutron Science Center
ISIS:	no acronym
SNS ^b :	Spallation Neutron Source
JSNS	Japanese Spallation Neutron Source
CSNS:	China Spallation Neutron Source
ESS:	European Spallation Source

Data based on reference [1].

^a “Koh Ene Ken” (Japanese: National Laboratory for High-Energy Physics)

^b Proposed Upgrades for 2012:

Proton beam power on target:	2000 - 4000 kW
Proton beam kinetic energy on target:	1300 MeV
Average beam current on target:	2300 μ A

Appendix B:

Neutron Scattering Lengths and Cross Sections of Selected Elements and Isotopes

All these numerical values in the following were taken from the publication authored by Sears [2]. Selected elements and their isotopes are alloying elements which are commonly (or may be) contained in martensitic 9-12% Cr steels (plus iron as the base material). In addition, the list provides data of oxygen and hydrogen. The used abbreviations are presented below [3].

Column	Symbol	Quantity	Unit
1	E	element	
2	Z	atomic number (= number of protons)	
3	A	mass number (= number of protons and neutrons)	
4	b_{coh}	bound coherent scattering length	fm ^c
5	b_{inc}	bound incoherent scattering length	fm
6	σ_{coh}	bound coherent scattering cross section	barn ^d
7	σ_{inc}	bound incoherent scattering cross section	barn
8	σ_{s}	total bound scattering cross section ^e	barn
9	σ_{abs}	absorption cross section for 2200 m/s neutrons	barn

The selected elements are sorted by atomic number and mass number.

E	Z	A	b_{coh}	b_{inc}	σ_{coh}	σ_{inc}	σ_{s}	σ_{abs}
H	1		-3.739		1.7568	80.26	82.02	0.3326
		1	-3.7406	25.274	1.7583	80.27	82.03	0.3326
		2	6.671	4.04	5.592	2.05	7.64	0.000519
		3	4.792	-1.04	2.89	0.14	3.03	0

^c 1 fm = 10⁻¹⁵ m

^d 1 barn = 10⁻²⁸ m² = 100 fm²

^e $\sigma_{\text{s}} = \sigma_{\text{coh}} + \sigma_{\text{inc}}$ in the case of unpolarized neutrons/nuclei

E	Z	A	b_{coh}	b_{inc}	σ_{coh}	σ_{inc}	σ_s	σ_{abs}
B	5		5.30-		3.54	1.70	5.24	767
			0.213 ^f					
		10	-0.1-	-4.7+	0.144	3.0	3.1	3835
			1.066 <i>i</i>	1.231 <i>i</i>				
		11	6.65	-1.3	5.56	0.21	5.77	0.0055
C	6		6.6460		5.550	0.001	5.551	0.00350
		12	6.6511	0 ^g	5.559	0	5.559	0.00353
		13	6.19	-0.52	4.81	0.034	4.84	0.00137
N	7		9.36		11.01	0.50	11.51	1.90
		14	9.37	2.0	11.03	0.5	11.53	1.91
		15	6.44	-0.02	5.21	0.00005	5.21	0.000024
O	8		5.803		4.232	0	4.232	0.00019
		16	5.803	0	4.232	0	4.232	0.00010
		17	5.78	0.18	4.20	0.004	4.204	0.236
		18	5.84	0	4.29	0	4.29	0.00016
Al	13	27	3.449	0.256	1.495	0.0082	1.503	0.231
Si	14		4.1491		2.1633	0.004	2.167	0.171
		28	4.107	0	2.120	0	2.120	0.177
		29	4.70	0.09	2.78	0.001	2.78	0.101
		30	4.58	0	2.64	0	2.64	0.107

^f The scattering length is complex and energy-dependent. Scattering is a resonance phenomenon: formation of compound nuclei (initial nuclei + neutrons). The real part of b is the scattering length of the neutrons, whereas the imaginary part indicates the absorption of neutrons by the nuclei [3].

^g Incoherent parts are zero if the nuclear spin of the nucleus is zero too [3]. The spin of the nuclear ground state for each nuclide can be looked up in [2].

E	Z	A	b_{coh}	b_{inc}	σ_{coh}	σ_{inc}	σ_{s}	σ_{abs}
P	15	31	5.13	0.2	3.307	0.005	3.312	0.172
S	16		2.847		1.0186	0.007	1.026	0.53
		32	2.804	0	0.9880	0	0.9880	0.54
		33	4.74	1.5	2.8	0.3	3.1	0.54
		34	3.48	0	1.52	0	1.52	0.227
		36	3	0	1.1	0	1.1	0.15
Ti	22		-3.438		1.485	2.87	4.35	6.09
		46	4.93	0	3.05	0	3.05	0.59
		47	3.63	-3.5	1.66	1.5	3.2	1.7
		48	-6.08	0	4.65	0	4.65	7.87
		49	1.04	5.1	0.14	3.3	3.4	2.2
		50	6.18	0	4.80	0	4.80	0.179
V	23		-0.3842		0.01838	5.08	5.10	5.08
		50	7.6		7.3	0.5	7.8	60
		51	-0.402	6.35	0.0203	5.07	5.09	4.9
Cr	24		3.635		1.660	1.83	3.49	3.05
		50	-4.50	0	2.54	0	2.54	15.8
		52	4.920	0	3.042	0	3.042	0.76
		53	-4.20	6.87	2.22	5.93	8.15	18.1
		54	4.55	0	2.60	0	2.60	0.36
Mn	25	55	-3.73	1.79	1.75	0.40	2.15	13.3
Fe	26		9.45		11.22	0.40	11.62	2.56
		54	4.2	0	2.2	0	2.2	2.25

E	Z	A	b_{coh}	b_{inc}	σ_{coh}	σ_{inc}	σ_s	σ_{abs}
		56	9.94	0	12.42	0	12.42	2.59
		57	2.3		0.66	0.3	1	2.48
		58	15	0	28	0	28	1.28
Co	27	59	2.49	-6.2	0.779	4.8	5.6	37.18
Ni	28		10.3		13.3	5.2	18.5	4.49
		58	14.4	0	26.1	0	26.1	4.6
		60	2.8	0	0.99	0	0.99	2.9
		61	7.60	± 3.9	7.26	1.9	9.2	2.5
		62	-8.7	0	9.5	0	9.5	14.5
		64	-0.37	0	0.017	0	0.017	1.52
Cu	29		7.718		7.485	0.55	8.03	3.78
		63	6.43	0.22	5.2	0.006	5.2	4.50
		65	10.61	1.79	14.1	0.40	14.5	2.17
Nb	41	93	7.054	-0.139	6.253	0.0024	6.255	1.15
Mo	42		6.715		5.67	0.04	5.71	2.48
		92	6.91	0	6.00	0	6.00	0.019
		94	6.80	0	5.81	0	5.81	0.015
		95	6.91		6.00	0.50	6.5	13.1
		96	6.20	0	4.83	0	4.83	0.5
		97	7.24		6.59	0.5	7.09	2.5
		98	6.58	0	5.44	0	5.44	0.127
		100	6.73	0	5.69	0	5.69	0.4
W	74		4.86		2.97	1.63	4.60	18.3

E	Z	A	b_{coh}	b_{inc}	σ_{coh}	σ_{inc}	σ_s	σ_{abs}
		180	5	0	3	0	3	30
		182	6.97	0	6.10	0	6.10	20.7
		183	6.53		5.36	0.3	5.66	10.1
		184	7.48	0	7.03	0	7.03	1.7
		186	-0.72	0	0.065	0	0.065	37.9

Appendix C:

Radii of Gyration of some Selected Homogeneous Particles

Data based on reference [4].

Type	Radius of gyration
Sphere of radius R	$R_g^2 = \frac{3R^2}{5}$
Spherical shell with radii $R_1 > R_2$	$R_g^2 = \frac{3R_1^5 - R_2^5}{5R_1^3 - R_2^3}$
Ellipse with axis a, b	$R_g^2 = \frac{a^2 + b^2}{5}$
Ellipsoid with axis a, b, c	$R_g^2 = \frac{a^2 + b^2 + c^2}{5}$
Prism with side lengths A, B, C	$R_g^2 = \frac{A^2 + B^2 + C^2}{12}$
Cylinder with radius R and length L	$R_g^2 = \frac{L^2}{6}$

Appendix D:

Technical Parameters of the SNS

Data based on reference [5].

Proton beam power on target	1.4 MW
Proton beam kinetic energy on target	1.0 GeV
Average beam current on target	1.4 mA
Pulse repetition rate	60 Hz
Protons per pulse on target	1.5×10^{14} protons
Charge per pulse on target	24 μ C
Energy per pulse on target	24 kJ
Proton pulse length on target	695 ns
Ion type (Front-end, Linac ^h , HEBT ⁱ)	H ⁻
Average linac macropulse duty factor	26 mA
Linac beam macropulse duty factor	6%
Front-end length	7.5 m
Linac length	331 m
HEBT length	170 m
Ring circumference	248 m
RTBT ^j length	150 m
Ion Type (Ring, RTBT, Target)	Proton
Ring filling time	1.0 ms
Ring revolution frequency	1.058 Hz
Number of injected turns	1060
Ring filling fraction	250 ns
Maximum uncontrolled beam loss	1 W/m
Target material	Hg
Number of ambient/cold moderators	1/3
Number of neutron beam shutters	18

^h Linear accelerator

ⁱ High-energy beam transport

^j Ring-to-target beam transport

Appendix E:

SNS Instrumentation

14 instruments are currently available, 5 are to be commissioned in the next few years and 3 are under development or under consideration. There are 24 beam lines on a total number of 18 neutron beam shutters [5].

Available Instruments

Instrument Name	Beam Line	Moderator
Nanoscale-Ordered Materials Diffractometer (NOMAD)	1B	decoupled hydrogen
High-Resolution Backscattering Spectrometer (BASIS)	2	decoupled hydrogen
Spallation Neutrons and Pressure Diffractometer (SNAP)	3	decoupled hydrogen
Magnetism Reflectometer	4A	coupled hydrogen
Liquids Reflectometer	4B	coupled hydrogen
Cold Neutron Chopper Spectrometer (CNCS)	5	coupled hydrogen
Extended Q-Range Small-Angle Neutron Scattering Diffractometer (EQ-SANS)	6	coupled hydrogen
Engineering Materials Diffractometer (VULCAN)	7	water
Powder Diffractometer (POWGEN)	11A	decoupled hydrogen
Single-Crystal Diffractometer (TOPAZ)	12	decoupled hydrogen
Fundamental Neutron Physics Beam Line (FNPB)	13	coupled hydrogen
Neutron Spin Echo Spectrometer (NSE)	15	coupled hydrogen
Fine-Resolution Fermi Chopper Spectrometer (SEQUOIA)	17	water
Wide Angular-Range Chopper Spectrometer (ARCS)	18	water

Future Instruments

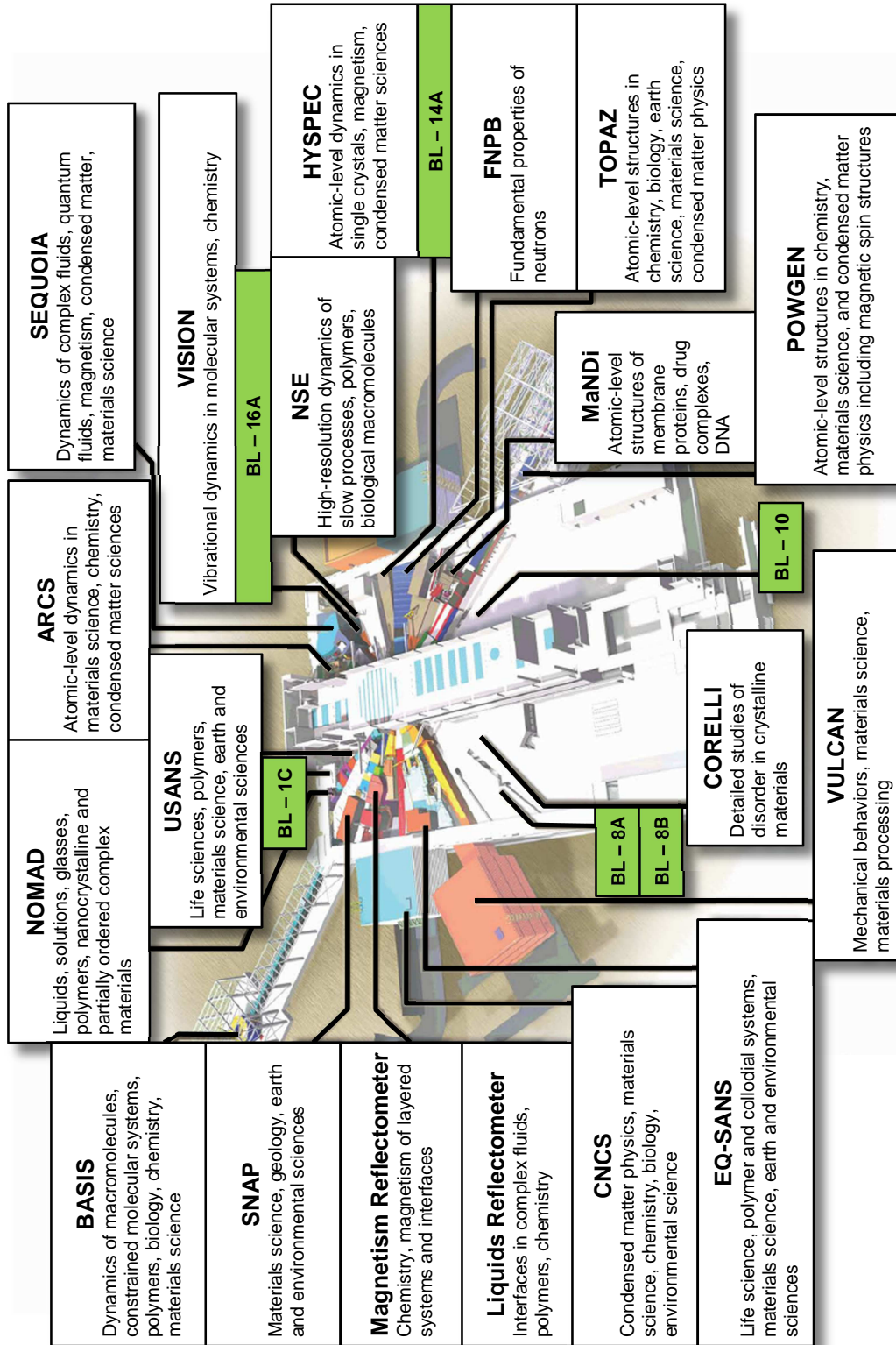
Instrument	Beam Line	Moderator	Planned Date
Ultra-Small-Angle Neutron Scattering Instrument (USANS)	1A	decoupled hydrogen	2014
Elastic Diffuse Scattering Spectrometer (CORELLI)	9	water	2014
Macromolecular Diffractometer (MaNDi)	11B	decoupled hydrogen	2012
Hybrid Spectrometer (HYSPEC)	14B	coupled hydrogen	in commissioning
Chemical Spectrometer (VISION)	16B	water	2012

Proposed Instruments

- Spin-Echo Resolved Grazing Incidence Scattering (SERGIS)
- Neutron Radiography (VENUS)
- Neutron Scattering at high Magnetic Fields (ZEEMANS)

The corresponding locations and the application fields are represented on the next page.

SNS Instrument Layout



List of Literature

- [1] Arai, M., & Crawford, K. (2009). Neutron Sources and Facilities. In I. S. Anderson, R. L. McGreevy, & H. Z. Bilheux, *Neutron Imaging and Applications: A Reference for the Imaging Community (Neutron Scattering Applications and Techniques)* (pp. 13-30). New York: Springer.
- [2] Sears, V. F. (1992). Neutron Scattering Lengths and Cross Sections. In *Neutron News Vol. 3, No.3* (pp. 26-37).
- [3] Squires, G. L. (1978). *Introduction to the Theory of Thermal Neutron Scattering*. Cambridge, UK: Cambridge University Press.
- [4] Lelong, G., Price, D. L., & Saboungi, M. L. (2011). Scattering Techniques. In N. Kanellopoulos, *Nanoporous Materials - Advanced Techniques for Characterization, Modeling and Processing* (pp. 3-52). Boca Raton FL - USA: Taylor & Francis.
- [5] *Spallation Neutron Source*. (2011). Retrieved June 7, 2011, from Oak Ridge National Laboratory - Neutron Sciences: <http://neutrons.ornl.gov/>